UNIVERSITÀ
degli STUDI
di CATANIA

MSc programme in physics

Cristiano Lo Pò

Laser production of Cu- and Ni-based nanostructures for water splitting applications

final project

Supervisor:
Prof. F. Ruffino

Co-Supervisor:
Dr. V. Iacono

academic year 2022/2023

Contents

List of Abbreviations

CE Counter Electrode. 15, 92

CNT Carbon Nanotube. 26, 29, 30

CPE Constant Phase Element. 97

CV Cyclic Voltammetry. 2, 9, 32, 88, 93, 94, 100, 102, 104, 108, 110, 156, 157

EDX Energy Dispersive X-Ray. 2, 3, 8, 32, 65–67, 69, 81, 123, 136, 139, 140, 142, 143

EIS Electrochemical Impedance Spectroscopy. 2, 9, 32, 88, 96, 98, 100, 102–106, 109–113, 115, 156, 159, 160

FFT Fast Fourier Transform. 54–57

GP Graphene Paper. 2, 9, 88–95, 98, 100–106, 113–120, 124, 153, 156–162

HER Hydrogen Evolution Reaction. 1, 2, 9, 19, 20, 22, 26–31, 42, 93–95, 98, 102–106, 108–110, 113, 114, 117–120, 123, 124, 156–162

HHV Higher heating values. 13, 14

LHV Lower heating values. 13, 14

LSV Linear Sweep Voltammetry. 2, 9, 32, 88, 94, 95, 100, 102–106, 108, 109, 111, 112, 115, 156–159

MS Mott Schottky. 2, 9, 32, 88, 99–101, 107, 108, 156

NF Nichel Foam. 2, 9, 26, 29, 30, 88, 89, 91–94, 99, 106–120, 124, 161, 162

NP Nanoparticle. 2, 8, 9, 26, 28–32, 37–53, 55, 57–71, 73, 76, 77, 79–82, 88–92, 94, 98, 100, 102, 104, 106, 109, 111, 113–115, 117–120, 123–126, 160, 161

OC Open Circuit. 2, 100, 101, 107, 108, 156, 157

OER Oxygen Evolution Reaction. 1, 2, 9, 20–22, 26–31, 42, 93–95, 98, 104–106, 110–113, 115–120, 123, 124, 156–162

PLAL Pulsed Laser Ablation in Liquid. 1, 2, 8, 30, 31, 37, 38, 40–42, 46, 67–69, 98, 100, 106, 123, 124, 154–158, 161

RBS Rutherford Backscattering Spectrometry. 2, 8, 32, 88–90, 124, 127, 144–146, 154, 155

RE Reference Electrode. 15, 92, 93, 97

RHE Reversible Hydrogen Electrode. 15, 95, 101–103, 105, 109, 112, 119, 161

SCE Saturated Calomel Electrode. 15, 92, 94, 95, 101, 102, 104, 106, 108, 110, 113, 160

SEM Scanning Electron Microscopy. 2, 3, 8, 32, 46–48, 50, 53, 68, 78, 81, 82, 88, 91, 117, 123, 124, 127, 136–139, 141

SHE Standard Hydrogen Electrode. 15, 95

STEM Scanning Transmission Electron Microscopy. 65, 66, 141, 143

TEM Transmission Electron Microscopy. 2, 8, 32, 50, 53, 55, 58, 65, 68, 76, 78, 79, 81, 82, 123, 127, 141–143

UV-Vis-NIR UltraViolet - Visible - Near InfraRed. 2, 8, 31, 44, 67, 123, 133

WE Working Electrode. 14, 15, 88, 92–94, 97

XPS X-Ray Photoelectron Spectroscopy. 2, 8, 32, 61–65, 67, 69, 70, 80–82, 123, 127, 150, 151

XRD X-Ray Diffraction. 2, 8, 32, 59–61, 68, 81, 82, 123, 127, 147, 148

Introduction

In the field of sustainability, the Hydrogen is considered a clean fuel and a renewable energetic source with no pollutant emissions. The most simple way to produce Hydrogen is from water using electrolysis. One of the goals on the scientific research nowadays is to find some catalyst for the water splitting reaction that are cheap, easy to find and also easy to be synthesized.

Transition metals and their oxides presents a good alternative to critical materials such as Platinum and Iridium. In particular, the most recent challenge is to use nanostructured materials to maximize catalytic activity. In this scope, this work deals with the production of Copper and Nickel Nanoparticles as catalyst in the water splitting reaction.

First the Nanoparticles will be synthesized using the Pulsed Laser Ablation in Liquid in organic solvent. This technique is chosen because is sustainable, cheap, rapid and at high yield of particle production. The so produced Nanoparticles will be stored in the same solvent in which they are produced for a long time before the usage. Also the Copper and Nickel are chosen because of their abundance and low cost.

Then these Nanoparticles must be analyzed to understand their morphology, structure and composition. The following techniques will be used: UV-Vis-NIR Spectrophotometry, SEM, TEM, XRD, XPS and EDX.

Then the electrodes were prepared by drop casting some μl of Nanoparticles solution on the substrate and will be characterized with SEM and RBS to find out the amount of deposited material. The chosen substrates

are Graphene Paper and Nichel Foam because they are cheap, easy to find and made of abundant and non pollutant materials. The produced electrodes will be tested both in the production of Hydrogen and Oxygen (depending on the applied potential) using the following electrochemical analysis: CV, LSV, EIS and MS.

The electrodes produced in this work will presents only few μg of catalyst and obtain so a lower overpotential ($\sim 80mV$ in HER and $\sim 60mV$ in OER) with respect to the bare substrate indicating a strong electrocatalytic activity of the Nanoparticles. The low amount of catalyst material makes these electrodes comparable with the one reported in literature at the state of the art.

A deep study of the Nanoparticles alone will show a new phenomenon non reported in literature: the presence of a polymer all around the particles that preserve their metallic nature. Also a simplistic model will be developed to find out the nature of the differences in the overpotential improvement between the various electrodes relating this parameter with the electronic properties of the substrate and the Nanoparticles.

Chapter 1

When life gives you water, make Hydrogen

1.1 The energetic problem

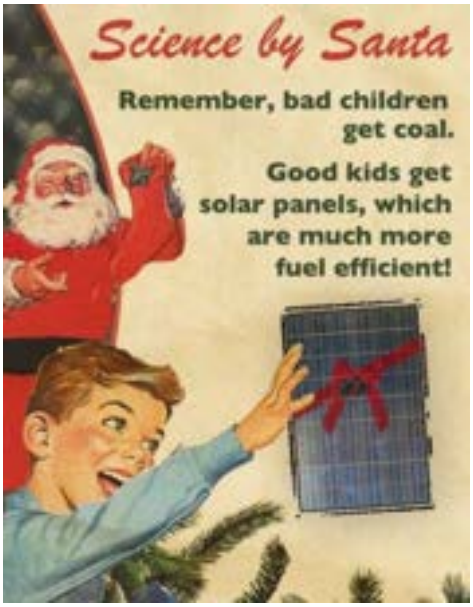

Figure 1.1: Randomly found on the internet.

In the last two hundred years the energy consumption in the world has grown rapidly, resulting in an increase in the exploitation of energy sources. First industrial revolution was carried by coal combustion. Within a century, thermal engine arrived on the wave of oil derivatives combustion. Population growth leads to ever greater energy demand but oil reserves are going to end and the excessive use of combustion as source of energy brought to environment pollution and climatic changes. To remedy this problem, new energy sources were investigated: bio fuels, solar energy, wind energy, hydroelectric energy, geothermal energy, nuclear energy and so forth [1, 2].

Bio fuels (or more in general biomass) are produced by plants and garbage and are compatible with old thermal engine technology, but they have the same problem as the petroleum derivatives: they produce a significant amount of carbon dioxides and other pollutants when burnt. Solar energy can be a good alternative, but solar panel production is expensive and requires rare elements, so big mines are required to satisfy the rising demand of rare earths used in all field of technology manufacturing. Also big solar farms cover high terrain surface which can be used instead for agriculture and the electricity production strongly depends on the weather. Hydroelectric energy requires dams and artificial lake, that can also be used as a solution for the rising drought. Nuclear energy is good for high amount of electric energy production.

These clean and renewable energy sources can be a solution for cities and industries, but transports are more problematic because traditional fuels are logistical convenient for avoid long stop time to recharge batteries. Also the production of high power electric accumulators for vehicles requires a large amount of rare earths and their disposal produce a lot of non recyclable wastes.

In general an energy source for the future should be easily transportable and able to produce energy in loco. Actual electric lines in fact disperse energy in form of Joule effect.

As reported in Figure 1.2 and 1.3, most of the energy produced today come from coal, oil and natural gas. But nowadays price of these raw materials is rising also due to their scarcity, so an urgent alternative is required.

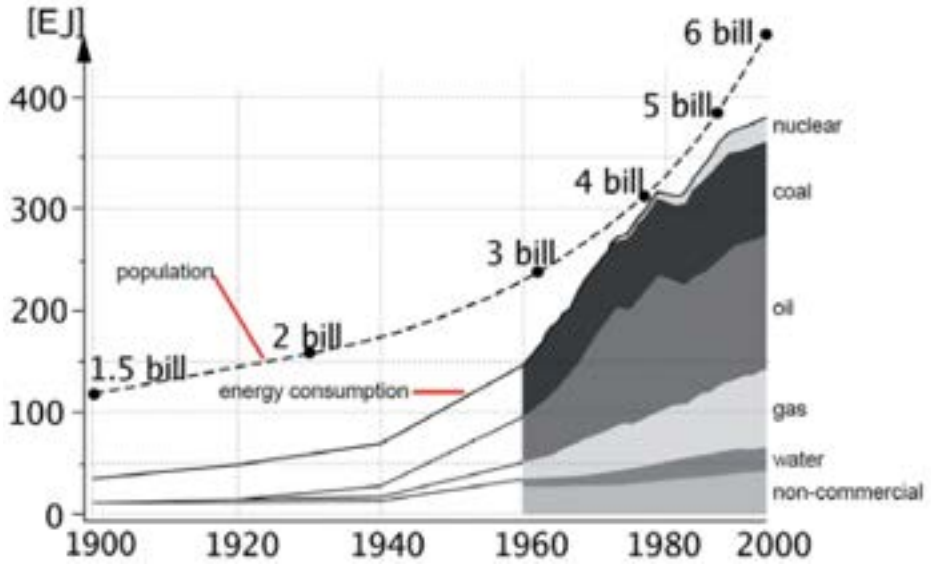

Figure 1.2: Growth of the world population and energy consumption in the 20th century. The dashed curve shows the population; the curves below show the energy consumption, broken down into the main energy carriers [3] ($1EJ = 10^{18}J$).

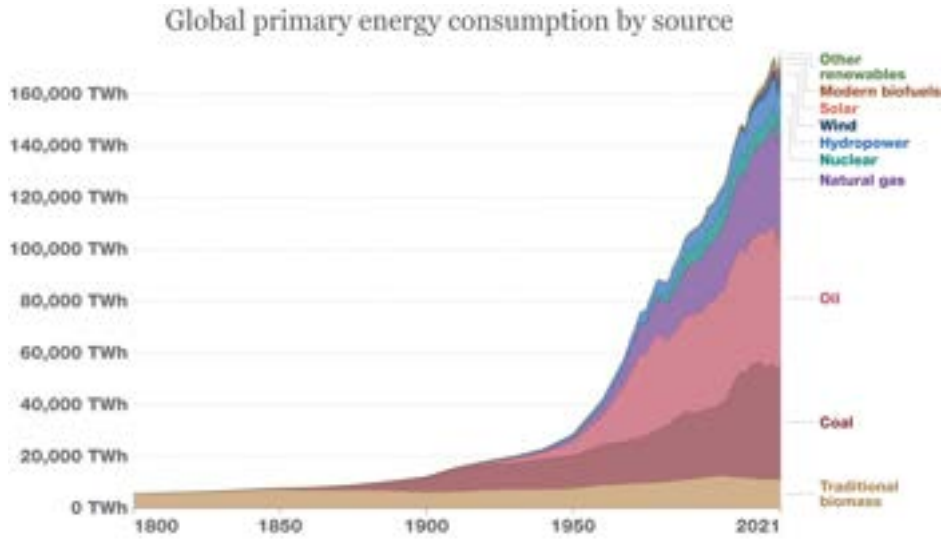

Figure 1.3: World electricity production by various energy source [4] ($1Wh = 3.6kJ$).

1.1.1 Hydrogen as solution

Hydrogen can be a solution to energetic problem because it can be burned like traditional fuel and can be used in fuel cells to produce electric energy.

In general hydrogen reacts with oxygen and the overall reaction is:

$$2H_2 + O_2 \rightarrow 2H_2O \tag{1.1}$$

Hydrogen is a clean energy source because it only requires oxygen from air and produce only water (or aqueous vapour) as waste, so is carbon free unlike traditional fuels [5]. The chemical burning of hydrogen also doesn't produce Nitrogen-based compounds like NO_x that is a dangerous pollutant.

Some of the advantages of hydrogen are [5]:

- high energy conversion efficiencies (defined as useful output energy divided by total input energy) and ease of conversion to other forms of energy: thermal energy is easily produced by combustion and electrical energy in fuel cells;

- different ways of production: hydrogen can be obtained by thermal, electrical and biochemical methods. The most common method is the electrolysis of water, in which direct current is applied to split water. Light can help the process with photoactive electrodes. In water also a very high temperature ($2500K$) can separate Hydrogen and Oxygen. Hydrogen can be obtained by fossil fuels for examples by using plasma arc decomposition. Others method are in the fields of chemistry and biochemistry;

- Higher heating values (HHV) and Lower heating values (LHV) bigger than most of the conventional fossil fuels[1] (Table 1.1);

[1] In the field of fuel combustion HHV is the amount of heat produced by the complete combustion of a unit quantity of fuel and is obtained when all products of the combustion are cooled down to the temperature before the combustion and the water vapor formed during combustion is condensed. LHV is obtained subtracting the latent heat of vaporization of the water vapor formed by the combustion from HHV[6].

- abundance: can be found in many substances in nature like water, biomass and fossil fuels;
- different forms of storage and long distance transportation: it can be stored in tanks in form of gas (at standard temperature and pressure $273.15K$ and $10^5 bar$) or can be compressed until it becomes liquid.

Fuel	HHV (kJ/g)	LHV (kJ/g)
Hydrogen	141.9	119.9
Methane	55.5	50.0
Gasoline	47.5	44.5
Diesel	44.8	42.5
Methanol	20.0	18.1

Table 1.1: HHV and LHV of some fuels [5].

So, hydrogen is much more efficient than traditional fuels with thermal technology, is easy to produce and transport and can be used also in other ways. For all this reasons and some other economic reasons hydrogen is considered important for the future and, hence, the scientific research in the next years will focus on it. A lot of interest is directed toward the hydrogen production from water using electrolysis because is the most simple and interesting way.

1.2 Electrochemical cell

The most common method to produce hydrogen is the electrolysis of water. The apparatus for perform and study electrolysis is the electrochemical cell [7]. These cells are made up by a can with electrolyte in which two or three electrode lies. The possible reactions and effects are studied applying a potential difference between two electrodes and measuring the current flowing. These electrodes should be standard and well known with stable characteristics and do not react with the studied species in solution. Initially this apparatus were used to study the charge transport in liquid and the possible chemical reactions that happens on an electrode surface that is called Working Electrode (WE). The other electrode

is called Counter Electrode (CE) and is generally chosen to be inert under the reaction condition [7].

Each standard electrode has a well known potential evaluated as compared to the Standard Hydrogen Electrode (SHE) whose potential is chosen by convention to be $E_{SHE} = 0.000V$ [8]. The CE must be non reactive with the electrolyte and also stable. The best CE is a Platinum wire or disk whose potential is pH dependent:

$$E_{RHE} = (E_{SHE} - 0.059 \cdot pH)V \tag{1.2}$$

This is called Reversible Hydrogen Electrode (RHE) and it's a special case of the SHE.

The difference between two and three electrodes configuration is the presence of a Reference Electrode (RE) that is in potential equilibrium with liquid. Voltage is measured between WE and RE, current between WE and CE. A common RE is the Saturated Calomel Electrode (SCE) whose potential is $E_{SCE} = 0.241V + E_{SHE}$ (at $25°C$) respect to the SHE.

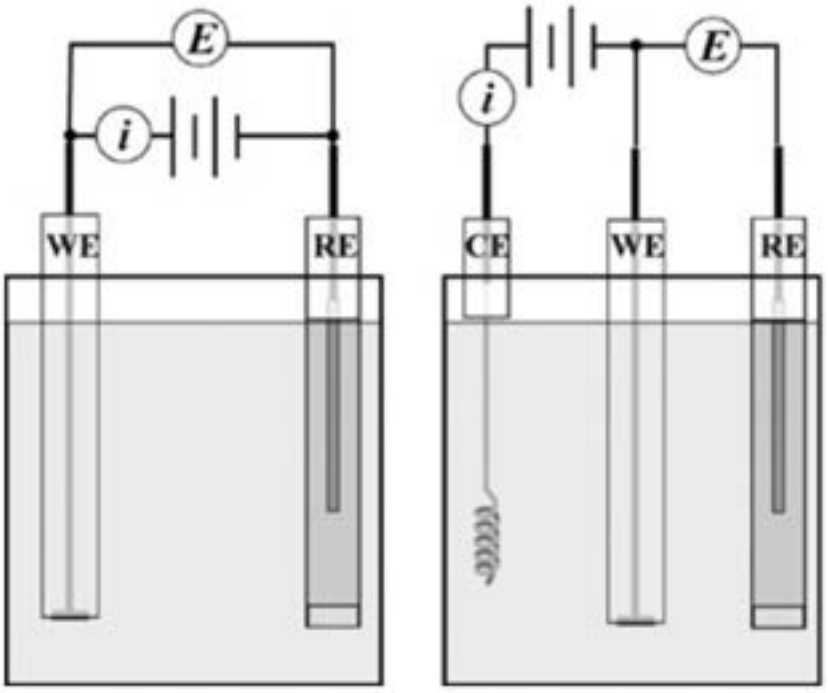

Figure 1.4: Scheme of two and three electrode electrochemical cell [7].

1.2.1 Water splitting

The reaction performed to obtain hydrogen from water in an electrochemical cells is called water splitting:

$$2H_2O \rightarrow 2H_2 + O_2 \tag{1.3}$$

This reaction follows different steps in case of alkaline or acidic condition [9]. In acidic condition there is an higher concentration of H^+ that act like charge carriers and the reactions are the following:

$$\text{Cathode: } 4H^+ + 4e^- \rightarrow 2H_2$$

$$\text{Anode: } 2H_2O \rightarrow O_2 + 4H^+4e^- \tag{1.4}$$

The required energy for cathode reaction is $E_c^0 = -0.83eV$, for anode reaction is $E_a^0 = -0.40eV$.

In alkaline (basic) condition there is an higher concentration of OH^- and the reactions are the following:

$$\text{Cathode: } 4H_2O + 4e^- \rightarrow 2H_2 + 4OH^-$$

$$\text{Anode: } 4OH^- \rightarrow O_2 + 2H_2O + 4e^- \tag{1.5}$$

The required energy for cathode reaction[2] is $E_c^0 = 0eV$, for anode reaction is $E_a^0 = 1.23eV$. In both case $|E_c^0 + E_a^0| = 1.23eV$ so a minimum applied voltage between electrodes of $1.23V$ is required to start the reaction.

The starting point to obtain the current behaviour in the cell is the Nernst Equation [10]:

$$E = E^0 + \frac{RT}{nF} ln \frac{C_O}{C_R} \tag{1.6}$$

where E is the applied potential, E^0 is the equilibrium voltage of the cell, T is the absolute temperature, R is the universal gas constant, F is the Faraday constant, n is the number of transferred electron and C_O and C_R are the oxidizing and reducing reagents concentration. The currents

[2] In reference [9] E_a^0 and E_c^0 in basic and acidic conditions are inverted.

j (anodic and cathodic) are strictly related to concentrations C (reducing and oxidizing) via the relation:

$$\frac{j}{nFA} = const \cdot C \tag{1.7}$$

where the constant depends on diffusion constants and A indicates the electrode surface. Substituting Equation 1.7 in the logarithmic part of Equation 1.6 the Equation become current dependent. Inverting Equation 1.6 is possible to can obtain anodic contribution (reduction) and cathodic contribution (oxidation) to the current:

$$j_{a/c} = nFk_{a/c}exp\left(\frac{\alpha_{a/c}nF\eta}{RT}\right) \tag{1.8}$$

where the subscript a/c indicates the anode/cathode behaviour, $k_{a/c}$ are the rate constant of half reaction and depends on concentrations ($k_a(C_R)$, $k_c(C_O)$), $\alpha_{a/c}$ are the transfer coefficients and η is called overpotential. The **overpotential** in general is given by:

$$\eta = E - E_{eq} \tag{1.9}$$

where E_{eq} is the equilibrium potential at with the total current is null ($j_{tot} = 0$). E_{eq} is not exactly E^0 but it has some correction due to temperature, basic/acid condition and electron transfer between electrodes and solution, but can be evaluated experimentally. The overall current is $j = j_a + j_c$, but is convenient to express the density current instead of the current[3]:

$$i = j/A \tag{1.10}$$

So follow the Butler-Volmer Equation:

$$i = i_0\left(exp\left(\frac{\alpha_a nF\eta}{RT}\right) + exp\left(\frac{\alpha_c nF\eta}{RT}\right)\right) \tag{1.11}$$

where i_0 is called exchange current and represents the electrodes current at $\eta = 0$. When the potential to an electrode is high, the current given by the other is negligible, so the current can be approximated to:

$$i \approx i_0 exp\left(\frac{\alpha_a nF\eta}{RT}\right) \tag{1.12}$$

[3]In other books and formalism i is the current and j is the current density.

and this is called Tafel Equation. Taking the logarithm this can be rewritten as a linear Equation:

$$log(i) = log(i_0) + \frac{\eta}{b} \tag{1.13}$$

where b is called **Tafel slope**. From graphics representation of $log(i)$ and η is possible to fit the linear behaviour and obtain the Tafel slope and the exchange current. Tafel plot is important because it provides information associated with the rate determining steps: the exchange current $i_0 = nFk$ is given by the reaction rate k, the Faraday constant F and the number electron involved n; the slope $b = RT/\alpha F$ is related to gas constant R, the temperature T and the transfer coefficient α. Usually Tafel plots presents different linear behaviours, this happen because the overall reaction is made up by different steps activated at different potentials [11].

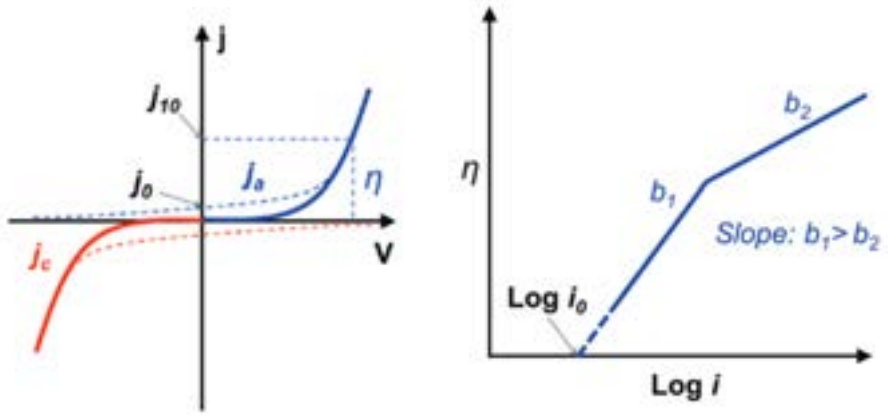

Figure 1.5: Left: example of cathode and anode current behaviour; Right: example of Tafel plot with different Tafel slopes [9].

To compare different experiments performed in different conditions two important parameters are usually reported. One is the overpotential at the given current density of $10 mA/cm^2$ [12], the other is the Tafel slope. Better results involves small overpotential and small Tafel slope.

1.2.2 Hydrogen Evolution Reaction

The Hydrogen Evolution Reaction (HER) is the set of processes which lead from water to gaseous hydrogen [13]. The first step involves the brakes of the water molecule and the adsorption of an hydrogen atom on the electrode (indicated with M) and it's called Volmer step:

$$H_2O + e^- + M \rightarrow M - H_{ads} + OH^- \tag{1.14}$$

Depending on the coverage of hydrogen atoms two different steps can occur. At low coverage a new water molecule breaks and the new hydrogen atom bonds with the adsorbed forming an H_2 molecule that leaves in form of gas. This is the Heyrovsky step:

$$H_2O + e^- + M - H_{ads} \rightarrow H_2 + OH^- + M \tag{1.15}$$

When the coverage is high, two adsorbed atoms bound each other and leave, this is the Tafel step:

$$2M - H_{ads} \rightarrow H_2 + 2M \tag{1.16}$$

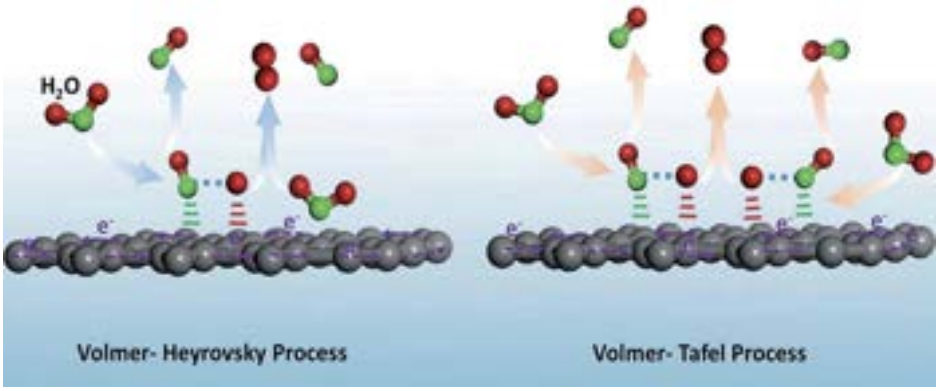

Figure 1.6: Scheme of different process in HER [13].

The reactions can be affected by the binding energy between the electrode and hydrogen atoms. The plot in Figure 1.7 is called volcano plot and presents the binding energy vs the exchange current for metals [14]. An interpretation of this graph is that when the binding energy is too

low, the electrode finds it difficult to absorb the hydrogen atoms in the Volmer step limiting the reaction speed and consequently the current. On the other side, when the binding energy is too high the electrode easily absorbs the hydrogen atoms and prevents them to form H_2 in Heyrovsky and Tafel steps. A good compromise are the metals that have medium binding energy, which result in having an high exchange current and so high performance in HER.

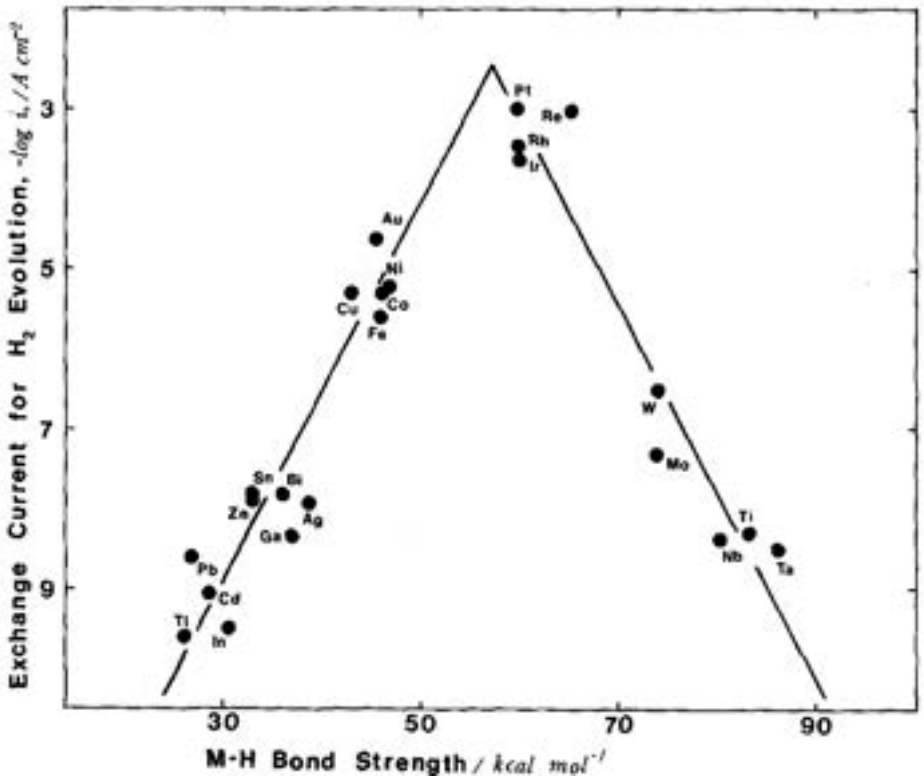

Figure 1.7: Hydrogen binding energy and exchange current for different metals [14].

1.2.3 Oxygen Evolution Reaction

Oxygen Evolution Reaction (OER) is the set of processes which lead from water to gaseous oxygen. Proposed mechanisms (summarized in Figure 1.8) are different for acidic and basic conditions and are composed by dif-

ferent steps involving the bonding between the electrode and the species O, OH and OOH [9].
In acidic condition the reactions are:

$$\begin{aligned} M + H_2O &\rightarrow MOH + H^+ + e^- \\ MOH + OH^- &\rightarrow MO + H_2O + e^- \\ 2MO &\rightarrow 2M + O_2 \\ MO + H_2O &\rightarrow MOOH + H^+ + e^- \\ MOOH + H_2O &\rightarrow M + O_2 + H^+ + e^- \end{aligned} \tag{1.17}$$

In alkaline condition the reactions are:

$$\begin{aligned} M + OH^- &\rightarrow MOH \\ MOH + OH^- &\rightarrow MO + H_2O \\ 2MO &\rightarrow 2M + O_2 \\ MO + OH^- &\rightarrow MOOH + e^- \\ MOOH + OH^- &\rightarrow M + O_2 + H_2O \end{aligned} \tag{1.18}$$

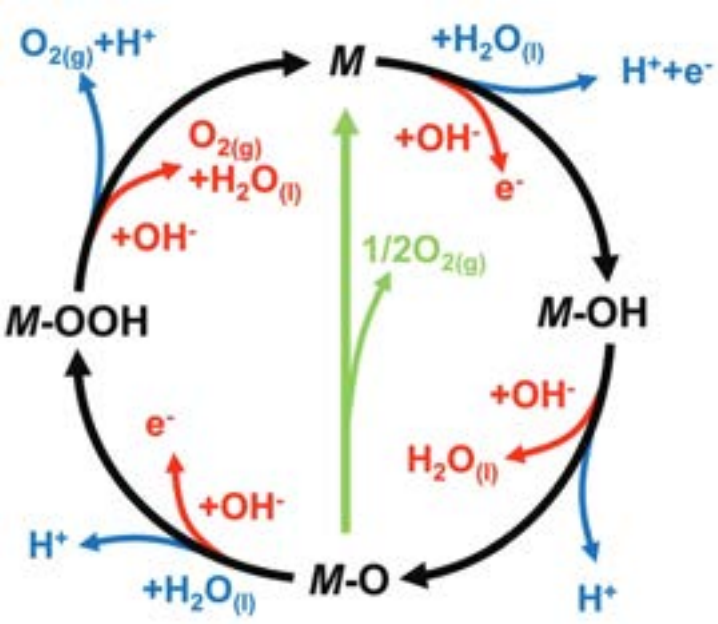

Figure 1.8: Scheme of OER: blue arrows are acidic reactions, red arrows are basic reactions [9].

OER and HER are not mutual exclusive: when the optimal potential difference is given, OER occurs on the anode and HER on cathode simultaneously. In fact at some time is possible to see some bubbles growing on the electrodes surface and migrates to the liquid surface.

1.3 Liquid and electrode interaction

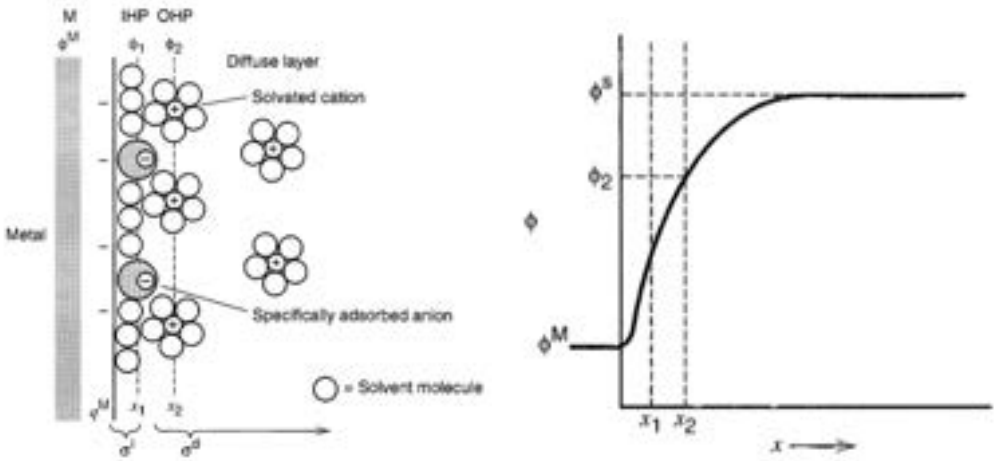

Figure 1.9: Representation of the double layer on the left and potential behaviour on the right. Inner Helmoltz Plane and Outer Helmoltz Plane indicated with x_1 and x_2 [15].

A study of the interface between electrode and solution can help to understand the physical phenomena that occurs on the electrode surface. The electrode-solution interface has been shown experimentally to behave like a capacitor [15, 16, 17], so the charge in solution near the electrode is equal and opposite of the charge in the electrode. The charge on the electrode is due to an excess or deficiency of electrons and resides in a very thin layer (less than an angstrom for metals). The charge in solution is due to an excess of either cations or anions in the proximity of the electrode surface. The whole array of charged species and oriented dipoles existing at the electrode-solution interface is called the electrical double layer. The first layer in solution is called inner layer and contains solvent molecules

and sometimes other species that are adsorbed on the electrode. The site of the electric centers of the adsorbed ions is called Inner Helmoltz Plane. Solvated ions can approach the electrode only to a bigger distance due to their bigger radius, the center of the this ions is called Outer Helmoltz Plane. Because of thermal agitation, these ions are distributed in a three-dimensional region called the diffuse layer. The sum of the charge of these two layer must be equal to the electrode charge. The charge distribution induces a potential behaviour showed in Figure 1.9 trough the electrical double layer.

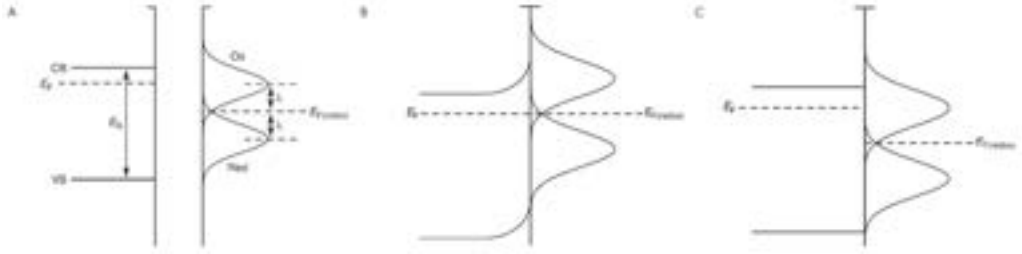

Figure 1.10: (A) Schematic of an n-type semiconductor and the redox states in solution (Ox and Red), with their corresponding Fermi level ($E_{F(redox)}$) and solvent-reorganization energy (λ). (B) Electronic equilibrium between the n-type semiconductor and redox couple in solution. (C) Situation when the semiconductor is at its flat-band potential V_{fb} [18].

In the semiconductor the interaction produces a band bending near the surface. The energy distributions of the solution states depend on whether the state is occupied (Red) or vacant (Ox) [18]. The charge exchange between the electrode and the solution is a dynamic process leading to a range of energies good described in terms of separate Gaussian distributions (Figure 1.10). A Fermi level for the solution $E_{F(redox)}$ can be expressed as the energy at which the probability of a state being occupied by an electron is 0.5 and lies in the middle of the two gaussians.

When a semiconductor is in contact with the liquid, the Fermi levels of both don't match, so a charge transfer occurs until the equilibrium is reached. In Figure 1.10 a n-type semiconductor gives electrons to the Ox species resulting in a positively charging of the semiconductor and a upward band bending. Carrier density in semiconductor is much smaller

than metals and solution itself, so a bigger charge layer (or depletion region) is placed inside the semiconductor surface.

Charge density ρ is related to the band potential ϕ via the Poisson Equation:

$$\frac{d^2\phi}{dx^2} = -\frac{\rho}{\epsilon\epsilon_0} \tag{1.19}$$

where ϵ and ϵ_0 are the dielectric constant of semiconductor and of the vacuum. Solution to this Equation gives both the band bending and the width of the depletion layer W in terms of applied potential V, flat-band potential V_{fb}, electron charge e and donor number N_d [19]:

$$W = \sqrt{\frac{2\epsilon\epsilon_0(V - V_{fb})}{eN_d}} \tag{1.20}$$

Flat band potential V_{fb} is the applied voltage at which there is no band bending or charge depletion region (Figure 1.10 C).

1.4 Nanotechnology

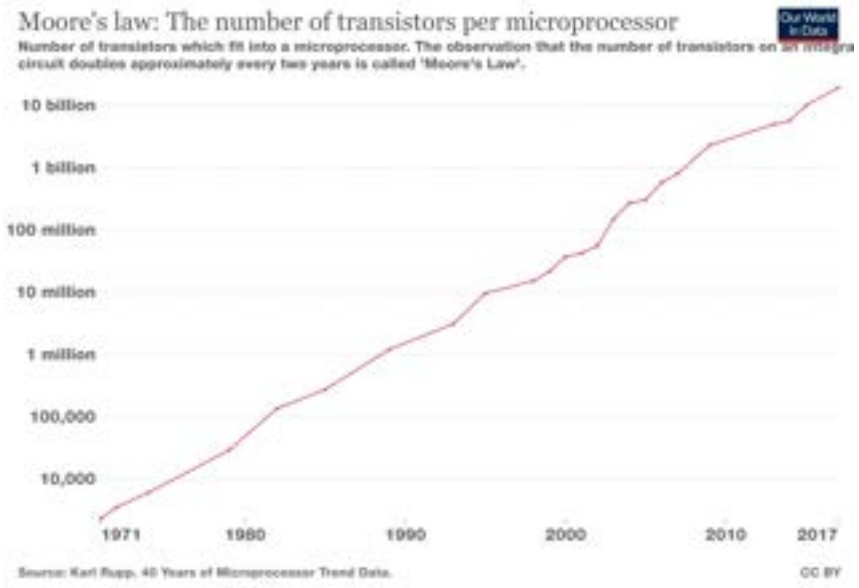

Figure 1.11: Number of transistors per microprocessor by year [20].

Nanotechnologies are present in everyday life as they make up almost all the objects we use. From computers to sensors, from TVs to cars, nanotechnologies are the fundamental components that make everything work. The main element of every electronic system is the MOSFET. It is a transistor made up by two contacts on a doped semiconductor substrate and an isolated gate that works like a capacitance controlling the available charges in the semiconductor and so the conduction of the device. An empirical law [21] states that roughly every two years, the number of transistors on microchips will double (Figure 1.11). This was valid in the past years, but now we are reaching the limit because of the prevailing quantum effects, for example tunnel effect trough the oxide layer.

The research on manufacturing smaller and smaller devices led to developing and studying the so called nanostructures and their properties that find their importance not only in the field of computers.

In general nanostructures are materials in which at least one dimension is smaller than $100nm$ but this definition is not so strict [22, 23]. In this type of structures the electron mean free path is greater than the size, so quantum effects are dominant and determine the electron properties. Quantum confinement can happen in one, two or three dimension leading to respectively 2D (like nanowalls or nanosheet), 1D (like nanorod or nanowire) or 0D (like nanoparticles or quantum dot) structures. A lot of new phenomena can be observed and used in this type of structures because they are quantum phenomena. For example conductance quantization appears when an electric field is applied and the Bohm-Aramov effect and Landau levels appears when a magnetic field is applied. The presence of defects lead to the phenomena of Anderson localization giving the possibility to tune the resistivity by altering the material. Combining different type of nanostructures in heterostructures can lead to objects used in every day life like gas sensors, liquid sensor, LED, Laser Diodes, Resonant Tunneling Diodes, photovoltaic cells, quantum computers and so forth. Potential applications for nanostructures are likely infinite and scientific research in this field is very active and profitable.

An important property of the nanostructures is the Surface to Volume ratio: at smaller sizes this ratio began very high. In a spherical particle, the number of surface atoms and number of the bulk atoms are linked to

the radius by the following trend:

$$\frac{N_s}{N_v} \approx \frac{1}{R} \tag{1.21}$$

This is important because all effects related to surface are enhanced when the radius is small and so when the atoms are few. In fact nanostructures are highly used for sensing because the interaction with the sensor and the gas/liquid heavily modified the surface electrical properties and so the whole electrical properties improving the sensing properties of the material.

1.4.1 Nanotechnologies for Hydrogen production

In previous Sections the current behaviour of the electrochemical cell was expressed in terms of current density (eq 1.10). In current density there is a dependence of surface, so nanostructuring the electrodes to increase its exposed surface could be an approach to reach higher performances (eq 1.21). In fact, high surface electrode can be a good starting point for the study of HER and OER. On the market nanoporous system like Nichel Foam or Copper Foam can be found at relatively low price. Also system made up by nanowires or Carbon Nanotubes are easy to produce.

Combining different materials with different performance in HER and OER is also an approach to have more powerful electrodes, in particular the use of a substrate decorated with nanostructures of different catalyst materials. Here Nanoparticles play an important role with their high surface to volume ratio and feasibility of production, but also interaction between Nanoparticles and substrate can contribute. In proximity of nanostructures the electrical double layer (Figure 1.9) behave different than near the substrate surface and also the binding energy with hydrogen atoms are different. This nanostructures can be active site for the requested reaction working like catalyst and lowering the overpotential and/or the Tafel slope. Hence in this work the characteristics of this type of system will be studied in detail.

This approach leads to the use of another important parameter in addition to Overpotential and Tafel slope: the catalyst loading or in alternative the mass activity. The **catalyst loading** is simply the mass of catalyst

on a specific surface (expressed in mg/cm^2). The **mass activity** is the density current that flow trough the catalysts (expressed in A/mg). Overpotential is evaluated for convention [12] at $10mA/cm^2$ so is the mass activity:

$$\text{Mass activity} = \frac{10mA/cm^2}{\text{Catalyst loading}} \left[\frac{mA}{mg}\right] \tag{1.22}$$

1.5 Common reported materials for HER and OER

As seen in Figure 1.7, best metals for HER are Platinum, Rhenium, Rhodium and Iridium. Also, HER works better in acidic conditions because of the higher concentration H^+ ions that can be easily adsorbed on the metal surface. Precious metals like Platinum are very stable in every condition, but more common materials like Copper, Nickel or Iron are heavily affected by the acidic condition and electrodes will be destroyed rapidly during the use.

The best exploited materials for OER are RuO_2 and IrO_2 [9], but also some alternatives like perovskites, spinels and metal chalcogenides are investigated and presents good performance.

1.5.1 Low cost metals

Platinum and Iridium are very rare, expensive and difficult to mine [24], so now the scientific community is focusing on find some cheap and common and eventually easily synthesizable materials.

A little below the top of volcano plot (Figure 1.7) there are Gold, Nickel, Copper and Iron. Except for Gold, the others are cheap and abundant, but high reactive to the acids. A solution to prevent the corrosion of these metals is to work in alkaline conditions [24]. Another solution is to create nanostructures to increase surface area and to create active spots that act like catalyst for the reaction. Some reviews [13, 25, 26] reports good results for catalyst made up by Nickel and Copper for HER. Even alloys and other chemical composites result to be competitive.

Some reviews [9, 27] in the field of OER shows that hydroxides and oxyhydroxydes made up of transition metals works good and the behaviour $Ni > Co > Fe > Mn > Cr$ is observed in catalyst performance.

Also Nanoparticles and nanostructures in general are used and leads to valuable results. This is why one of the research main topic is about the use of nanotechnology to equal and surpass the results already obtained with precious element combined with low cost and non-polluting techniques and materials.

However the starting point is the study of the bare substrate and then analyze the effect of nanostructures to find the best combinations.

1.5.2 State of the art

The state of the art in electrode manufacturing for HER and OER is here briefly summarized by some reviews. Most of them reports only the Overpotential and Tafel slope [9, 13, 25, 27, 28] because most works focus only on this values and don't report the mass activity or other parameters (several relevant data are collected in Tables 1.4 and 1.5). A complete collection of data about catalyst loading and mass activity is given by [24] and reported in Figures 1.12 and a selection of most relevant data is collected in Tables 1.2 and 1.3. Catalyst loading is reported in $\mu g/cm^2$ to stress the fact that a very few amount of catalyst is used.

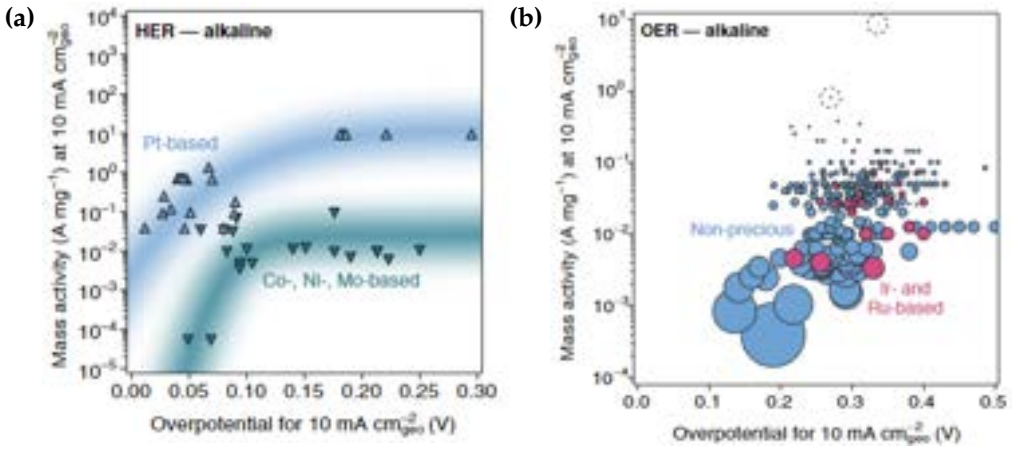

Figure 1.12: (a): Representation of data in Table 1.2, **(b)**: Representation of data in Table 1.3[24].

Material	Catalyst loading ($\mu g/cm^2$)	Overpotential (mV) at $10 mA/cm^2$
	acidic	conditions
MoS_2/rGO	280	154
$[Mo_3S_{13}]^2$-clusters	10	180
$Co_xFe_{1-x}P$ nanocubes	350	72
$Fe_{0.5}Co_{0.5}P$ thin film	250	160
$Fe_{0.25}Co_{0.75}P$ thin film	250	158
Fe_2P thin film	250	192
Ni_2P thin film	250	210
$MoP\|S$ thin film	250	132
C-shell coated FeP/C NP	440	71
$Ni2P$@NPCNFs	337	63
$N@MoPCx$-800	140	108
CoP@NC-NG	280	135
Pt NP	1	32
ALD50 Pt/NGN	1.58	40
10Pt@HN-BC	12	47
Pt NIs@f-MWCNT	3.8	84
Pt-GT-1	1.4	18
O_2-based ALD Pt	3.5	48
N_2-based ALD Pt	3.5	46
400-SWNT/Pt	0.57	27
Pt/C	20	25
PtNP/OMC	1	32
Pt/vulcan	1	30
Pt/Mxene	12	30
	alkaline	conditions
$Ni_{0.33}Co_{0.67}S_2$ NWs	300	88
NiO/Ni-CNT	280	80
CeO_2/Ni-CNT	140	91
Co/Co_3O_4-nanosheets	850	100
CoP/CarbonCloth	920	250
MoC_x	800	151
Mo_2C@NC	280	60
Mo_2C NP	102	176
$PtCo-Co$/TiM	43	28
$Pt/C/Ni(OH)_2$	60	90
Pt NWs/SL-$Ni(OH)_2$	16	48
Pt_3Ni_3 NWs/C-air	15	40
$Pt/NiO@Ni$/NF	92	34
Pt/C	286	46
$Pt@Ni$/NF	113	51
Pt	1	295

Table 1.2: Some of the most important results in HER, data from [24] reporting Overpotential at $10 mA/cm^2$ and catalyst loading.

Material	Catalyst loading ($\mu g/cm^2$)	Overpotential (mV) at $10 mA/cm^2$
	acidic	conditions
$K_{x\approx 0.25}IrO_2$	200	350
$3RuO_2@SiO_2$	750	297
$2RuO_2@C@SiO_2$	740	270
$IrNi$ NCs	13	280
$IrO_x - Ir$	133	293
Ir-black	133	331
$Bi_2Ir_2O_7$	402	360
$IrO_2 - RuO_2@Ru$ (3:1)	379	281
Ir_3RuO_2	379	293
RuO_2 (CM)	379	289
$IrOOH$ nanosheet	200	344
6H-$SrIrO_3$	900	248
IrO_2	900	300
$Cr_{0.6}Ru_{0.4}O_2$	279	178
$Ru_1 - Pt_3Cu$	16	220
	alkaline	conditions
$Fe - Ni$ NP	29	311
3DGN/$CoAl$-NS	50	252
$Ni - Fe - Se$ cages	100	240
$Ni_{2.7}Zn(OH)_x$	50	290
CFO/rGO	100	340
$CoCo$-NS	70	353
$NiCo$-NS	70	334
$NiCo_2S_4$	70	337
$NiCo_2O_4$	70	377
$Ni - Fe$ film	27	280
Co_3O_4@MWCNT	50	309
$Ni_{0.9}Fe_{0.1}O_x$	1	336
$Ni_{0.5}Co_{0.5}$/NC	100	300
Co/NC	100	384
$NiFe$/NF	32	215
$NiFe$-LDH	100	270
NiO	140	364
Ni	140	377
IrO_x	136	393
$IrNi$ NCs	13	270
IrO_2	140	330
RuO_2	130	350
Ir/C	28	380
Ru/C	28	390
Commercial IrO_2/C	360	400
IrO_2 NPs	200	339

Table 1.3: Some of the most important results in OER, data from [24] reporting Overpotential at $10 mA/cm^2$ and catalyst loading.

Material	Overpotential (mV) at $10 mA/cm^2$	Tafel slope (mV/dec)
Reference [13]		
$CuTi$ NP	50	110
NiO/Ni/CNT	80	82
Ni_3P NP	291	119
$Pt-Co_2P$	2	44
Pt/C	20	65
Rh_2P NF	9	38
Ni_3N NF	45	97
CoNPs/N-rGO	59	105
$Ni(Cu)VO_x$NF	21	28
Ni/NiO	90	41
$Ni-S-OH$ NF	179	120
Reference [28]		
$NiMo$	$185(20\frac{mA}{cm^2})$	112
MoS_2	150	41
FeP	55	38
Ni/C	34	41
$Cu_{95}Ti_5$	60	110
Reference [25]		
$NiMo$ nanopowder	$70(20\frac{mA}{cm^2})$	–
CoP on Ti	$85(20\frac{mA}{cm^2})$	–
Ni_2P	$130(20\frac{mA}{cm^2})$	–
MoS_2 rGO	150	–
Pt/C	$50(20\frac{mA}{cm^2})$	–

Table 1.4: Some of the most important results in HER, data from various reviews reporting Overpotential at $10 mA/cm^2$ and Tafel slope.

Material	Overpotential (mV) at $10 mA/cm^2$	Tafel slope (mV/dec)
Reference [28]		
$NiFe$ oxides	300	40
$CoMnP$	330	61
Ni oxides	320	52
Reference [9]		
RuO_2 on Ti	$240(1\frac{mA}{cm^2})$	39
RuO_2 on FTO	358	55
IrO_2 on Ir	$270(1\frac{mA}{cm^2})$	91
IrO_2 on Ti	$290(1\frac{mA}{cm^2})$	61
$CaFeO_3$ on GCE	390	47
$COFe_2O_4$on GCE	370	82
Co_3O_4 NP on GCE	530	49
Co_3O_4 nanocube on GCE	580	60
$CoCr_2O_4$/CNT on GCE	326	51
$NiOOH$ on Pt/Au	$375(5\frac{mA}{cm^2})$	–
$Ni(OH)_2$ on Au	$410(1\frac{mA}{cm^2})$	–
Reference [27]		
$Cu-Ir$	286	44
Cu@$NiFe$ porous NP	199	28
Cu@$graphidyne/Co$ nanotube	$311(500\frac{mA}{cm^2})$	148
CuO nanofibers	475	59
$CuFe_2O_4$ NP	340	94
$CuNiO_x$ nanosheet	350	120
$Cu-Pt$ core-shellNP	200	–
$Cu/Cu_2O/CuO$ porous NP	290	64
Cu_2O/Cu core-shell nanorods	350	68
$NiCuP$ porous	300	49
$CuCoO$ nanowires	320	68
Cu_3P/C NP	320	51
$NiFe/Cu_2O$ nanowires	215	42

Table 1.5: Some of the most important results in OER, data from various reviews reporting Overpotential at $10 mA/cm^2$ and Tafel slope.

1.6 Aim of this work

The aim of this work is to find and study a low cost and non pollutant alternative electrodes good for both HER and OER using nanostructures fabricated in a simple way.

In particular Copper and Nickel NPs were synthesized using Pulsed Laser Ablation in Liquid technique. These NPs were, then, characterized using various instrument and analysis. Then electrodes were created depositing NPs on different substrates and performance in HER and OER were evaluated. In this work only few amount of NPs will be used, trying

to find a competitive alternative to Platinum and Iridium catalyst in HER and OER [24].

The reason that lies behind the use of Pulsed Laser Ablation in Liquid is that is rapid and cheap, and does not create waste and does not require big apparatus, but only a laser [29]. This could be an alternative to industrial methods for NPs synthesis that involve sputter and dewetting techniques. In fact an alternative way to directly produce electrodes decorated with NPs involves a thin film deposition using sputter: once the sample is loaded in the machine the vacuum condition must be reached and the chamber filled with an inert gas whose atoms are ionized and accelerated toward the metal target. The impact extract atoms from the target that travel in the chamber and reach the substrate and form a film, but a lot of atoms reach also the chamber walls and so are wasted. Once the thin film is formed a thermal processing is needed to bring the film in the liquid phase and agglomerate in NPs (dewetting). This can be performed into a oven (also vacuum and inert gas are required) or with laser irradiation. This last process is performed in air so the hot NPs can oxidize. However the high temperature can induce some irreversible modification to the substrate. The overall process requires a lot of time, equipment and steps and the amount of catalyst must be choose first.

Pulsed Laser Ablation in Liquid instead create NPs simply shooting a laser beam on to a target that lies in a liquid and so the NPs are stored in the same solvent, so do not react with air and can be stored for long time. Electrodes are created simply by dropping some drops of solution on the substrate and let it dry. The amount and also the spatial distribution of catalyst on the substrate is easily controlled and performed without special equipment. The overall process to create NPs is easy, rapid and cheap and can hopefully help the industrialisation of Hydrogen production.

1.6.1 Next Chapters

Next Chapters will be about:

- Synthesis and characterization of NPs: first the theory of Pulsed Laser Ablation in Liquid (PLAL) is explained; then the produced solution of NPs are presented and analyzed with UltraViolet - Visible -

Near InfraRed (UV-Vis-NIR) spectrophotometry, Scanning Electron Microscopy, Transmission Electron Microscopy, X-Ray Diffraction, X-Ray Photoelectron Spectroscopy and Energy Dispersive X-Ray; in the end theoretical considerations and simulation are conducted to understand the nature of NPs.

- Electrodes preparation and characterization: first the production parameters of the electrodes are presented and some analysis are conducted to quantify and qualify the NPs on the electrode using Rutherford Backscattering Spectrometry and Scanning Electron Microscopy; then electrochemical measurements (Cyclic Voltammetry, Linear Sweep Voltammetry, Electrochemical Impedance Spectroscopy, Mott Schottky); in the end results are explained with theoretical considerations.

Bibliography

[1] Péter Kádár. Pros and cons of the renewable energy application. *Acta Polytechnica Hungarica*, 11(4):211–224, 2014.

[2] 12 important pros and cons of renewable energy to consider. https://blog.ecoflow.com/us/pros-and-cons-of-renewable-energy/.

[3] E. Rebhan. Challenges for future energy usage. *The European Physical Journal Special Topics*, 176(1):53–80, September 2009. doi:10.1140/epjst/e2009-01148-9.

[4] Electricity production by source, world. https://ourworldindata.org/energy-key-charts.

[5] Ibrahim Dincer and Canan Acar. Review and evaluation of hydrogen production methods for better sustainability. *International Journal of Hydrogen Energy*, 40(34):11094–11111, September 2015. doi:10.1016/j.ijhydene.2014.12.035.

[6] High and low heat values. https://www.engineeringtoolbox.com/gross-net-heating-value-d_824.html.

[7] C.G. Zoski. *Handbook of Electrochemistry*. Elsevier Science, 2007. URL: https://books.google.it/books?id=2g5GJtBFwo0C.

[8] Reference electrode potentials. https://www.edaq.com/wiki/Reference_Electrode_Potentials.

[9] Nian-Tzu Suen, Sung-Fu Hung, Quan Quan, Nan Zhang, Yi-Jun Xu, and Hao Ming Chen. Electrocatalysis for the oxygen evolution reaction: recent development and future perspectives. *Chemical Society Reviews*, 46(2):337–365, 2017. doi:10.1039/c6cs00328a.

[10] A.J. Bard and L.R. Faulkner. *Electrochemical Methods: Fundamentals and Applications*. Wiley, 2000. URL: https://books.google.it/books?id=kv56QgAACAAJ.

[11] Tatsuya Shinagawa, Angel T. Garcia-Esparza, and Kazuhiro Takanabe. Insight on tafel slopes from a microkinetic analysis of aqueous

electrocatalysis for energy conversion. *Scientific Reports*, 5(1), September 2015. doi:10.1038/srep13801.

[12] Chao Wei and Zhichuan J. Xu. The comprehensive understanding of 10 mA cmgeo-2 as an evaluation parameter for electrochemical water splitting. *Small Methods*, 2(11):1800168, July 2018. doi:10.1002/smtd.201800168.

[13] Thomas B. Ferriday, Peter Hugh Middleton, and Mohan Lal Kolhe. Review of the hydrogen evolution reaction—a basic approach. *Energies*, 14(24):8535, December 2021. doi:10.3390/en14248535.

[14] Sergio Trasatti. Work function, electronegativity, and electrochemical behaviour of metals. *Journal of Electroanalytical Chemistry and Interfacial Electrochemistry*, 39(1):163–184, September 1972. doi:10.1016/s0022-0728(72)80485-6.

[15] Allen J. and Larry R Faulkner. *Electrochemical Methods*. John Wiley & Sons, Nashville, TN, 2 edition, December 2000.

[16] Keith B Oldham and Janice C Myland. *Fundamentals of Electrochemical Science*. Academic Press, San Diego, CA, January 1994.

[17] Norio Sato. *Electrochemistry at metal and semiconductor electrodes*. Elsevier Science, London, England, October 1998.

[18] K. Gelderman, L. Lee, and S. W. Donne. Flat-band potential of a semiconductor: Using the mott–schottky equation. *Journal of Chemical Education*, 84(4):685, April 2007. doi:10.1021/ed084p685.

[19] Kevin Sivula. Mott–schottky analysis of photoelectrodes: Sanity checks are needed. *ACS Energy Letters*, 6(7):2549–2551, July 2021. doi:10.1021/acsenergylett.1c01245.

[20] Moore's law - ourworldindata. https://ourworldindata.org/grapher/transistors-per-microprocessor.

[21] Gordon E. Moore. Cramming more components onto integrated circuits, reprinted from electronics, volume 38, number 8, april 19,

1965, pp.114 ff. *IEEE Solid-State Circuits Society Newsletter*, 11(3):33–35, September 2006. doi:10.1109/n-ssc.2006.4785860.

[22] Paul N Butcher, Norman Henry March, and Mario P Tosi, editors. *Physics of low-dimensional semiconductor structures*. Physics of Solids and Liquids. Springer, New York, NY, June 2013.

[23] David Ferry and Stephen Marshall Goodnick. *Cambridge studies in semiconductor physics and microelectronic engineering: Transport in nanostructures series number 6*. Cambridge University Press, Cambridge, England, October 1999.

[24] Jakob Kibsgaard and Ib Chorkendorff. Considerations for the scaling-up of water splitting catalysts. *Nature Energy*, 4(6):430–433, May 2019. doi:10.1038/s41560-019-0407-1.

[25] Ming Gong, Di-Yan Wang, Chia-Chun Chen, Bing-Joe Hwang, and Hongjie Dai. A mini review on nickel-based electrocatalysts for alkaline hydrogen evolution reaction. *Nano Research*, 9(1):28–46, December 2015. doi:10.1007/s12274-015-0965-x.

[26] Xing-Xing MA, Li CHEN, Zhe ZHANG, and Ji-Lin TANG. Electrochemical performance evaluation of CuO@cu2o nanowires array on cu foam as bifunctional electrocatalyst for efficient water splitting. *Chinese Journal of Analytical Chemistry*, 48(1):e20001–e20012, January 2020. doi:10.1016/s1872-2040(19)61211-9.

[27] Zhenyi Zhou, Xinran Li, Qing Li, Yan Zhao, and Huan Pang. Copper-based materials as highly active electrocatalysts for the oxygen evolution reaction. *Materials Today Chemistry*, 11:169–196, March 2019. doi:10.1016/j.mtchem.2018.10.008.

[28] Isolda Roger, Michael A. Shipman, and Mark D. Symes. Earth-abundant catalysts for electrochemical and photoelectrochemical water splitting. *Nature Reviews Chemistry*, 1(1), January 2017. doi:10.1038/s41570-016-0003.

[29] Stephan Barcikowski, Vincenzo Amendola, Galina Marzun, Christoph Rehbock, Sven Reichenberger, Dongshi Zhang, and

Bilal Gökce. Handbook of laser synthesis of colloids. 2016. URL: http://duepublico.uni-duisburg-essen.de/servlets/DocumentServlet?id=41087, doi:10.17185/DUEPUBLICO/41087.

Chapter 2

Synthesis and characterization

This Chapter will describe the techniques for the synthesis and the morphological, structural, compositional characterization of the Copper- and Nickel-based NPs. First, NPs are produced via Pulsed Laser Ablation in Liquid and stored at $4°C$ in the same solvent in which they are produced to avoid air contamination and prevent agglomeration. Then analysis were conducted to evaluate morphology, structure and composition of the NPs.

2.1 Pulsed Laser Ablation in Liquid

Pulsed Laser Ablation in Liquid (PLAL) is a recent technique allowing a fast and easy production of colloidal solution. The main advantage of this technique is that it works at room temperature and pressure and does not require furnace or pressure systems like other techniques [1, 2]. Figure 2.1 shows the Pulsed Laser Ablation in Liquid (PLAL) set-up scheme and the he fundamental processes acting at the surface of the target interacting with the laser beam.

The experimental apparatus requires an optical table that prevent external movement to affect the system. Laser beam starts horizontally and a reflective mirror deflects the laser beam at 90°. Then a convex lens focus the laser beam toward a Teflon vessel containing a solid target immersed on a liquid. The lens can be moved upside down to change the spot area.

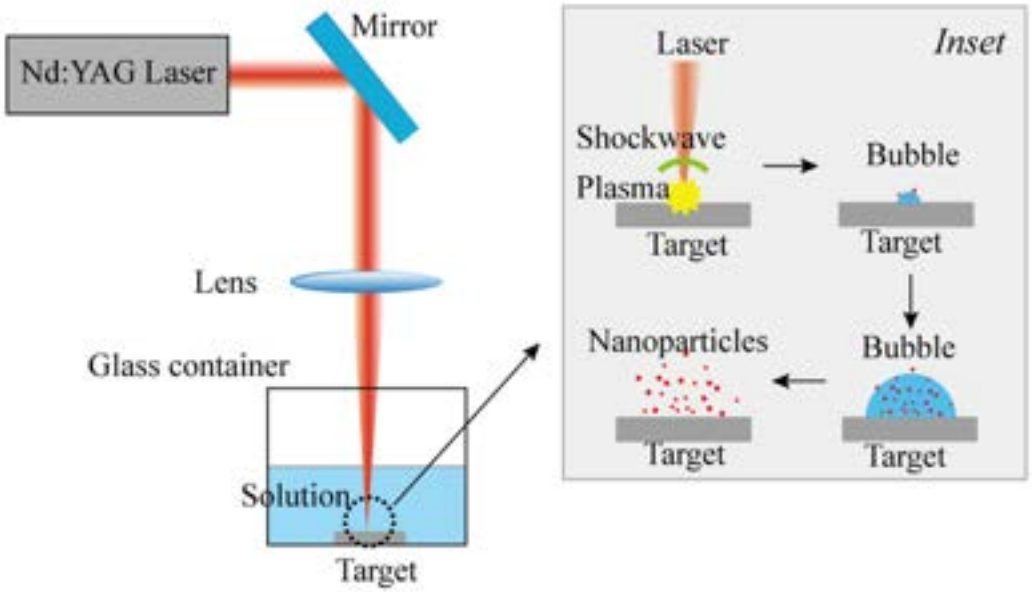

Figure 2.1: Typical scheme of Pulsed Laser Ablation in Liquid apparatus and schematic of the NP creation mechanism [3].

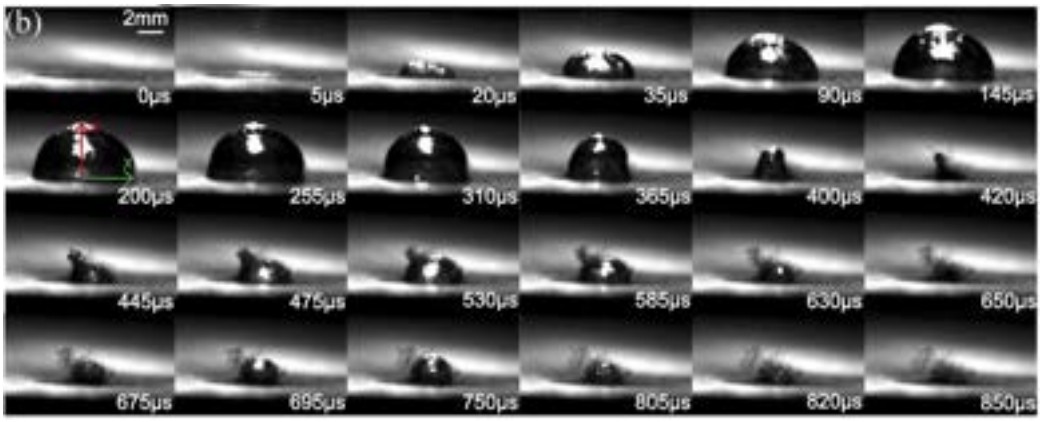

Figure 2.2: Cavitation bubble behaviour in time obtained with high speed camera [3]. After bubble collapsing, a smaller one is created.

When the laser beam collides on the target, the high energy in small area leads to formation of plasma and a shockwave. This shockwave leads the formation of a cavitation bubble of liquid vapour due to the energy

exchange between the plasma phase and the liquid environment. The cavitation bubble expands really fast and cool down. In the hot spot, the target material breaks in some NPs that are carried away by the bubble expansion and are released in the solution.

NPs only interact with the solvent and are not exposed to air. Thus, NPs purity depends only on the solvent and target purity. With Gold and Platinum almost every solvent produce pure metallic NPs, but ablating transition metals in different solvents typically leads to oxide-based NPs synthesis [2]. For example, in literature it has been reported that Copper target ablated in water leads to the production of Cu_2O NPs [4], while in organic solvent Cu metallic spheres are mainly synthesized, but also nanorods and nanocubes formation have been reported due to different experimental conditions [5]. Confinement of NPs in the solution prevents the releasing of NPs in air, so the technique is safe for operators.

2.1.1 Laser parameters

The solvent is important because establishes the composition of the nanostructures. Also, other NPs properties, such as size, are strictly correlated to the laser parameters.

First of all laser must be a pulsed laser and not a continuous one. The reason behind that are that laser pulses carries a lot of power with respect to a continuous one. For example $1ns$ pulse of $250\mu J$ have a peak power of $P = E/t = 2.5 \cdot 10^{-4} J / 10^{-9} s = 2.5 \cdot 10^5 W = 0.25 MW$ [2]. All this power allows the laser to locally melt the target digging a hole in it while all the extracted and dispersed material are the so wanted NPs.

The rate of ablation, setting the **productivity** of the technique is a parameter that measure the efficiency of the process and can be expressed in mass of ablated target per time [2]. The productivity depends on some other important laser parameters: wavelength, fluence and pulse duration [6].

At small **wavelength** (UV light) the energy that every photon carries is higher than IR light, so photons can trigger more electron transitions inside the target. Therefore, the productivity of an UV laser is higher than

an IR laser. Also, shorten wavelengths mean higher cross section[1], this means that NPs dispersed in solution absorb and drastically attenuate the beam in UV. The attenuation is present also in IR, but the effect is much lower. In general IR lasers are preferable because the productivity does not vary significantly during the ablation process (Figure 2.3) and also they are cheaper than UV laser.

Laser **fluence** is defined as:

$$F = \frac{\text{Pulse energy}}{\text{Laser spot area}} \left[\frac{J}{cm^2}\right] \tag{2.1}$$

Productivity has been observed to go logarithmic with fluence (Figure 2.4). The reason behind this behaviour is that at fixed spot area, higher energy can dig deeper in the target and pull away more material. While at fixed energy, a low surface helps to concentrate the energy which otherwise will be dispersed on the target. The spot area depends on the lens position or working distance.

Pulse duration is also important because shorter pulses do not give the target enough time to dissipate the heat and so all the material in the region affected by the pulse is extracted. As shown in Figure 2.5 productivity drastically decrease with the pulse duration. Actually, femtosecond ($10^{-15}s$) lasers are the best for PLAL, but nanosecond ($10^{-9}s$) lasers are more common and cheaper. If pulse duration is lesser than electron phonon scattering, it is called "cold ablation" (obtained with femtosecond lasers). Hence with greater pulse duration it is called "hot ablation" because within the laser pulse duration the electrons thermalize, heating the target [8].

The repetition rate is the number of pulses per second. With high repetition rate, the incoming pulse can encounter the cavitation bubble formed by the previous one (Figure 2.2), being attenuated and/or scattered leading to a decrease of the productivity. To prevent this, a lower repetition rate or a motorized stage for the target position can be a solution.

Particles size depends on the interaction with solvent, but also on the **ablation time**: big particles in solution have high probability to be ex-

[1]Cross section for Rayleigh scattering goes with the inverse of the square of the wavelength $\sigma \sim 1/\lambda^2$. Hence, the particles absorb mostly in the UV than in the IR [7].

posed to laser beam and be fragmented. Small particles absorb predominantly in UV range and so are likely unaffected by IR beam, whereas bigger particles mainly absorb in the IR range and have higher cross section. The size distribution of PLAL-obtained NPs tipically presents a small amount of big particles and a bigger amount of small particles following a lognormal distribution.

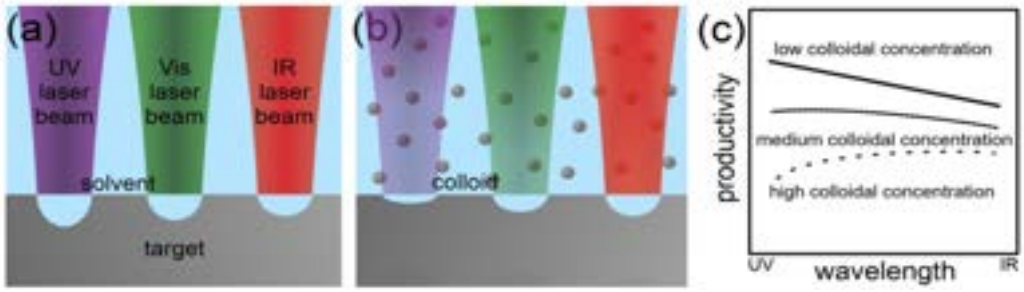

Figure 2.3: Schematic of the laser ablation of metals in liquids at different **wavelengths** in absence (a) and presence (b) of colloidal particles. Equal energy densities were assumed for all laser spots. The diagram in (c) (linear scales for both axes) demonstrates the effect of an increasing colloidal concentration on the NP productivity in PLAL at different wavelengths [6].

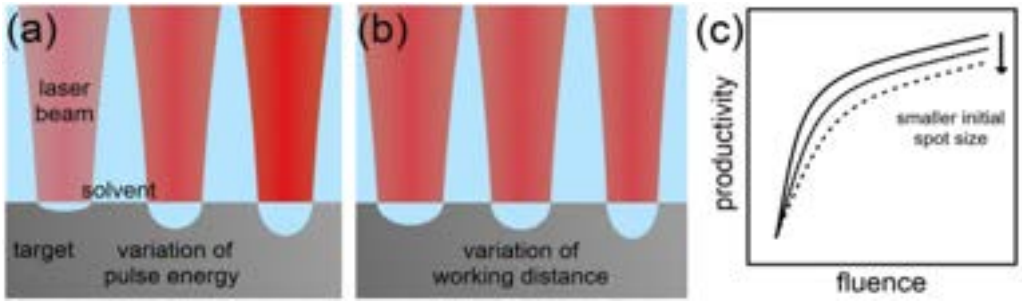

Figure 2.4: Illustration of the laser ablation of metals in liquids at different **fluences** varied by the pulse energy (a) and the working distance (b). The diagram in (c) shows how the fluence variation caused by different initial spot sizes affects the NP productivity in LAL in the high-fluence regime. A Gaussian beam profile was assumed. In (c), both axes scale linearly. The arrow and the less dense (dashed) line style in (c) indicate the trend in productivity induced by a smaller initial spot size [6].

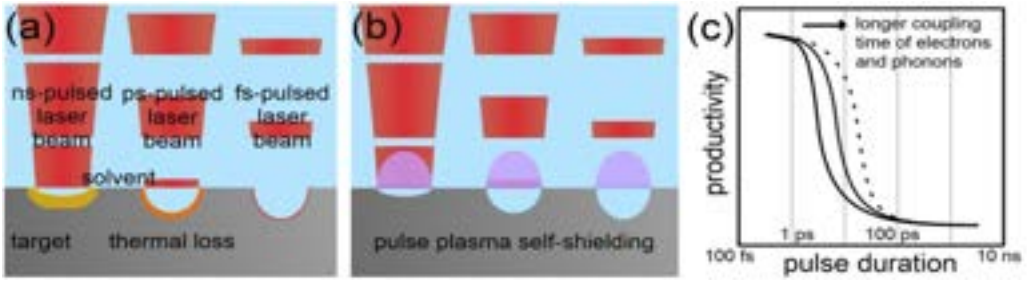

Figure 2.5: Illustration of the laser ablation of metals in liquids at different **pulse duration** neglecting non-linear effects. Thermal losses (a) and self-shielding by plasma (b) of pulses of different duration regimes. The diagram in (c) demonstrates how the coupling constant of electrons and phonons affects the NP productivity in PLAL, depending on the laser pulse duration. A change of the coupling constant was assumed to have no influence on other material properties. In (c), the y-axis scales linearly. In (c), the arrow and the less dense (dashed) line style indicate the effect of a longer coupling time of electrons and phonons of the target material on productivity [6].

2.2 PLAL produced colloidal solutions

For this work, Copper an Nickel NPs were produced using the PLAL technique in different solvent. NPs were produced using a Nd:Yttrium Aluminium Garnet (Nd:YAG) nanosecond pulsed laser. The laser is extensively described in Appendix A. Methanol and Ethanol were used as solvent because in literature PLAL in these solvents has resulted in pure metal NPs (Nickel in methanol, Copper in methanol) and oxide-based NPs (Copper in methanol), while in pure water oxides are produced [5, 9, 10]. The reason behind this choice is that Nickel, Copper and Copper oxide are good catalysts for HER and OER as reported in Tables 1.2, 1.3, 1.4 and 1.5. Organic solvent may seem dangerous because their vapour can burn due to laser beam, but some practical precautions avoid this.

Copper and Nickel target were polished with isopropylic alcohol to remove surface impurity and then weighted with a microbalance `Sartorius M5` ($100\mu g$ precision). Targets were placed at the bottom of a Teflon vessel then filled with $8ml$ of solvent. Laser parameters: $10ns$ pulses at $1064nm$ wavelength, repetition rate $10Hz$, mean output power $5W$. The focusing

lens was placed at $9cm$ respect to the target to avoid solvent vapours to condense on the lens surface and burn. In Table 2.1 are reported the produced solutions, the used solvent and the ablated mass. The ablated mass is obtained by weighting the target after the ablation and find the mass difference before and after.

The laser used in this work produces pulses of $500mJ$, that is ~ 2000 times more energetic than the laser used for other works [5, 9, 10]. This different energy will lead to new phenomena resulting from the interaction between the laser and the target even different from literature.

Sample name	Solvent	Ablation time	Ablated mass
Cu_met	methanol	8 min	$0.09mg$
Cu_et	ethanol	10 min	$0.13mg$
Ni_met	methanol	10 min	$0.40mg$

Table 2.1: NPs solutions summary.

Within the same solvent (methanol) and in the same time (10 minute) Nickel has a higher ablation yield than Copper (about $4:1$). The Copper ablated mass is similar for methanol $0.09mg$ and for ethanol $0.13mg$. Ablation time was chosen after some attempts to have slightly the same ablated mass for Copper.

From Figure 2.6 is possible to see slightly different shades of colours of the obtained solutions. In particular the solution of Copper in ethanol resulted slightly pink, while Copper in methanol is slightly grey and Nickel in methanol is more transparent.

Solutions were stored at $+4°C$. After two days the solutions show dark sediment on the bottom of the storing vials. This is not surprising because NPs tends to aggregate to minimize surface energy [2]. To prevent this, some surfactant (usually organic molecules) can be added to the solution and cover the whole surface of the metal particles bonding with some surface atoms. This layer prevents bonds whenever particles collide for brownian motion. For our purpose, pure NPs are needed, so no surfactant were added. Before performing analysis, solutions were handshaked and sonicated for 15 minute to break agglomeration and redisperse the NPs.

Figure 2.6: NPs solutions, from left to right: *Cu_et*, *Cu_met*, *Ni_met*.

2.3 Measurement and analysis

In this Section all the measures and the analysis conducted on the NPs are presented with a first interpretation of the data.

2.3.1 UV-Vis-NIR spectroscopy measurement

The optical measurement on the NPs solution were conducted using the `Varian Cary 500 Spectrophotometer` described in the Appendix B.

A quartz cuvette was used for the optical measurements. The absorption spectrum was acquired in range $200 - 1070nm$ to cover UV strong absorption and the visible range in which plasmonic peaks of Copper appear. The spectra were acquired on the as prepared solution and after two days.

Absorption spectra of Copper solutions just after the synthesis (Figure 2.7(a)) show both a clear peak around $600nm$ and a large shoulder at higher wavelengths that slowly decrease to zero as expected in the IR region. At lower wavelengths the absorption increase as expected in the UV region. The central peak clearly refers to a plasmonic peak that clearly identify the metallic Copper [11, 12, 13, 14]. According to the Mie theory, the position and shape of this peak depends on the shape and size of the NPs and can be also affected by a shell oxide that shift them at higher wavelengths.

Nickel solution instead presents a smooth behaviour at high wavelenghts, a peak near $320nm$ and a significant absorption toward the UV. Also in this case, the peak position depends on the NPs morphology and gives sign of the metallic Nickel presence [11, 15, 16].

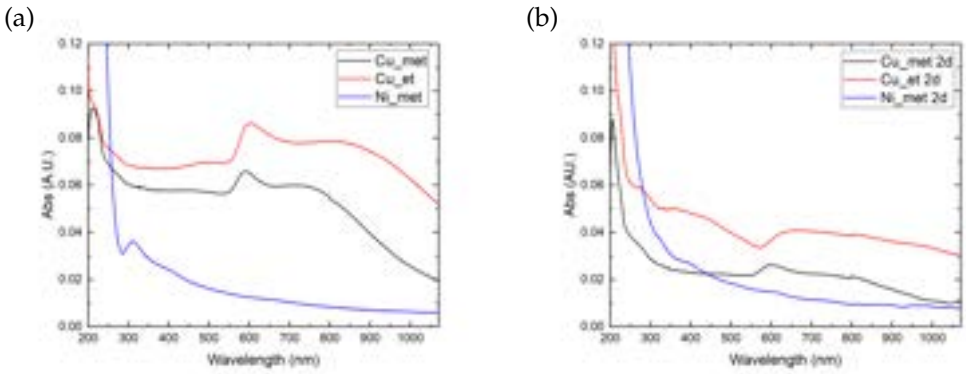

Figure 2.7: (a): Absorption spectra of NPs solutions after synthesis and **(b)**: absorption spectra of NPs solutions after two days in the fridge.

Figure 2.7(b) shows the absorption spectra after two days. All samples present a smoother behaviour with high absorption in UV and low absorption in IR. *Cu_met* still presents its peak at $\sim 600nm$, *Cu_et* completely loose their characteristics and *Ni_met* become very smooth with a barely perceptible peak at $\sim 320nm$. This change is due to agglomeration of NPs that was not completely broken by the sonication process.

2.3.2 Scanning Electron Microscopy

Scanning Electron Microscopy (SEM) analysis (see appendix C) where conducted to first obtain a morphological information on NPs. Samples were prepared by drop cast $20\mu l$ of solutions on a Silicon substrate (rinsed with deionized water and dried in N_2) and then dried on a hot plate. Particles analysis were conducted using ImageJ software [17].

2.3.2.1 Copper in methanol

Figure 2.8 shows **Copper** NPs produced in **methanol**. In Figure 2.8(a) lot of NPs are widely distributed on the substrate. Some NPs have size close to the SEM resolution. High magnification images show also some agglomerates of two or more particles and a non perfect circular shape suggesting a spherical shape.

Size distribution analysis was conducted setting a brightness threshold in ImageJ software and using the automatic algorithm of the software that counted 1008 particles, this thanks to the sharp contrast between the particles and the substrate. Another threshold was set on the dimension because particles smaller than $15nm$ radius are barely visible or not well defined. A check in order to verify the accuracy of the algorithm result was done. The NPs distribution in Figure 2.8(d) shows a lognormal trend, as already reported in literature regarding PLAL-based NPs production [2]:

$$f(x) = \frac{1}{xw\sqrt{2\pi}} exp\left(-\frac{ln^2(x/x_c)}{2w^2}\right) \tag{2.2}$$

where x_c is the median of the distribution and w is the scale parameter related to the distribution width. The peak value (the distribution mode) is given by $x_p = exp(ln(x_c) - w^2)$ while the mean value is given by $x_m = exp(ln(x_c) + w^2/2)$. A geometric standard deviation can be defined as $\sigma = ln(w) = \sqrt{(\sum_i n_i(ln(x_i) - ln(x_c))^2) \,/\, \sum_i n_i}$. The distribution is not symmetric so this two parameters will be reported for now on instead of mean and standard deviation. This distribution is the statistical result of the multiplicative product of many independent random positive variables and so $f(x)$ goes to zero with x [18, 19].

For these NPs the statistic shows a large amount of small particles

and few bigger ones. The fitted distribution curve reports $x_c = 47nm$ and $w = 0.67$ with the most representative value $x_p = 30nm$.

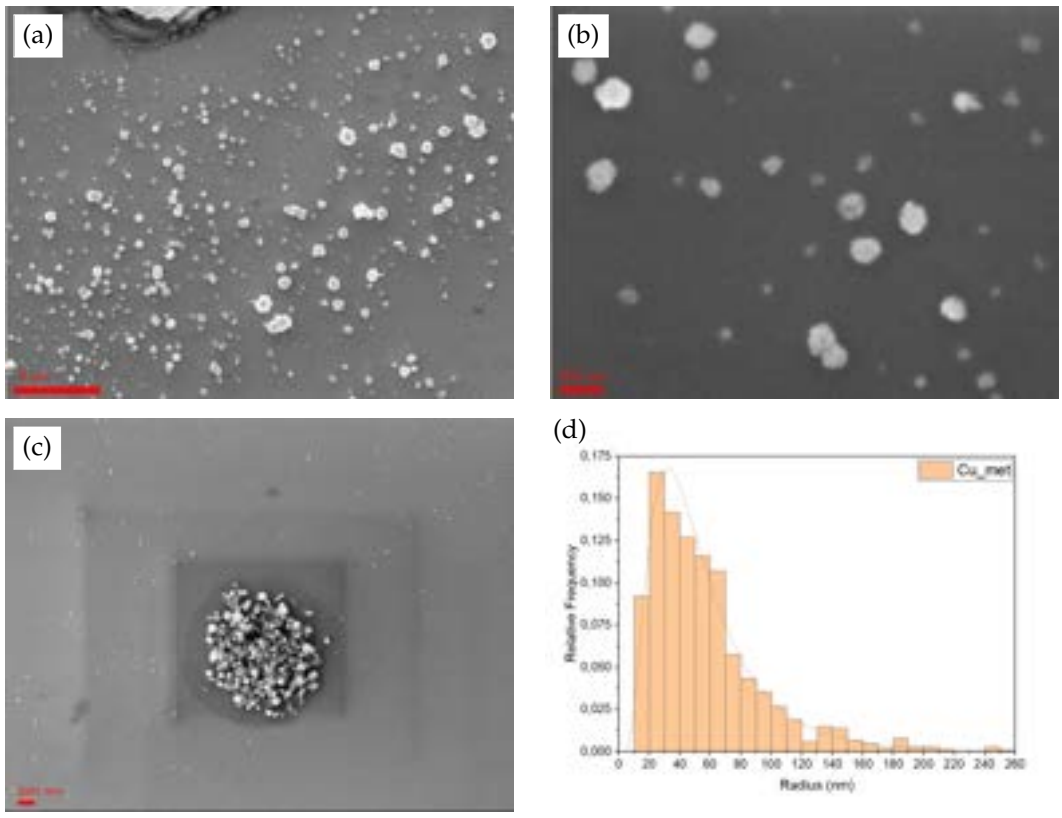

Figure 2.8: (a),(b),(c): *Cu_met* NPs on Silicon substrate at different magnification. **(d)**: Statistic of 1008 particles fitted with a lognormal distribution ($x_c = 47nm$, $w = 0.67$).

2.3.2.2 Copper in ethanol

Figure 2.9 shows SEM images of **Copper** NPs produced in **ethanol** at different magnifications. An overall inspection shows big NP clusters (Figures 2.9(a) and 2.9(b)), but a close inspection shows small particles between the clusters (Figure 2.9(c)). All these small particles seem to be circular or at least ellipsoidal. The Copper in ethanol presents an higher aggregation degree than in methanol.

Size distribution analysis in Figure 2.9(d) was conducted by measuring each particle outside the clusters (the ones inside the clusters were not distinguishable). In total 135 particles were measured and their size distribution follows a lognormal distribution. The fitted distribution curve reports $x_c = 43nm$ and $w = 0.69$ with the most representative value $x_p = 28nm$.

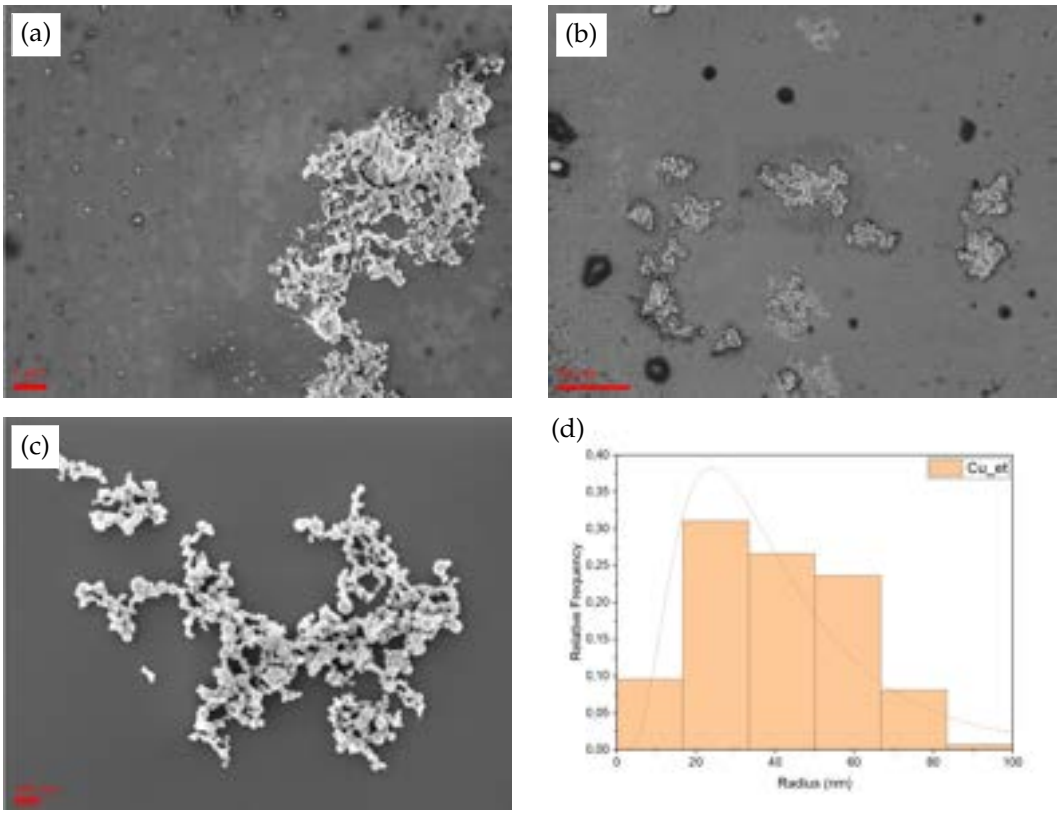

Figure 2.9: (a),(b),(c): *Cu_et* NPs on Silicon substrate at different magnification. **(d)**: Statistic of 135 particles fitted with a lognormal distribution ($x_c = 43nm$, $w = 0.69$).

2.3.2.3 Nickel in methanol

Figure 2.10 shows SEM images of **Nickel** NPs produced in **methanol** at different magnifications. Big linear cluster are made up by giant spherical

particles and some jagged frames. High magnification images show small particles all around giant particles and between the clusters forming other smaller clusters, but too small to be distinguishable.

Size distribution analysis in Figure 2.10(d) was conducted by measuring one by one the particles of the clusters counting 487 particles whose size distribution follows a lognormal distribution. The fitted distribution curve reports $x_c = 484nm$ and $w = 0.47$ with the most representative value $x_p = 388nm$.

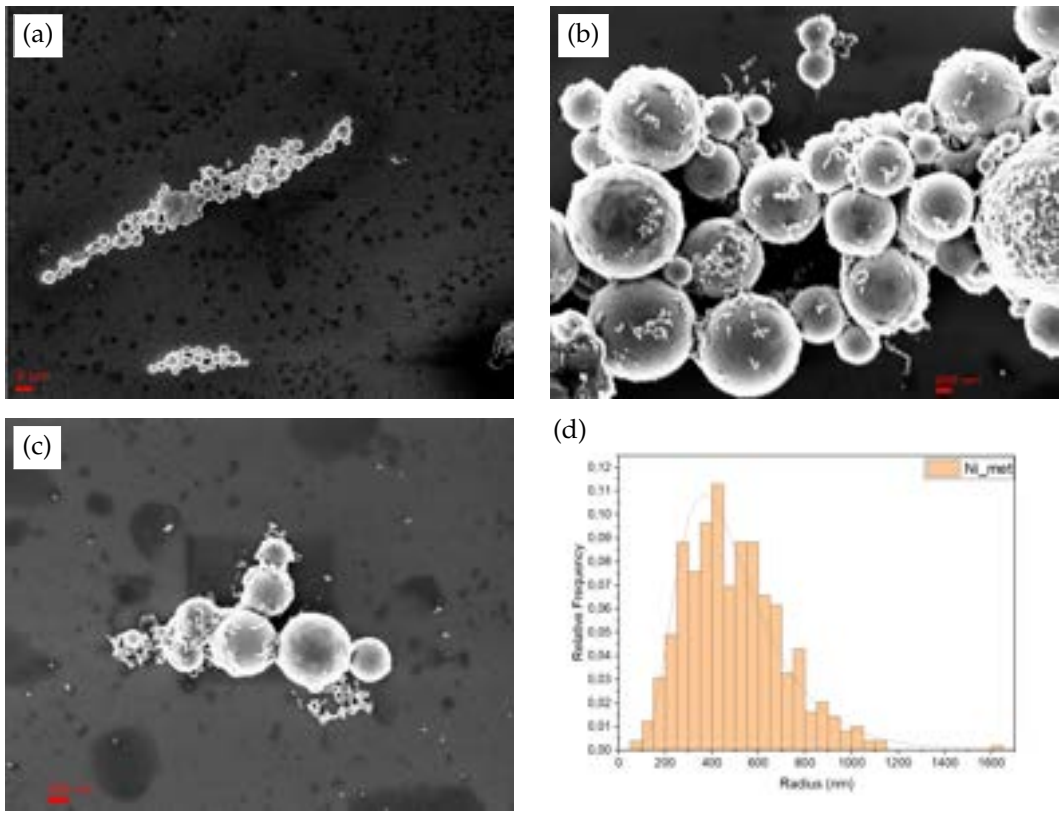

Figure 2.10: (a),(b),(c): *Ni_met* NPs on Silicon substrate at different scales. **(d)**: Statistic of 487 particles fitted with a lognormal distribution ($x_c = 484nm$, $w = 0.47$).

2.3.3 Transmission Electron Microscopy

Transmission Electron Microscopy (TEM) analysis (see appendix D) was conducted in order to obtain a more detailed morphological information on small particles not accessible with the SEM. High resolution TEM provides information also on the crystallinity of the particles which allows extracting compositional informations. Only Copper solutions were examined (both methanol and ethanol) due to lab disposability. Samples were prepared by drop cast some μl of sonicated solution on a `Carbon lacey` grid.

2.3.3.1 Copper in methanol

Figure 2.11 shows a collection of **Copper** NPs produced in **methanol** at different magnifications. Figures 2.11(a), 2.11(b), 2.11(c) and 2.11(d) show a large amount of particles of very different sizes. Most of them are circular, but some particles appears ellipsoidal maybe because they are the aggregate of two smaller particles. In Figure 2.11(b) some NPs present white stripes. These are the Moire patterns formed due to the superposition of two different lattices with small differences. In Figure 2.11(d) the crystal planes of some particles are clearly visible. These TEM images allowed to extract structural information about the NPs.

Size distribution analysis in Figure 2.11(f) was conducted by measuring one by one the particles that appear distinguishable. In total 892 particles were measured and their size follows a lognormal distribution with a fitted curve that reports $x_c = 2.1nm$ and $w = 0.62$ with the most representative value $x_p = 2.0nm$. This distribution indicates a dimension much smaller then the one obtained with SEM analysis in Figure 2.8(d) because of the higher resolution of the TEM. Also the bigger particle observe with SEM here are not present: the size distribution of Figure 2.11(f) stops at $\sim 20nm$ radius. Figure 2.11(e) shows a big particle that turns out to be formed by many small agglomerated particles. This indicates that the big particles observed with SEM are nothing but agglomerates.

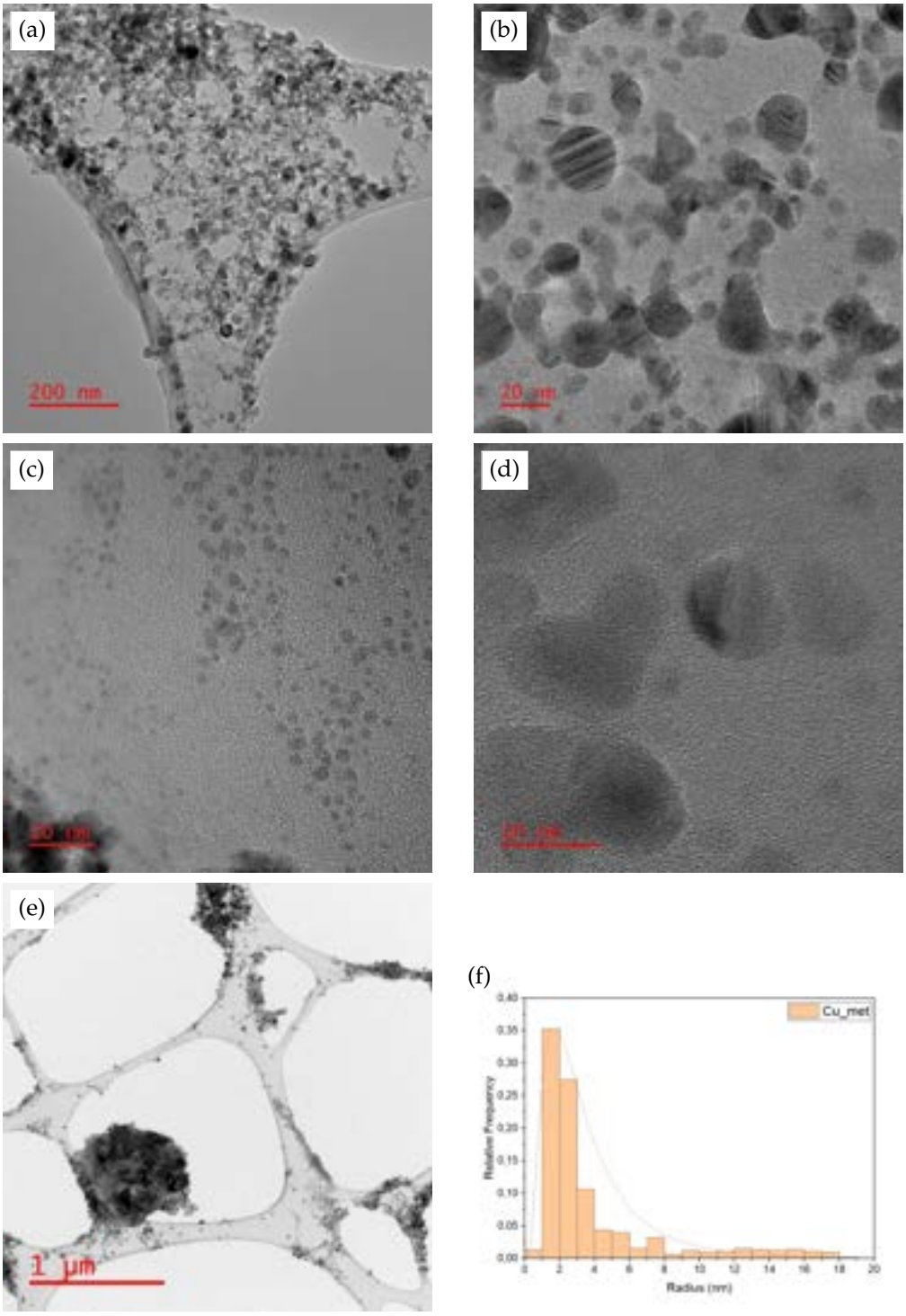

Figure 2.11: (a),(b),(c),(d),(e): *Cu_met* NPs on Carbon lacey grid at different magnifications. **(f)**: Statistic of 892 particles fitted with a lognormal distribution ($x_c = 2.1nm$, $w = 0.62$).

2.3.3.2 Copper in ethanol

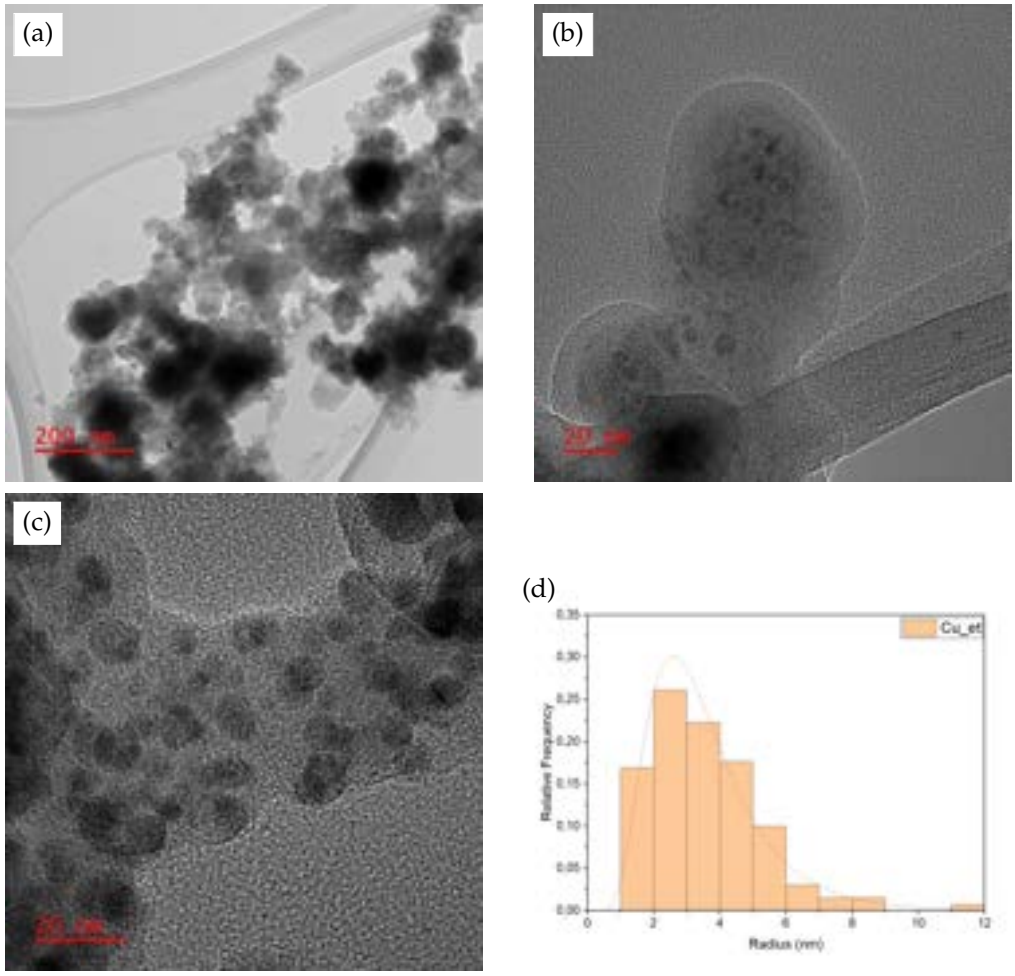

Figure 2.12: (a),(b),(c): *Cu_et* NPs on Carbon lacey grid at different magnifications. **(d)**: Statistic of 130 particles fitted with a lognormal distribution ($x_c = 3.3nm$, $w = 0.52$).

Figure 2.12 shows a collection of **Copper** NPs produced in **ethanol** at different magnifications. All the particles seem to be embedded in a unknown matrix that extends outer the grid. Most of the particles seem to be circular, but no specific analysis can be conducted due to the embedding in the unknown substance which did not allow to acquire higher

resolution images.

Size distribution analysis in Figure 2.12(d) was conducted by measuring one by one the particles that appear distinguishable. In total 130 particles were measured and their size distribution follows a lognormal distribution with a fitted curve that reports $x_c = 3.3nm$ and $w = 0.52$ with the most representative value $x_p = 2.5nm$, indicating a dimension much smaller then the one obtained with SEM analysis in Figure 2.9(d). This size is similar to the one obtained for *Cu_met* and in both case there is no presence of a shell around the particles.

2.3.3.3 High resolution TEM

To better understand the particle nature, high resolution images are taken of the **Copper** NPs produced in **methanol**. A first close inspection allows to identify crystal planes on small particles. Some of these particles (Figure 2.13) also present one or more twin defects, a clear sign of the strong non equilibrium process that happen during laser ablation.

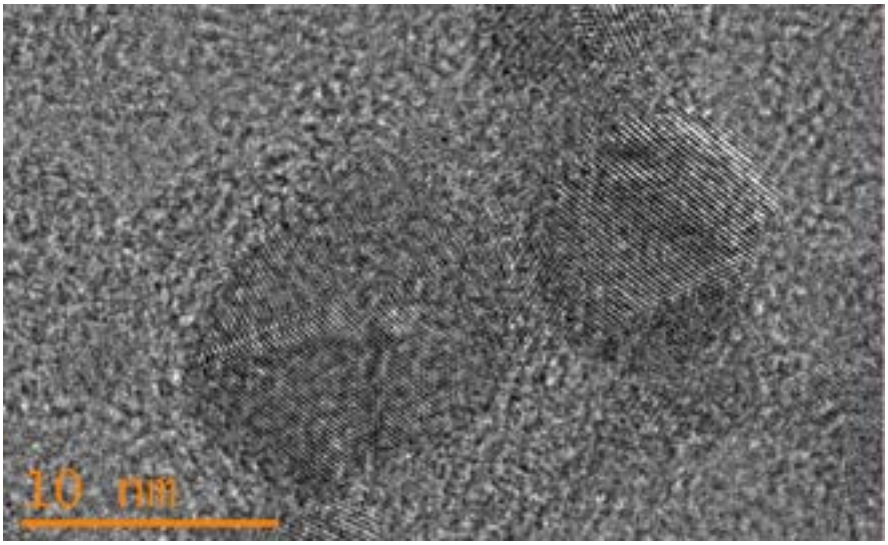

Figure 2.13: Two small particles with twin defects (*Cu_met*).

The distance between crystal planes are typical of each compounds and allows to identify the particle nature. With this high resolution TEM

is possible to measure the interplanar distance and in some cases even the single atoms are visible and distinguishable.

Analysis were conducted with `Gatan DM3` software [20]. To obtain the interplanar distance, a line profile was taken perpendicular to the visible atom lines. This line is expanded in form of rectangle to help eyes in alignment and integrate over the width to help cover the image noise. The line profile is reported in form of histogram and the distance between two peaks in the line profile represents the interplanar distance and the error corresponds to the bin size. The x axis is nm while the y axis report the integrate image intensity. Another approach is to perform a Fast Fourier Transform (FFT) on a square region where the atomic planes are clearly visible and measure the distance between the central spot and the other bright spots with an error that depends on the pixel size.

Figure 2.14(a) shows a large particle (compared to scale) in which the single atoms are visible and at least three crystallographic direction can be identified. The FFT (Figure 2.14(b)) is performed on the red square box and clearly shows six brilliant spot symmetric with respect to origin. Each couple of spots represent a crystallographic direction and the line that connects the spot to the center is perpendicular to the crystal plane due to the mathematical formulation of the FFT. These three crystallographic directions are marked with numbers in both Figures 2.14(a) and 2.14(b) and the relative line profiles are reported in Figures 2.14(1), 2.14(2) and 2.14(3). The direction (3) is very noisy both in line profile and FFT in fact presents a bit higher interplanar distance ($0.23 \pm 0.01nm$ line profile, $0.23 \pm 0.02nm$ FFT) than the others ($0.21 \pm 0.01nm$ line profile, $0.22 \pm 0.01nm$ FFT). Figure 2.14(b) also presents other less brilliant spots all around central hexagon. The ones aligned with the highest intensity spots are a second order effect of the FFT and results in a distance half the previously reported. The others refers to planes with a distance of $0.13 \pm 0.01nm$ but are very confused.

Figures 2.15(a) and 2.15(b) shows a very small particle in which the single atoms can be identified and its Fourier transform. Even if three crystallographic direction can be identified, only the most relevant will be considered (in this case the quasi vertical planes) to avoid high uncertanties.

Figures 2.15(c) and 2.15(d) shows a particle with a defect and its

Fourier transform. The right side presents atomic planes misaligned with the electron beam direction and appears unclear, but the left part shows bright atomic lines. The FFT indeed clearly shows only two bright symmetrical spots and also the second order spots.

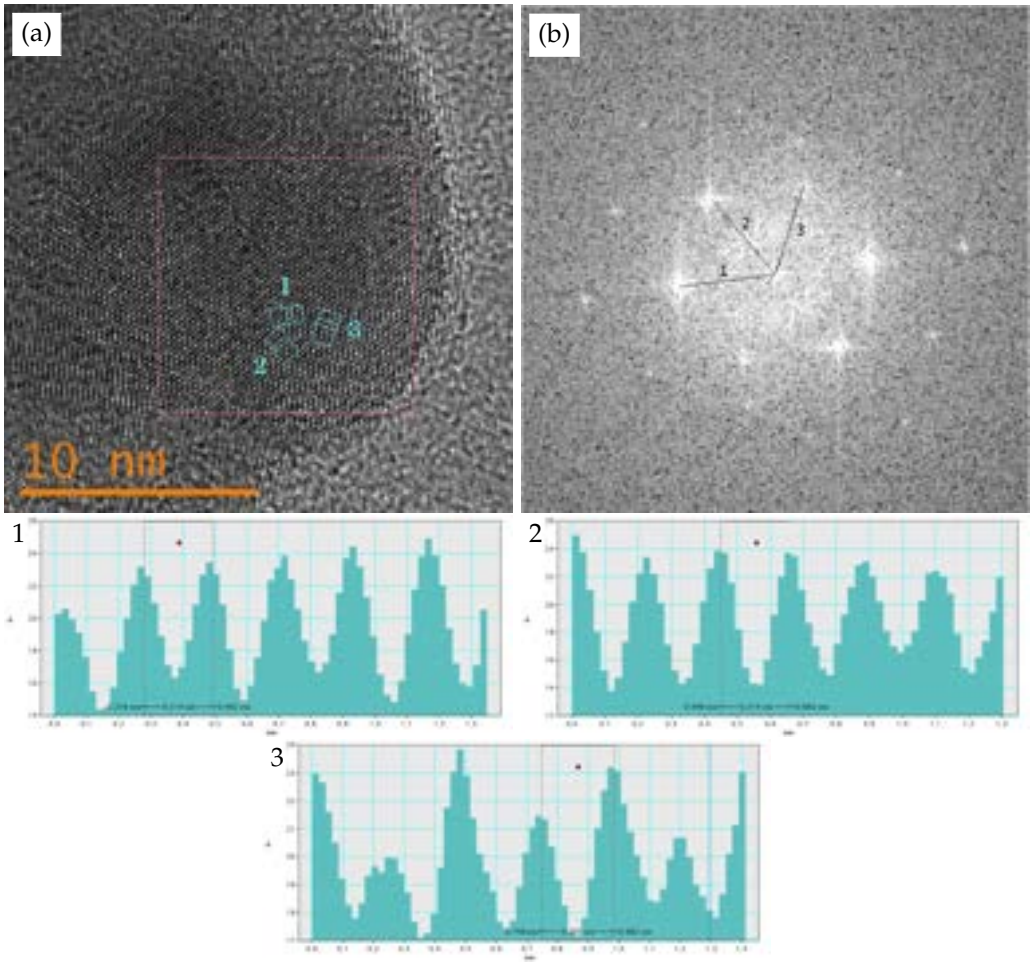

Figure 2.14: (a): High resolution TEM of a *Cu_met* NP and **(b)**: its FFT. **(1)**,**(2)** and **(3)**: the line profiles in the three marked crystallographic directions.

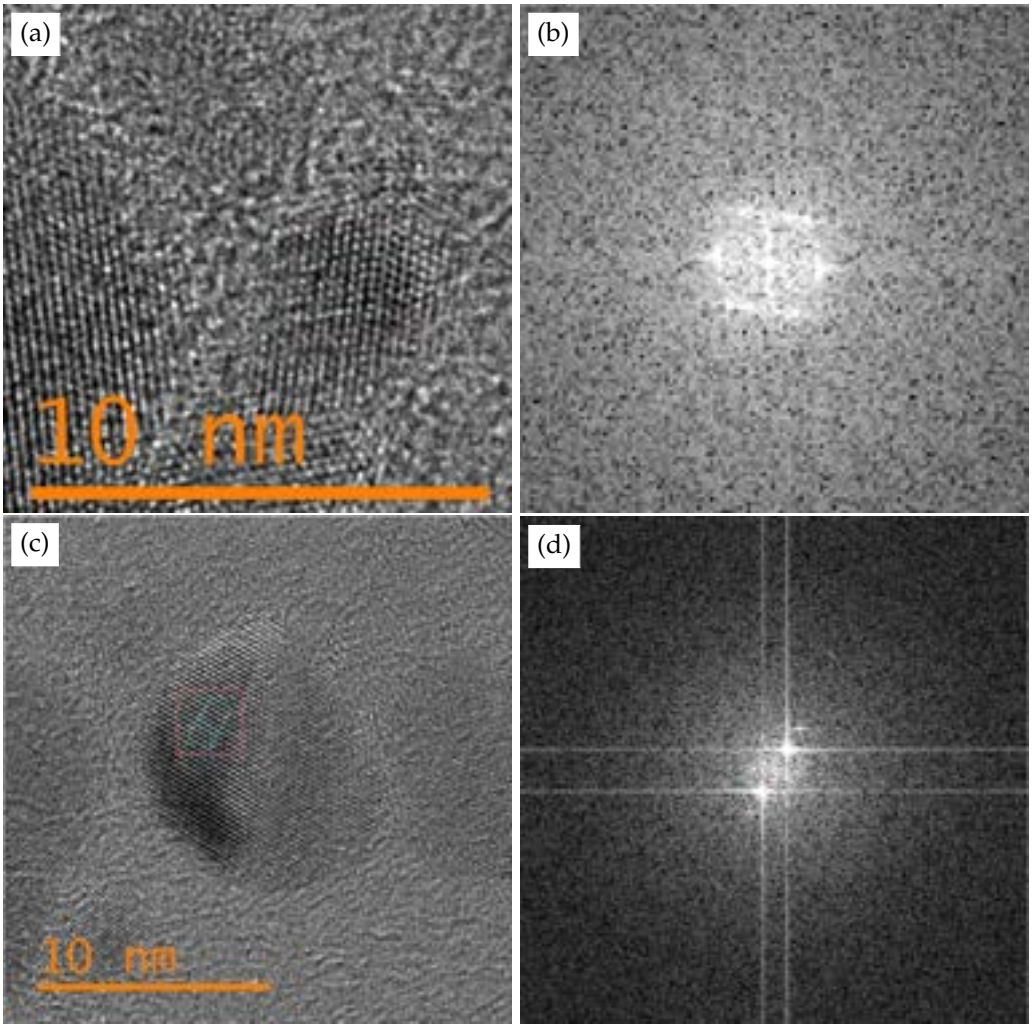

Figure 2.15: (a): A very small particle (*Cu_met*) with clearly visible atoms and **(b)**: its FFT. **(c)**: A particle (*Cu_met*) with strong visible atomic line and **(d)**: its FFT.

In general interplanar distance obtained trough FFT differs from the one obtained with line profile because of the image noise. Mean values of interplanar distance are 2.2 ± 0.2Å for line profile method and 2.1 ± 0.1Å for FFT method.

All the measured values are reported in the Figure 2.16. Horizontal dashed lines are the interplanar distance for Copper (blue) and *CuO*

(green) with the reported crystallographic direction evaluated with software `CaRIne Crystallography` [21]. Copper has a Face Centered Cubic lattice whose most suitable plane is $(1,1,1)$ with a spacing of 2.087Å. CuO instead has a Monoclinic lattice whose most suitable planes are $(1,1,1)$ with a spacing of 2.316Å and $(-1,1,1)$ with a spacing of 2.516Å. All the measured values lies between Cu and CuO and has a lot of variation for very small particles. The less brilliant spots reported in Figure 2.14(b) suggest a distance $(1.3 \pm 0.1$Å$)$ similar to $Cu(2,2,0)$ (1.278Å) or $CuO(2,2,0)$ (1.371Å) but the error is to high to strict identify the composition.

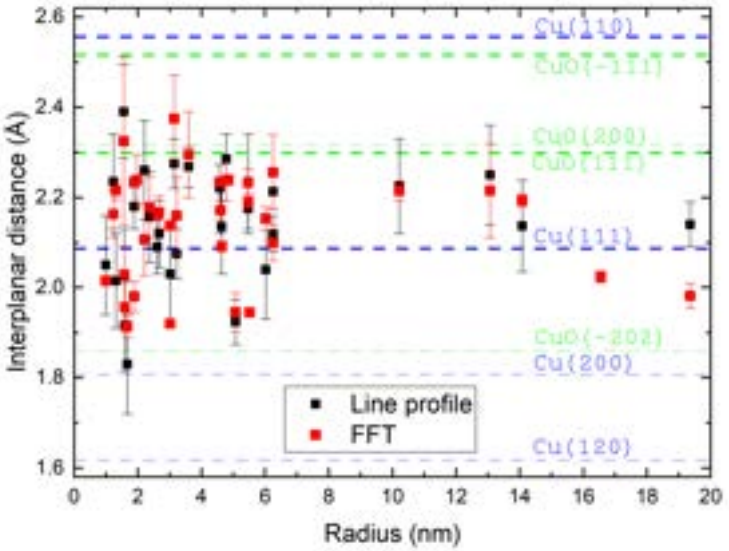

Figure 2.16: Plot of measured interplanar distances with error bars against particle radius of **Copper** NPs produced in **methanol**. Horizontal lines are the planes distances for some crystallographic direction obtained with [21].

Both line profiles and FFT were taken considering the nearest atomic lines or brlliant spots, so planes given by second order Miller index can be excluded. All the data reported in Figure 2.16 lies around $Cu(1,1,1)$ suggesting that the particles are mostly metallic, but the high variability of the interplanar distance of the small particles cannot exclude that few of them are CuO.

High Resolution TEM for **Copper** NPs produced in **ethanol** presents the problem of the unknown substance and allows to see only a very small amount of particles with distinguishable crystal planes. Figure 2.17(a) shows some particles not well defined with visible planes. Figure 2.17(b) reports the measured distances with the errors that are bigger than the previous. This values suggest metallic Copper.

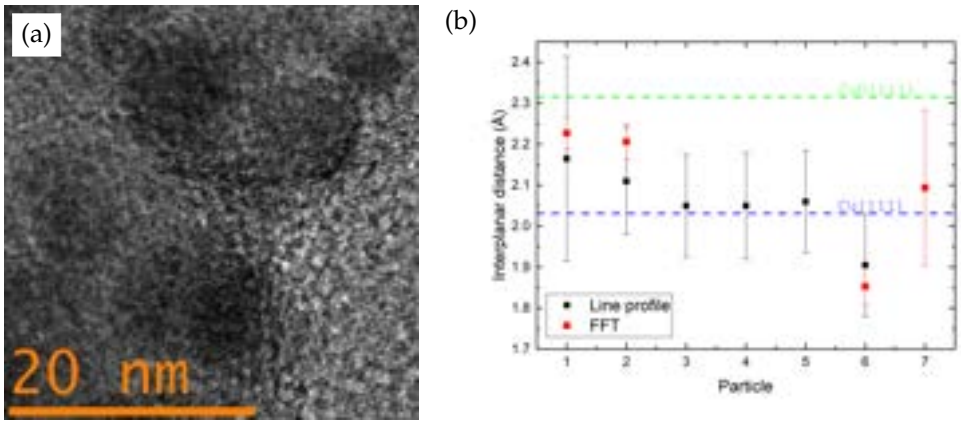

Figure 2.17: (a): An example of **Copper** NPs produced in **ethanol** with visible crystal planes. **(b)**: Plot of measured interplanar distances with error bars per particle. Horizontal lines are the planes distances for for $Cu(1,1,1)$ and $CuO(1,1,1)$ obtained with [21].

2.3.3.4 Electron Diffraction

Another result obtained by the TEM is the electron diffraction. The diffraction pattern of the **Copper** NPs produced in **Methanol** is given in Figure 2.18. This pattern presents a lot of circles with some brilliant spots. The circles are originated from all the small NPs with different orientations, while the spots come from some bigger monocrystalline particles. A circular patter was simulated using `CrysTBox` software [22] for Cu, CuO and Cu_2O. Only the metallic Copper circles match the data and the brightest one correspond to $\{1,1,1\}$ plane, the one indicated in figure 2.16 around which all the data is located.

The analysis was not conducted on Cu_et NPs because of the presence of the unknown substance

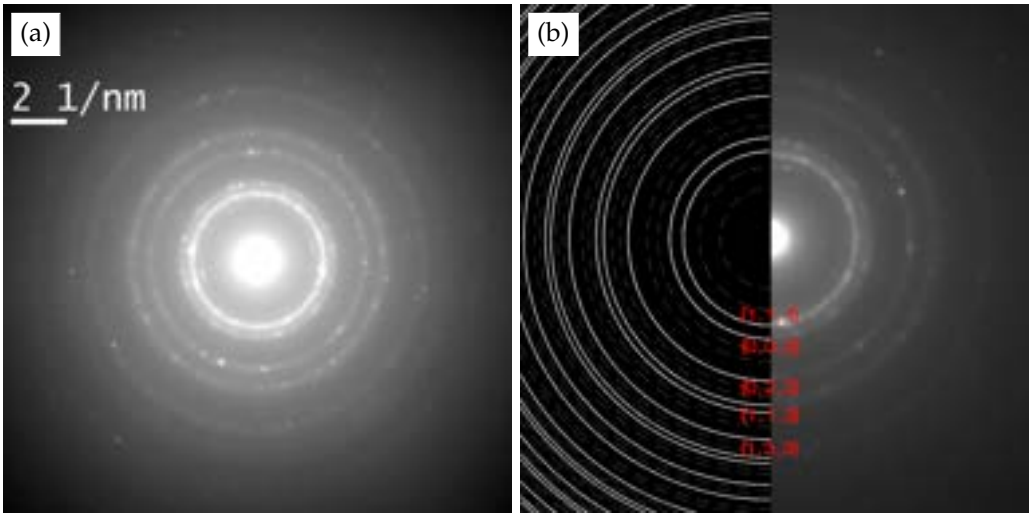

Figure 2.18: (a): Diffraction pattern of *Cu_met* NPs with adjusted contrast to distinguish up to five circles. **(b)**: Image produced by [22] with half *Cu* simulated rings and half experimental data with marked crystal plane.

2.3.4 X-Ray Diffraction

Another technique that can point out the NPs nature is the X-Ray Diffraction (XRD) because can analyze their composition (see appendix F). Samples were prepared by drop casting a large amount of solution (less than a *ml*) on a quartz substrate (`Corning Glass`). A large quantity of material is necessary because XRD is a bulk technique.

Figure 2.19 presents the XRD diffractogram of **Copper** NPs produced in **methanol**. The vertical lines are the tabulated peaks positions for metallic Cu, CuO and Cu_2O with relative intensities [23, 24, 25]. At low angles there is a descending behaviour indicating the amorphous substrate. First sharp peak appears at $\sim 43^\circ$, another one at $\sim 50^\circ$ and a smaller one at $\sim 74^\circ$ indicating respectively $Cu(1,1,1)$, $Cu(2,0,0)$ and $Cu(2,2,0)$ planes. The overall diffractogram is noisy for except these peaks and does not evidence trace of oxides.

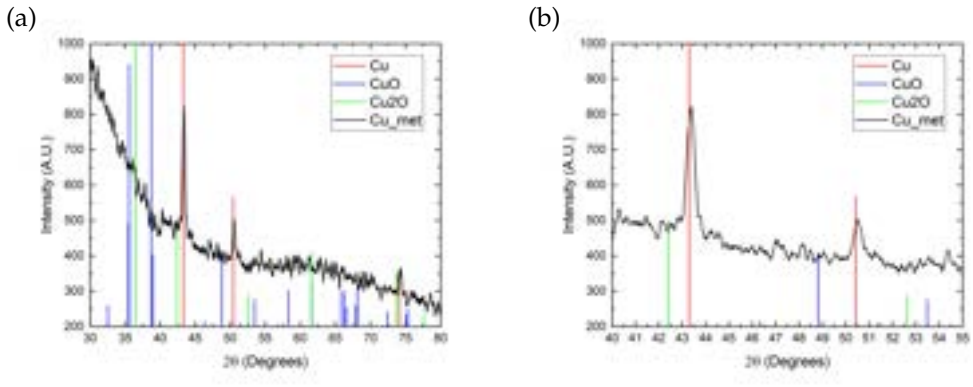

Figure 2.19: (a): *Cu_met* XRD spectrum (black), Vertical line are *Cu* (red), *CuO* (blue) and Cu_2O (green) peaks with high corresponding to relative reported intensities [23, 24, 25]. **(b)**: Zoom on the main peaks region ($2\theta = 40 - 55°$).

Figure 2.20 presents the XRD diffractogram of **Copper** NPs produced in **ethanol**. Also in this case the behaviour at low angles indicates the amorphous substrate and the observable peaks correspond to metallic *Cu* peaks with no evidence of oxides. An exception can be the peak at $\sim 36°$ that can indicate a small presence of Cu_2O, but can also be noise because the main peak of Cu_2O at $\sim 38°$ is not present.

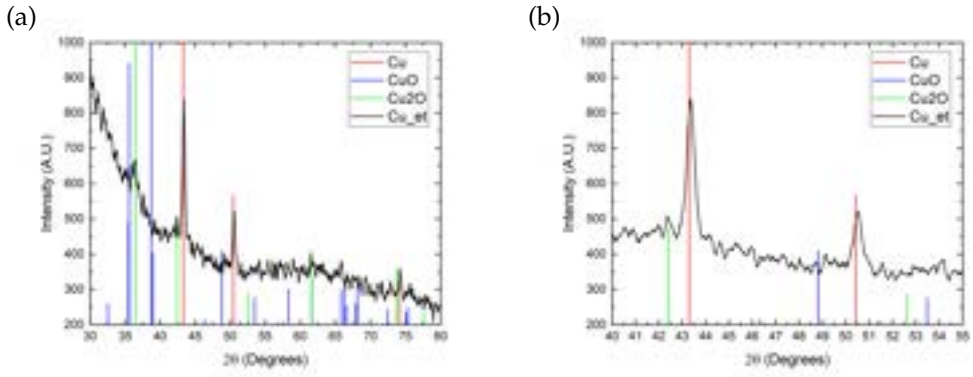

Figure 2.20: (a): *Cu_et* XRD spectrum (black), Vertical line are *Cu* (red), *CuO* (blue) and Cu_2O (green) peaks with high corresponding to relative reported intensities [23, 24, 25]. **(b)**: Zoom on the main peaks region ($2\theta = 40 - 55°$).

Figure 2.21 presents the XRD diffractogram of **Nickel** NPs produced

in **methanol**. The vertical lines are the tabulated peaks positions for metallic Ni, NiO with relative intensities [26, 27]. First sharp peak appears at $\sim 44^\circ$, another one at $\sim 51^\circ$ and a smaller one at $\sim 76^\circ$ indicating respectively $Ni(1,1,1)$, $Ni(2,0,0)$ and $Ni(2,2,0)$ planes. No trace of oxides are present, but all the peaks are shifted at lower angles, maybe due to a calibration issue.

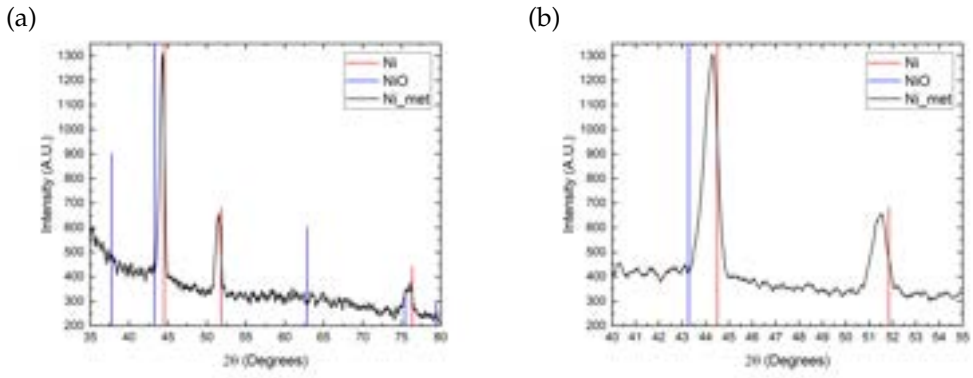

Figure 2.21: (a): Cu_et XRD spectrum (black), Vertical line are Ni (red) and NiO (blue) peaks with high corresponding to relative reported intensities. [26, 27] **(b)**: Zoom on the main peaks region ($2\theta = 40 - 55^\circ$).

2.3.5 X-Ray Photoelectron Spectroscopy

A technique that can point out the chemical composition of the NPs surface is the X-Ray Photoelectron Spectroscopy (XPS) (see appendix G). Samples were prepared by drop casting some μl of solution on Silicon and letting it dry on a hot plate. The study of the spectrum is conducted by checking the tabulate peak on the XPS handbook [28].

2.3.5.1 Copper in methanol

Figure 2.22 presents the XPS spectra of **Copper** NPs produced in **methanol** with two high peaks corresponding to Oxygen ($\sim 531eV$) and Carbon ($\sim 285eV$). At low binding energy there are two peaks corresponding to the Silicon substrate ($\sim 151eV$ and $\sim 99eV$). At high energy, but very low intensities there are the typical peaks of Copper ($\sim 933eV$ and $\sim 953eV$)

and an Auger peak of Oxygen ($\sim 978eV$). The presence of Silicon peak indicates that not all the substrate is covered by particles. The low intensity of Copper peaks suggest that a very few amount of NPs is present of the substrate or these particles are somehow screened. This last hypothesis is supported by the strong peaks of Carbon and Oxygen coming from the solvent. The Oxygen presents its peak at $532.6eV$, this chemical shift is come from SiO_2 indicating an oxidation of the substrate. The Carbon presents its peak at $285.7eV$, this chemical shift is come from the alcohols. The Copper presents its peak at around $933.5eV$ but there is also a shoulder that suggest another peak.

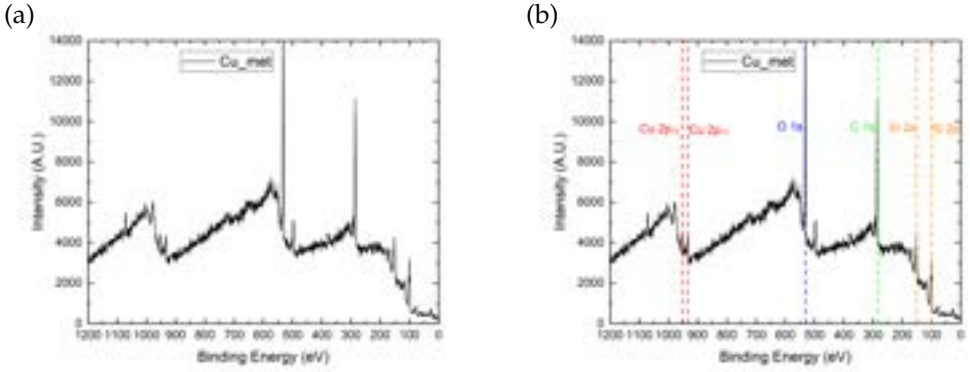

Figure 2.22: (a): *Cu_met* XPS survey spectra. **(b)**: Same spectra with marked Copper (red), Oxygen (blue), Carbon (green) and Silicon (orange) peaks [28].

Figure 2.23(c) shows the high resolution spectrum on the energy scale of the Copper peak. Figures 2.23(a) and 2.23(b) shows the literature spectrum [28] respectively for metallic Cu and CuO. The secondary large and lower peak at $\sim 945eV$ is present only in the oxide but the one reported in literature is much more intense than the one measured. The main peak is at $\sim 933eV$ that lies between metallic Copper ($933eV$) and CuO ($933.8eV$). This suggests an intermediate nature of metallic Cu and CuO, but prevalently Cu. Figure 2.24 shows that the main peak is the convolution of two peaks: one at $933.4eV$ that lies between metallic Copper and CuO and another one at $935.5eV$ that may come from some compounds involving Copper and Carbon.

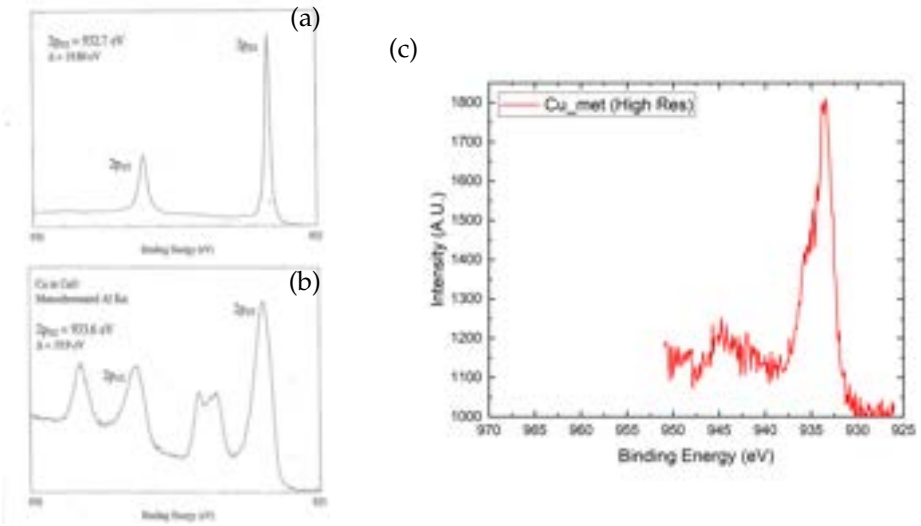

Figure 2.23: High resolution XPS spectra of the Copper peak in **(a)**: metallic Copper [28], **(b)**: *CuO* [28] and **(c)**: *Cu_met* NPs. The plots are deliberately in the same x-axis range.

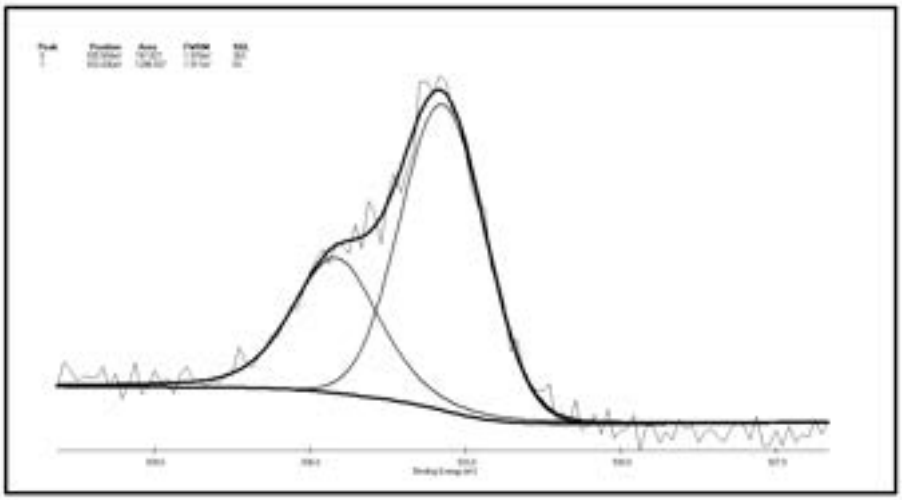

Figure 2.24: Deconvolution of Copper peak using [29]. There is a main peak at $933.4eV$ and another one at $935.5eV$.

2.3.5.2 Copper in ethanol

Figure 2.25 presents the XPS spectra of **Copper** NPs produced in **ethanol** with the two high peaks of Oxygen and Carbon. The peaks of Copper are absent and the Silicon ones are really low in intensity. This suggest that the unknown substance seen in Figure 2.12 completely screen the Copper signal. Also in this case the Oxygen chemical shift (533.6eV) suggests SiO_2 and the Carbon chemical shift (285.6eV) suggests alcohols.

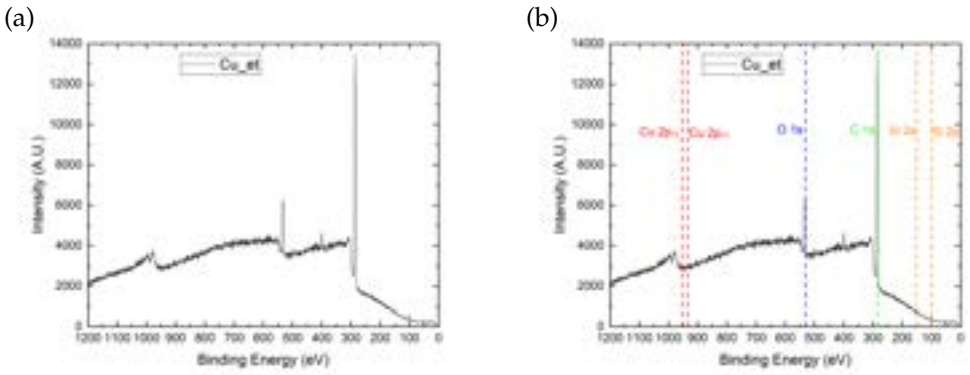

Figure 2.25: (a): *Cu_et* XPS survey spectra. **(b)**: Same spectra with marked Copper (red), Oxygen (blue), Carbon (green) and Silicon (orange) peaks [28].

2.3.5.3 Nickel in methanol

Figure 2.26 presents the XPS spectra of **Nickel** NPs produced in **methanol** with the two high peaks of Oxygen and Carbon. Also in this case the Oxygen chemical shift (532.8eV) suggest SiO_2 and the Carbon chemical shift (286eV) suggest alcohols. The Nickel presents its peak at 856.3eV suggesting $Ni(acac)_2$ (Nickel acetylacetonate) or some other Carbon compounds at least on the NPs surface.

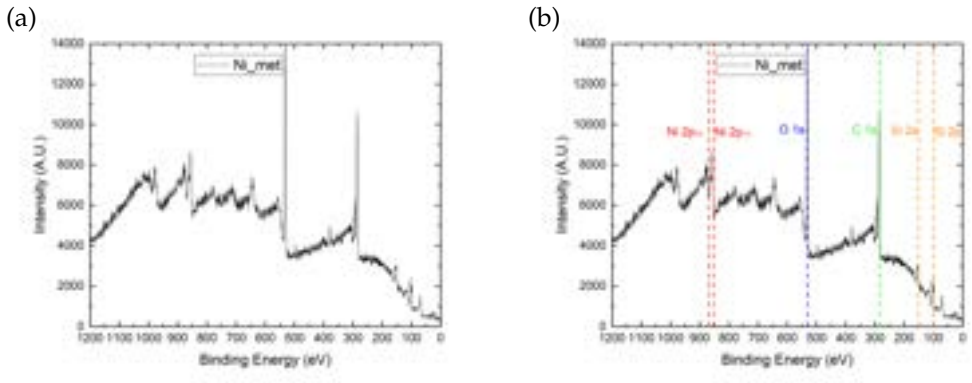

Figure 2.26: (a): *Ni_met* XPS survey spectra. **(b)**: Same spectra with marked Nickel (red), Oxygen (blue), Carbon (green) and Silicon (orange) peaks [28].

2.3.6 Energy Dispersive X-Ray

Information about the composition of the NPs are provided by Energy Dispersive X-Ray (EDX) using the X-Rays emitted from the previously used samples inside the TEM (see appendix C.3) working in Scanning Transmission Electron Microscopy (STEM) mode. The analysis was conducted only on *Cu_met* NPs because of the substance that cover all the particles in *Cu_et* sample will prevent valuable results. Analysis were conducted using `Gatan DM3` software [20].

Figure 2.27 shows two STEM images and the EDX analysis with some color map. Figure 2.27(a) presents three NPs, Figure 2.27(b) a bigger one. The Copper (green) is present only inside the NPs while Carbon (blue) and Oxygen (red) are present uniformly outside the NPs. The particle marked as "1" in Figure 2.27(a) is low contrasted in the STEM image, in fact results covered of Carbon and Oxygen in the color maps. Particles marked as "2" and "3" exhibit a higher contrast and presents a hole especially in the Carbon map.

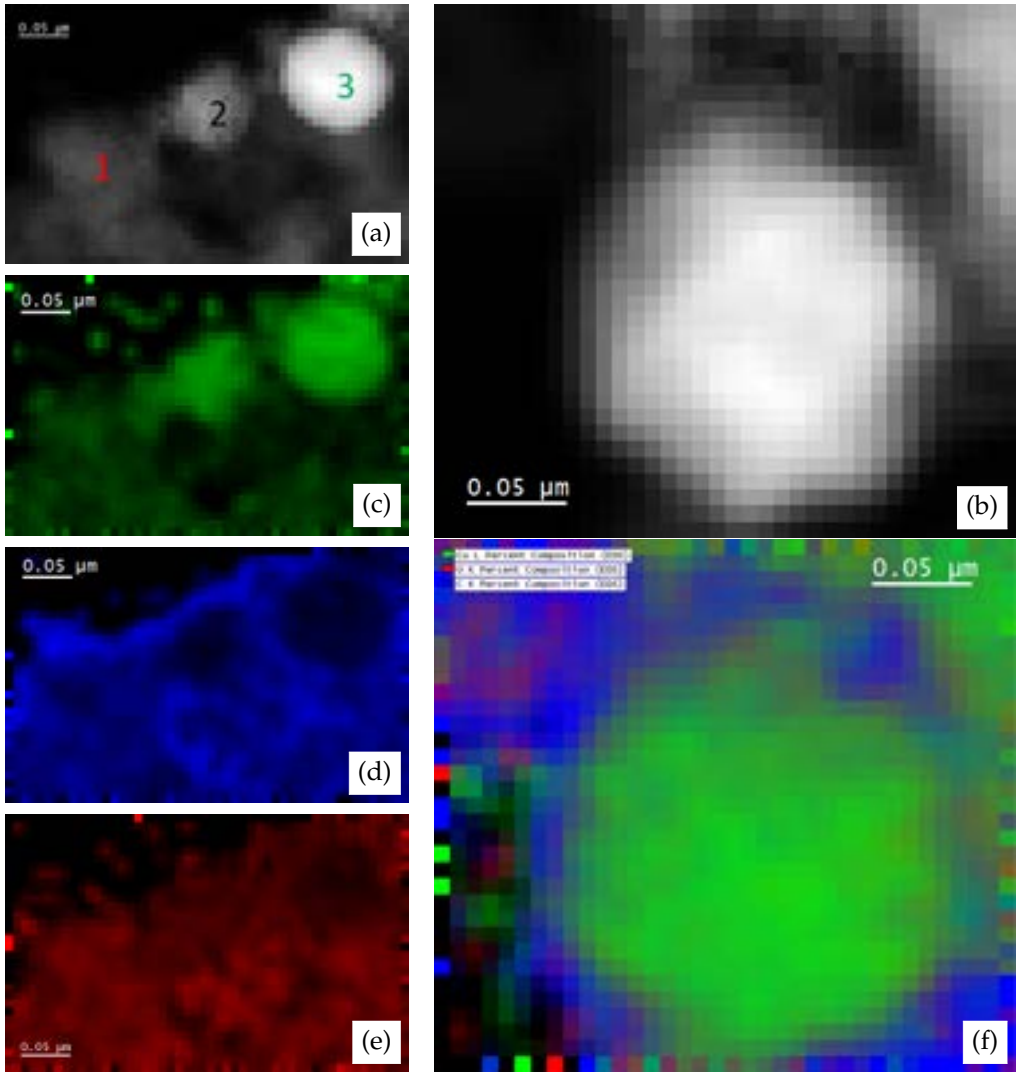

Figure 2.27: (a),(b): STEM images of **Copper** NPs produced in **Methanol** on which EDX analysis are performed. **(c),(d),(e)**: Color map indicating the presence of Copper (green), Carbon (blue) and Oxygen (red) of image (a). **(f)**: Color map indicating the presence of Copper, Carbon and Oxygen of image (b).

Figure 2.28(a) presents the EDX spectrum of the three particles marked in Figure 2.27(a). Particles "2" and "3" presents a most relevant Copper peak with respect to other elements. Oxygen and Copper peaks have slightly the same height in the same NPs. Some impurity are present

like *Mg* and *Si*. Figure 2.28(b) presents a line profile with the percentage of presence of Copper (green), Carbon (blue) and Oxygen (red) across the particle in Figure 2.27(b). This figure in particular and more in general this analysis indicates that the particles are made of metallic Copper, presents no shell and are embedded in a medium that contains both Carbon and Oxygen.

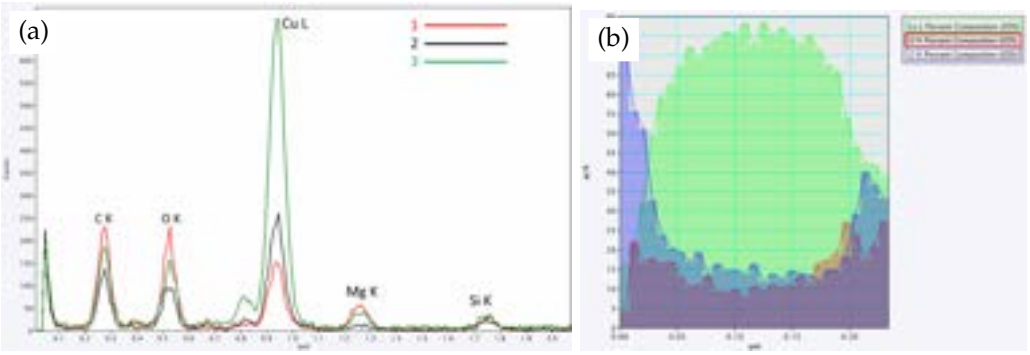

Figure 2.28: (a): EDX spectrum of the particles marked in Figure 2.27(a) ("1" red, "2" black and "3" green).**(b)**: Line profile with the percentage of presence of Copper (green), Carbon (blue) and Oxygen (red) across the particle of Figure 2.27(b).

2.4 Understanding the data

Previous data seems to suggest that PLAL produced metallic NPs, but some point should be clarified:

- The nature of the unknown substance around the Copper NPs produced in ethanol (Section 2.3.3) and the reason behind the absence of the Copper peaks in XPS (Section 2.3.5).
- The meaning of the UV-Vis-NIR spectra (Section 2.3.1).

In this Section some hypothesis and simulation are conducted to clarify the previous points and better understand the data.

2.4.1 Polymer shell around particles

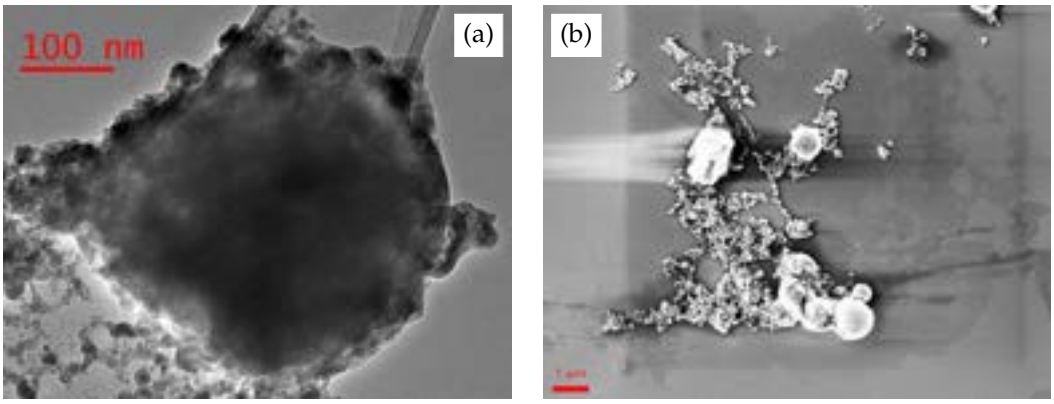

Figure 2.29: (a): TEM image of a big particle made up of many small NPs clusters in *Cu_met*. **(b)**: SEM image with straight horizontal lines due to charge accumulation in *Cu_met*.

The nature of the unknown substance that encloses the particles of Copper synthesized in ethanol seen in Figure 2.12 can be attributed to a polymer that embeds the particles formed from the solvent during the laser ablation process. The idea behind the consideration of a polymer around the particles come from extreme process that occurs during the Pulsed Laser Ablation in Liquid. In fact in proximity of the laser spot, there is the formation of a cavitation bubble of vaporized solvent at high temperature that can heavily modify the chemical composition of the solvent. In support of this hypothesis there is the fact that all the XRD measures presented in Section 2.3.4 were performed after three month of deposition: the NPs results to be metallic, but the Copper oxidizes rapidly in air [30]. So the preservation of metallic nature of the particles over a long time indicates the presence of a protective coating. Also the strong difference of size distribution between SEM (Section 2.3.2) and TEM (Section 2.3.3) can be explained with the polymer. The few big particles visible with TEM analysis results to be the agglomeration of smaller particles and the polymer is the glue that keeps them together as in Figure 2.29(a). Also the presence of polymer should affect the electric conductivity due to its insulating properties. This idea is supported by some artifacts seen

in Figure 2.29(b) around the bigger particles of the cluster indicating a charge accumulation due to non conductivity. Also EDX data (Section 2.3.6) support the polymer hypothesis: Carbon and Oxygen are uniform between the particles and sometimes cover them.

2.4.1.1 Pulsed Laser Polymerization

An entire technique developed by chemists uses the laser pulses to start the polymerization from gaseous organic compounds (Pulsed Laser Polymerization) [31, 32], but there are no recent studies that involves methanol or ethanol polymerization. The idea behind this technique is that UV radiation (or at least electrons) can break some chemical bonding by resonating with them and so creating polymeric chains. The laser used for this works is typically working in the UV region and involve vaporized precursors, but a recent review [33] shows how this process happen also in traditional PLAL. In fact the cavitation bubble contain vaporized solvent and both the heat and the eventual hot metal can act like catalyst to form this polymers. In this case both ethanol and methanol are reported to form HC_nCH_3 or C_nH_2 compounds with a laser wavelength of $1064nm$ using a graphite target, but no further studies on the nature of the polymer was conducted.

Another technique is the plasma polymerization, that involves the plasma generated from a RF electric field to induce chemical reaction in the precursor vaporized in the chamber. In particular ethanol is reported to form a polymer film [34, 35]. The process in this case is activated by the plasma and involves the ethanol vapour, the idea is that in the cavitation bubbles this two elements (plasma and vapour) are present as well and so the mechanism of polymerization could be the same. Surely more chemical knowledge is needed to fully comprehend this process.

2.4.1.2 Polymer XPS peak

Polymer film reported by [34, 35] is characterized with XPS and the Carbon peak is surprisingly similar to the one observed in Section 2.3.5 for all the samples.

By comparing the spectrum reported in Figure 2.30, Copper NPs pro-

duced in ethanol presents slightly the same behaviour of the reported one, so there could be polymer coating. This coating seems to be big enough to prevent photoelectrons emitted from Copper to reach the detector and completely screen the NP signal.

Copper and Nickel NPs produced in methanol present a sharper peak shifted at slightly higher energies that also indicate a polymer.

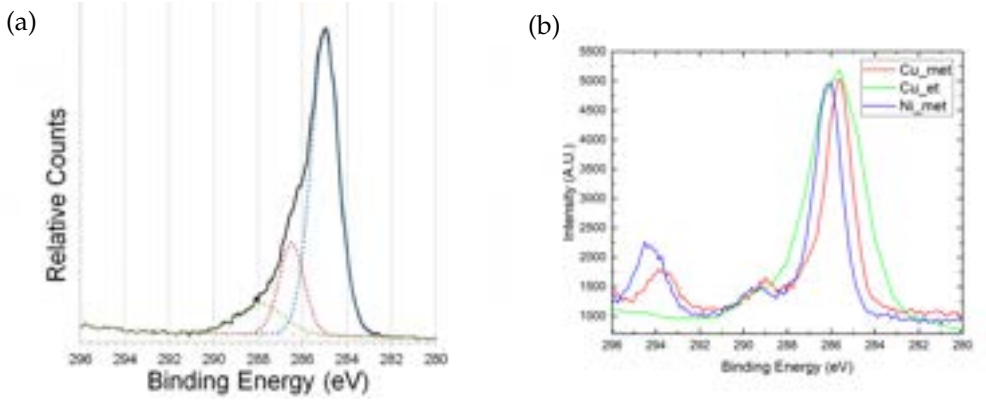

Figure 2.30: (a): Carbon XPS peak from [34] where are presented also $C-C$ bonds (blue dashed line), $C-O$ bonds (red dashed line) and $C=O$ bonds (green dashed line). **(b)**: Carbon XPS peak for *Cu_met* (red line), *Cu_et* (green line) and *Ni_met* (blue line).

2.4.2 Optical simulations

In order to understand the relation between absorption spectrum and particle size and distribution, some simulations were conducted. This simulation will provide the extinction cross section σ_{ext}. Extinction is given by the sum of two effects: the absorption and the scattering. Whenever the light encounter a small NP, it can be absorbed or scattered by the NP surface. The total cross section is related to the absorption via the Beer-Lambert law (Equation B.5).

The relation within spherical particles and light absorption is well described by the Mie theory [11, 36, 37]. This theory starts from the Drude models for electrons.

2.4.2.1 Drude model

Some electrons in metal can behave like free electrons because metals have no bandgap between conduction and valence band. Whenever an electromagnetic wave affects a metal NP, free electrons start responding as follow:

$$m_e \frac{\partial^2 \mathbf{r}}{\partial t^2} + m_e \Gamma \frac{\partial \mathbf{r}}{\partial t} = e\mathbf{E_0} e^{-i\omega t} \tag{2.3}$$

where m_e is the electron effective mass, Γ is a damping constant, e is the electron charge, $\mathbf{E_0}$ is the amplitude of the incident electric field and ω is the incident field frequency. From the position $\mathbf{r}$, the dipole moment is given by $\mathbf{p} = e\mathbf{r}$ and the polarization by $\mathbf{P} = n\mathbf{p}$ where n is the numeric density of electrons. Polarization and incident electric field are related by the polarizability α, $\mathbf{P} = n\alpha\mathbf{E}$. Polarizability can be expressed in relation to the dielectric function ϵ:

$$\epsilon - 1 = \frac{1}{\epsilon_0} n\alpha \tag{2.4}$$

From the solutions of (2.3) the dielectric function is:

$$\epsilon(\omega) = 1 - \frac{\omega_p^2}{\omega^2 + i\omega\Gamma} \tag{2.5}$$

where the relaxation constant $\Gamma = v_F/l$ is related to Fermi velocity v_F and electron mean free path l and $\omega_p = \sqrt{ne^2/\epsilon_0 m_e}$ is the plasma frequency. This relation can be extended to all band transitions adding a sum:

$$\epsilon(\omega) = 1 - \frac{\omega_p^2}{\omega^2 + i\omega\Gamma} + \sum_j \frac{\omega_{pj}^2}{\omega_j^2 - \omega^2 - i\omega\gamma_j} \tag{2.6}$$

where ω_j depends on the energy difference $\Delta E_j = \hbar\omega_j$ between two bands or levels with its own plasma frequency ω_{pj} and damping constant γ_j that depends on the the inverse of the level lifetime.

2.4.2.2 Quasistatic response of a small metal sphere

When the particle radius is much smaller than wavelength $R \ll \lambda$, the NP act like a dipole and responds to the electric field in a quasi static way.

Whenever the sphere is placed inside a medium, the ratio between internal and external field is obtained by applying the boundary conditions to Maxwell Equations:

$$\frac{E_i}{E_0} = \frac{3\epsilon_m}{\epsilon + 2\epsilon_m} \tag{2.7}$$

where ϵ is the metal dielectric function and ϵ_m is the medium dielectric function. The polarizability can be redefined as:

$$\alpha = 4\pi\epsilon_0 R^3 \frac{\epsilon - \epsilon_m}{\epsilon + 2\epsilon_m} \tag{2.8}$$

Cross section depends on the polarizability α and the wave number $k = 2\pi/\lambda$ as follow:

$$\sigma_{sca} = \frac{k^4}{6\pi} Abs(\alpha)^2 \tag{2.9}$$

$$\sigma_{abs} = kIm(\alpha) \tag{2.10}$$

$$\sigma_{ext} = \sigma_{abs} + \sigma_{sca} \tag{2.11}$$

the subscripts indicate respectively scattering, absorption and extinction.

2.4.2.3 Mie theory

A relevant parameter is the size parameter defined as:

$$x = |k|R \tag{2.12}$$

When $x \gg 1$ geometric optic is valid, when $x \ll 1$ the quasi static approach is valid, elsewhere Mie theory must be used.

In 1908 Mie applied Maxwells Equations with appropriate boundary conditions in spherical coordinates using multipole expansions of the incoming electric and magnetic fields to solve the scattering problem. Starting point is the Helmoltz Equation:

$$(\nabla^2 + k^2)U(\mathbf{r}) = 0 \tag{2.13}$$

Solutions can be express in spherical coordinates $U(\mathbf{r}) = R(r)\Theta(\theta)\Phi(\phi)$. The overall solution express cross section in the form of a sum of the contributions of different multipoles of order L:

$$\sigma_{ext} = \frac{2\pi}{|k|^2} \sum_{L=1}^{\infty} (2L+1) Re(a_L + b_L) \tag{2.14}$$

$$\sigma_{sca} = \frac{2\pi}{|k|^2} \sum_{L=1}^{\infty} (2L+1) \left(|a_L|^2 + |b_L|^2 \right) \tag{2.15}$$

$$\sigma_{abs} = \sigma_{ext} - \sigma_{sca} \tag{2.16}$$

where a_L and b_L are functions of size parameter and refractive index (ratio between the refractive index of the particle and the medium $m = n/n_m$) an the order L. These functions takes L from the Riccati-Bessel function ψ_L and Riccati-Hankel function ξ_L:

$$\begin{aligned} a_L &= \frac{m\psi_L(mx)\psi'_L(x) - \psi'_L(mx)\psi_L(x)}{m\psi_L(mx)\xi'_L(x) - \psi'_L(mx)\xi_L(x)} \\ b_L &= \frac{\psi_L(mx)\psi'_L(x) - m\psi'_L(mx)\psi_L(x)}{\psi_L(mx)\xi'_L(x) - m\psi'_L(mx)\xi_L(x)} \end{aligned} \tag{2.17}$$

In computations the sum can be truncated at $L = 6$ because high order multipoles gives negligible contributes.

Another Mie hypothesis states that dielectric function should be size dependent. In particular in the free electron part in the Equation 2.6 the relaxation constant Γ should be reconsidered. An interpretation of this hypothesis is that if free electrons mean free path is bigger than the NP size they can scatter on particle surface [38]. New Γ will depends on the old Γ_{bulk}, on the Fermi velocity v_F and on an effective mean free path l_{eff}:

$$\Gamma = \Gamma_{bulk} + \frac{v_F}{l_{eff}} \tag{2.18}$$

Effective mean free path l_{eff} depends on NP radius, but no specific relation is present in literature. Some works report a polynomial behaviour [38, 39] that fit well to the experimental data.

2.4.2.4 Core-Shell particle

Cross sections can also be evaluated for a core-shell spherical NP.

In the quasistatic response, the shell presence induce a modification of the polarizability α that depends on the shell dielectric function ϵ_s and the thickness d:

$$\alpha = \frac{(\epsilon_s - \epsilon_m)(\epsilon + 2\epsilon_s) + \left(\frac{R}{R+d}\right)^3 (\epsilon - \epsilon_s)(\epsilon_m + 2\epsilon_s)}{(\epsilon_s + 2\epsilon_m)(\epsilon + 2\epsilon_s) + \left(\frac{R}{R+d}\right)^3 (\epsilon - \epsilon_s)(2\epsilon_s - \epsilon_m)} \frac{4\pi}{3} (R+d)^3 \tag{2.19}$$

In this case R is the core radius and not the whole radius. Cross section are evaluated from α as before (Equations 2.10, 2.9 and 2.11).

In the case of Mie scattering, relations between core (no subscript), shell (subscript $_s$) and medium (subscript $_m$) are involved:

$$m_1 = \frac{n}{n_m} \qquad m_2 = \frac{n_s}{n_m} \qquad x = kR \qquad y = k(R+d)$$

$$A_L = \frac{m_2\psi_L(m_2x)\psi'_L(m_1x) - m_1\psi'_L(m_2x)\psi_L(m_1x)}{m_2\chi_L(m_2x)\psi'_L(m_1x) - m_1\chi'_L(m_2x)\psi_L(m_1x)}$$

$$B_L = \frac{m_2\psi_L(m_2x)\psi'_L(m_1x) - m_1\psi'_L(m_2x)\psi_L(m_1x)}{m_2\chi_L(m_2x)\psi'_L(m_1x) - m_1\psi'_L(m_2x)\chi_L(m_1x)}$$

$$a_L = \frac{\psi_L(y)(\psi'_L(m_2y) - A_L\chi'_L(m_2y)) - m_2\psi'_L(y)(\psi_L(m_2y) - A_L\chi_L(m_2y))}{\xi_L(y)(\psi'_L(m_2y) - A_L\chi'_L(m_2y)) - m_2\xi'_L(y)(\psi_L(m_2y) - A_L\chi_L(m_2y))}$$

$$b_L = \frac{m_2\psi_L(y)(\psi'_L(m_2y) - B_L\chi'_L(m_2y)) - \psi'_L(y)(\psi_L(m_2y) - B_L\chi_L(m_2y))}{m_2\xi_L(y)(\psi'_L(m_2y) - B_L\chi'_L(m_2y)) - \xi'_L(y)(\psi_L(m_2y) - B_L\chi_L(m_2y))} \tag{2.20}$$

Here there are Riccati-Bessel function ψ_L and Riccati-Hankel function ξ_L and χ_L. Cross section are evaluated from the functions a_L and b_L as before (Equations 2.14, 2.15 and 2.16).

2.4.2.5 The refractive index problem

To compute Mie cross section some solution are available and easy to use. An online tool [40], a free software [41], a Matlab script [42] and also a Mathematica script [39] can be found online with relative documentation. For the simulation in this work, the Mathematica script [39] was used as inspiration, but heavy changes and implementation have been performed to understand the meaning of the absorption spectrum.

In any case, the starting point is the dielectric function or the refractive index: $n = \sqrt{\epsilon\mu}$ but the magnetic permeability is considered negligible for every material in this energy range: $\mu \sim 1$. Refractive index can be found tabulated in an online database [43] or in a handbook [44]. For the case of Copper, a lot of refractive indexes are reported (Figure 2.31). They maintain likely the same trend, but are very different. This happen for every metal because they have been studied with different approaches,

so the problem is figuring out which one to use. Instead for the oxides data are more difficult to find and the few reported are defined only in a narrow range. However in the handbook [44] are present both CuO and Cu_2O in the desired range. The search was fruitless for NiO. Methanol and ethanol can be found in the online database [43].

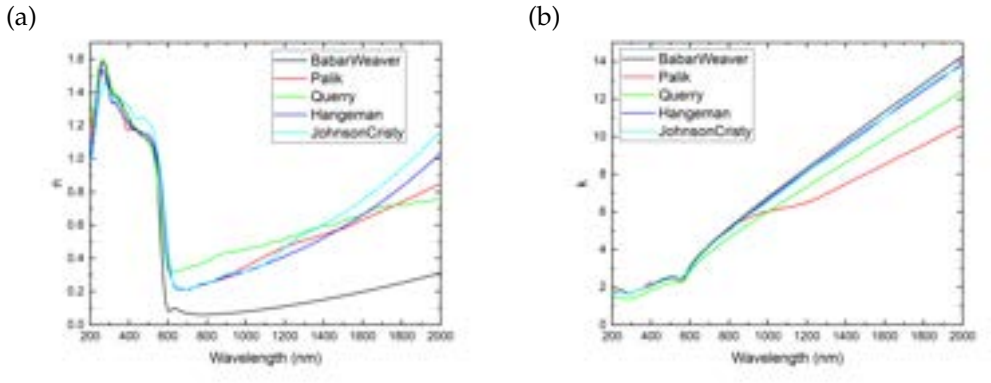

Figure 2.31: Real part **(a)** and imaginary part **(b)** of the reported refractive index for Copper. At low wavelengths they have the same behaviour, but diverge at high wavelengths.

2.4.2.6 Computation

Computations were made using Hangeman refractive index from [43] for Copper (because it lay in the middle of the other curves), Palik refractive index from [44] for CuO and Cu_2O, Moutzouris and Kozma refractive index from [43] for Methanol and Sani refractive index from [43] for Ethanol.

Quasistatic case (Figure 2.32) show a descendent behaviour in the range $200 - 600nm$ for every particle size and a small peak before $600nm$. No differences for particle size are evident except for the scale.

Mie scattering computations (Figure 2.33) shows a completely different behaviour. Small particles recall the quasistatic case as expected. Increasing the particle size, the small peak before $600nm$ starts growing in intensity and broadening and shifting to high wavelength: this is the electric dipole peak. At a radius of $\sim 120nm$ another peak appears at $\lambda \approx 600nm$. Also this peak starts growing in intensity (more than the

dipole) and broadening (it stay more sharp than the dipole) and shifting to high wavelength (less than the dipole): this is the electric quadrupole peak. At a radius of $\sim 200nm$ the electric octupole peak appears. Electron mean free path in Copper is reported to be $39.9nm$ [45], at this size quasistatic approach dominate, so size correction of Equation 2.18 was not used. Absorption spectrum of Copper NPs solutions in Figure 2.7(a) resemble the quasistatic case for small wavelength and Mie case (radius $\sim 150nm$) for higher wavelength due to the large shoulder that is nothing but the large electric dipole peak.

The simulated spectra at the laser wavelength ($1064nm$) presents a cross section that grows with the particle size. The biggest particles so are not transparent to IR light and can absorb the laser beam again and be fragmented in smaller ones. This explain the very small radius of the particles obtained with TEM in Figures 2.11(f) (Cu_met) and 2.12(d) (Cu_et).

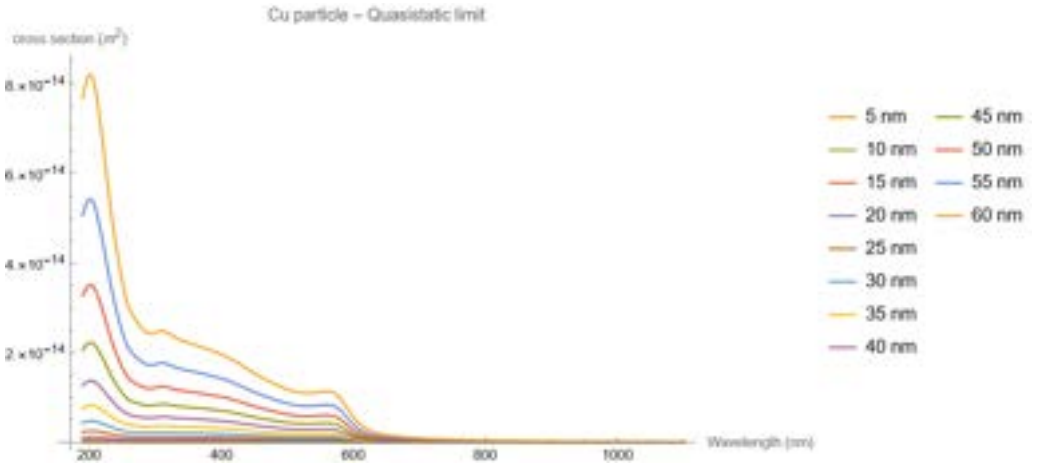

Figure 2.32: Quasistatic case extinction cross section for different radius of Copper NP from $5nm$ to $60nm$ with steps of $5nm$.

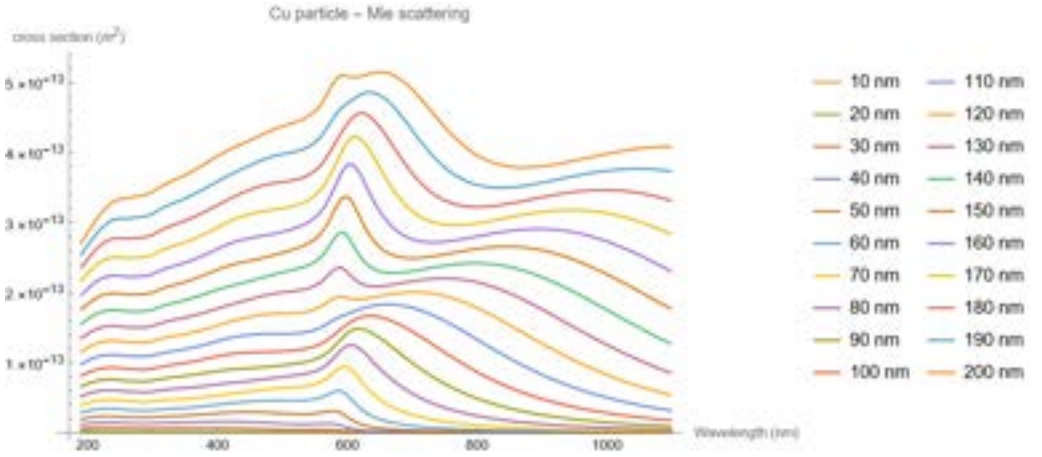

Figure 2.33: Mie extinction cross section for different radius of Copper NP from $10nm$ to $200nm$ with steps of $10nm$.

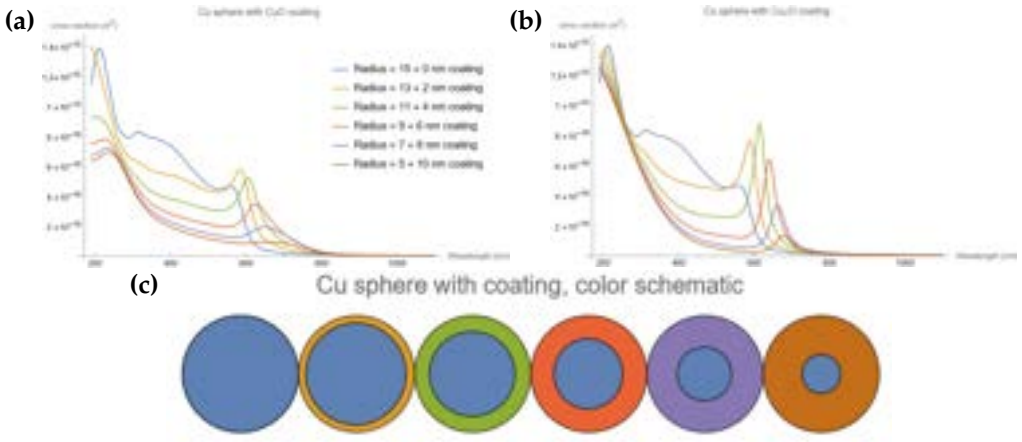

Figure 2.34: Mie extinction cross section for Copper NP of $15nm$ radius covered with different **(a)**: CuO and **(b)** Cu_2O shell. **(c)**: Schematic representation of core-shell structure for different colors in the legend. The legend is the same for all graphs.

The effects of an oxide shell are also simulated (Figure 2.34) using a $15nm$ radius sphere as starting point and adding various shell. The peak part (after $600nm$) behave similar to the metal particle except for the peak sharpness (more sharp for Cu_2O than CuO). The region before $600nm$ acts

different, increasing the cross section at small wavelength with the shell thickness. Comparison with Figure 2.7 suggest no Cu_2O shell because the main peak is not sharp.

2.4.2.7 Particle distribution

SEM and TEM images indicate the presence of particles of different size with a proper distribution. The total cross section $\sigma(\omega)$ come from the contribution of every particles by integrating the size depending cross section $\sigma(\omega, r)$ multiplied by the (normalized) size distribution $f(r)$ over an infinite range. This cannot be realized computationally so the distribution become discrete and the integral become a sum over a finite range (from $r = 0$ to a certain $r = R$ where the distribution is ~ 0) [39]:

$$\sigma(\omega) = \frac{\int_0^\infty f(r)\sigma(\omega, r)dr}{\int_0^\infty f(r)dr} \rightarrow \frac{\sum_{r=0}^{r=R} f(r)\sigma(\omega, r)}{\sum_{r=0}^{r=R} f(r)} \tag{2.21}$$

2.4.2.8 Best results

Best results are obtained using a log normal distribution to represent the small particles ($1 \sim 20nm$ radius) in combination with a gaussian distribution that represents the big particles (up to $200nm$ radius). Parameter were adjusted to match IR zone (big particles) and UV zone (small particles) separately and then joint together. An automatic fitting routine was not implemented due to high computation times and to preserve the physical significance of the all parameters related also to the other measures.

Cu_met spectrum in Figure 2.7(a) is similar to one simulated using a gaussian distribution with $\mu = 120nm, \sigma = 5nm$ (mean and standard deviation) and a lognormal distribution of $x_c = 2.1nm, w = 0.62$ (TEM distribution in Figure 2.11(f)) in Figure 2.35. Cross section depends also on the numbers of particles so to match the scales the lognormal was multiplied by 6000. This implies there are much more small particles

than big ones. In particular, the simulation matches very well the zone with wavelength $< 300nm$ and perfectly match the zone $> 800nm$.

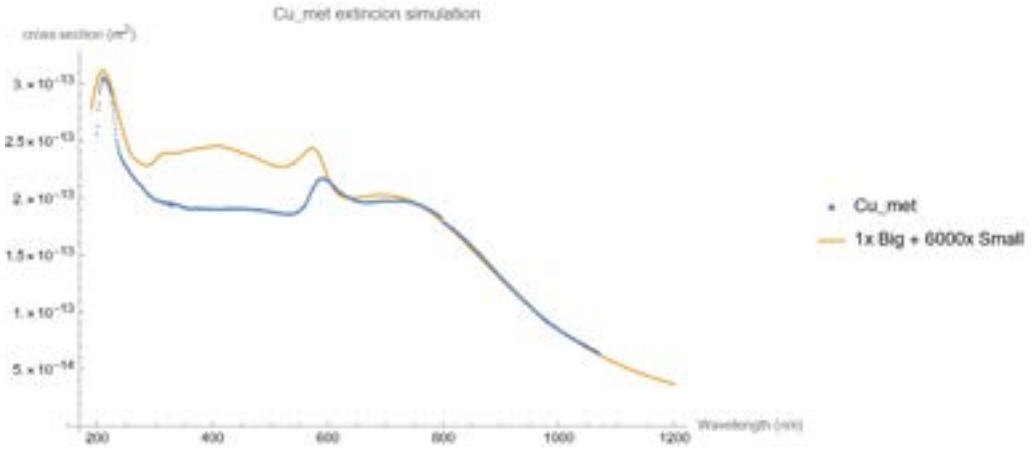

Figure 2.35: Best results: simulated spectra for Copper in methanol, gaussian distribution ($\mu = 120nm, \sigma = 5nm$) plus lognormal distribution ($x_c = 2.1nm, w = 0.62$) in radius with different weights (yellow) and *Cu_met* absorption data (blue).

Cu_et spectrum in Figure 2.7(a) is similar to one simulated using a gaussian distribution of $\mu = 145nm, \sigma = 15nm$ and a lognormal distribution of $x_c = 3.3nm, w = 0.52$ (TEM distribution in Figure 2.12(d)) in Figure 2.36. To match the scales the lognormal was multiplied by 7000. Also in this case the small particles are way more than the big ones. In particular, the simulation perfectly match the zone with wavelength $> 700nm$.

Simulations with oxides layer did not produced any matching spectrum, so this simulations suggest pure metals NPs. Even simulation of combination of small oxide NPs and bigger pure metal particles did not produced reasonable changes in spectrum. A polymer layer of any thickness does not produce any change in absorption or scattering because the used refractive index $n = 1.55$ [35] is real and similar to the solvent one.

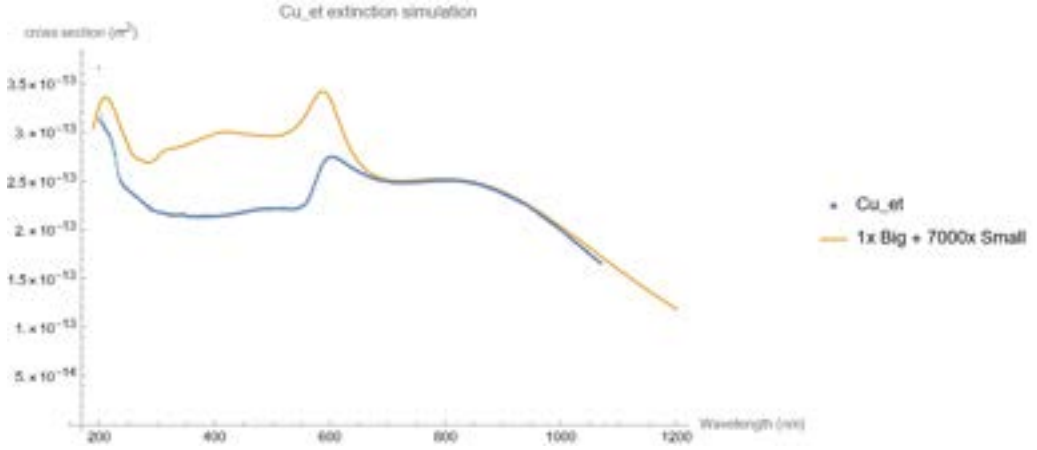

Figure 2.36: Best results: simulated spectra for Copper in ethanol, gaussian distribution ($\mu = 145nm, \sigma = 15nm$) plus lognormal distribution ($x_c = 3.3nm, w = 0.52$) in radius with different weights (yellow) and *Cu_et* absorption data (blue).

In both cases simulations suggest the presence of a large amount of small particles and very few bigger particles. Bigger particles however contribute a lot to cross section, this catches the eye looking at the scale in Figures 2.32 and 2.33 and their order of magnitude. But in previous Section was proved that the big particles are nothing but agglomerate of small particles. The matching optical spectrum especially in the high wavelength region indicates that this agglomerates optically acts like metal spherical particles even if they are partially made of polymer. More in general this simulation works ONLY with spherical particles, in fact that spectrum and simulation wont match in the region $300 - 600nm$, indicating non spherical particles. But this mismatch can come also from some other physical phenomena involving smaller agglomerates of metal NPs and polymer.

Simulation on Nickel did not produced any valuable results especially in matching the strong absorption in the UV region of Figure 2.7(a). The fault may be the strong difference in the tabulated refractive index or the presence of chemical compounds on the surface highlighted by XPS.

2.5 Summary

Here it is a final summary of the all the analysis and measures conducted on the NPs. The following Tables contains the analysis conducted, the results obtained and the reference Section of this Chapter were they are discussed.

Copper NPs produced in **methanol** (*Cu_met*) characterizations are summarized in Table 2.2. These particles are metallic sphere of radius $\sim 2nm$ covered by a polymer that forms clusters.

The same situation and size, but with a thicker layer of polymer, is for **Copper** NPs produced in **ethanol** (*Cu_et*), whose characterizations are summarized in Table 2.3.

Nickel NPs produced in **methanol** (*Ni_met*) characterizations are summarized in Table 2.4. These particles are metallic spheres (radius $\sim 480nm$) covered by a polymer and aggregated in clusters.

Analysis	**Result**	**Section**
Optical	Metallic Cu, Mostly sphere, Clusters	2.3.1 2.4.2.8
SEM	Big spheres ($x_c = 47nm, w = 0.67$)	2.3.2.1
TEM	Small spheres ($x_c = 2.1nm, w = 0.62$) Presence of agglomerate of small NPs Interplanar distances suggests metallic Cu Electron diffraction indicates metallic Cu	2.3.3.1 2.3.3.3 2.3.3.4
XRD	Metallic Cu	2.3.4
XPS	Mostly metallic Cu, Presence of polymer Surface compounds	2.3.5.1 2.4.1
EDX	Metallic NPs Presence of polymer	2.3.6

Table 2.2: Characterization of **Copper** NPs produced in **methanol** (*Cu_met*).

Analysis	Result	Section
Optical	Metallic Cu, Mostly sphere, Clusters	2.3.1,2.4.2.8
SEM	Spheres ($x_c = 43nm, w = 0.69$)	2.3.2.2
TEM	Small spheres ($x_c = 3.3nm, w = 0.52$) Presence of thick polymer Interplanar distances of Cu	2.3.3.2, 2.3.3.3
XRD	Metallic Cu	2.3.4
XPS	Presence of thick polymer	2.3.5.2, 2.4.1

Table 2.3: Characterization of **Copper** NPs produced in **ethanol** (*Cu_et*).

Analysis	Result	Section
Optical	Metallic Ni, Clusters	2.3.1
SEM	Big spheres ($x_c = 484nm, w = 0.47$) Linear clusters Big NPs decorated with small NPs	2.3.2.3
XRD	Metallic Ni	2.3.4
XPS	Presence of polymer Surface compounds	2.3.5.3,2.4.1

Table 2.4: Characterization of **Nickel** NPs produced in **methanol** (*Ni_met*).

Bibliography

[1] Vincenzo Amendola, David Amans, Yoshie Ishikawa, Naoto Koshizaki, Salvatore Scirè, Giuseppe Compagnini, Sven Reichenberger, and Stephan Barcikowski. Room-temperature laser synthesis in liquid of oxide, metal-oxide core-shells, and doped oxide nanoparticles. *Chemistry – A European Journal*, 26(42):9206–9242, July 2020. doi:10.1002/chem.202000686.

[2] Stephan Barcikowski, Vincenzo Amendola, Galina Marzun, Christoph Rehbock, Sven Reichenberger, Dongshi Zhang, and Bilal Gökce. Handbook of laser synthesis of colloids. 2016. URL: http://duepublico.uni-duisburg-essen.de/servlets/DocumentServlet?id=41087, doi:10.17185/DUEPUBLICO/41087.

[3] Hongkun Huang, Jiancheng Lai, Jian Lu, and Zhenhua Li. Pulsed laser ablation of bulk target and particle products in liquid for nanomaterial fabrication. *AIP Advances*, 9(1):015307, January 2019. doi:10.1063/1.5082695.

[4] Maria Censabella, Valentina Iacono, Antonino Scandurra, Kaveh Moulaee, Giovanni Neri, Francesco Ruffino, and Salvatore Mirabella. Low temperature detection of nitric oxide by CuO nanoparticles synthesized by pulsed laser ablation. *Sensors and Actuators B: Chemical*, 358:131489, May 2022. doi:10.1016/j.snb.2022.131489.

[5] Talshyn Begildayeva, Seung Jun Lee, Yiseul Yu, Juhyeon Park, Tae Ho Kim, Jayaraman Theerthagiri, Ahreum Ahn, Hyeon Jin Jung, and Myong Yong Choi. Production of copper nanoparticles exhibiting various morphologies via pulsed laser ablation in different solvents and their catalytic activity for reduction of toxic nitroaromatic compounds. *Journal of Hazardous Materials*, 409:124412, May 2021. doi:10.1016/j.jhazmat.2020.124412.

[6] Enza Fazio, Bilal Gökce, Alessandro De Giacomo, Moreno Meneghetti, Giuseppe Compagnini, Matteo Tommasini, Friedrich Waag, Andrea Lucotti, Chiara Giuseppina Zanchi, Paolo Maria Ossi,

Marcella Dell'Aglio, Luisa D'Urso, Marcello Condorelli, Vittorio Scardaci, Francesca Biscaglia, Lucio Litti, Marina Gobbo, Giovanni Gallo, Marco Santoro, Sebastiano Trusso, and Fortunato Neri. Nanoparticles engineering by pulsed laser ablation in liquids: Concepts and applications. *Nanomaterials*, 10(11):2317, November 2020. doi:10.3390/nano10112317.

[7] Bahaa E A Saleh and Malvin Carl Teich. *Fundamentals of Photonics*. Wiley Series in Pure and Applied Optics. Wiley-Blackwell, Chichester, England, 2 edition, February 2007.

[8] Francesco Ruffino and Maria Grazia Grimaldi. Nanostructuration of thin metal films by pulsed laser irradiations: A review. *Nanomaterials*, 9(8):1133, August 2019. doi:10.3390/nano9081133.

[9] Hyeon Jin Jung and Myong Yong Choi. Specific solvent produces specific phase ni nanoparticles: A pulsed laser ablation in solvents. *The Journal of Physical Chemistry C*, 118(26):14647–14654, June 2014. doi:10.1021/jp503009a.

[10] Talshyn Begildayeva, Deviprasath Chinnadurai, Seung Jun Lee, Yiseul Yu, Jae Kyu Song, and Myong Yong Choi. Implementation of novel pulsed laser ablation strategy to control the morphological growth and enrich the electrochemically active sites of multifunctional ni–CuO electrocatalyst. *Journal of Alloys and Compounds*, 901:163446, April 2022. doi:10.1016/j.jallcom.2021.163446.

[11] Michael Quinten. *Optical properties of nanoparticle systems*. Wiley-VCH Verlag, Weinheim, Germany, January 2011.

[12] Stefano Boscarino, Maria Censabella, Melanie Micali, Marco Russo, Antonio Terrasi, Maria Grazia Grimaldi, and Francesco Ruffino. Morphology, electrical and optical properties of cu nanostructures embedded in AZO: A comparison between dry and wet methods. *Micromachines*, 13(2):247, February 2022. doi:10.3390/mi13020247.

[13] Lu-Syuan Jhuang, Gautham Kumar, and Fang-Chung Chen. Localized surface plasmon resonance of copper nanoparticles improves

the performance of quasi-two-dimensional perovskite light-emitting diodes. *Dyes and Pigments*, 188:109204, April 2021. doi:10.1016/j.dyepig.2021.109204.

[14] Jagmeet Singh Sekhon and S S Verma. Cu, CuO, and cu2o nanoparticle plasmons for enhanced scattering in solar cells. In *Renewable Energy and the Environment*. OSA, 2011. doi:10.1364/e2.2011.jwe22.

[15] P. Lobotka, G. Radnoczi, Z. Czigany, I. Vavra, M. Drzik, M. Micusik, E. Dobrocka, and P. Kunzo. Preparation of nickel, nickel-iron, and silver-copper nanoparticles in ionic liquids. In *2013 Transducers Eurosensors XXVII: The 17th International Conference on Solid-State Sensors, Actuators and Microsystems*. IEEE, June 2013. doi:10.1109/transducers.2013.6627194.

[16] Ahmed M. El-Khatib, Mohamed S. Badawi, Gamal D. Roston, Ramy M. Moussa, and Moustafa M. Mohamed. Structural and magnetic properties of nickel nanoparticles prepared by arc discharge method using an ultrasonic nebulizer. *Journal of Cluster Science*, 29(6):1321–1327, September 2018. doi:10.1007/s10876-018-1451-x.

[17] Imagej. https://imagej.nih.gov/ij/index.html.

[18] Kuang-Hua Chang. Reliability analysis. In *e-Design*, pages 523–595. Elsevier, 2015. doi:10.1016/b978-0-12-382038-9.00010-7.

[19] C.G. Granqvist and R.A. Buhrman. Log-normal size distributions of ultrafine metal particles. *Solid State Communications*, 18(1):123–126, January 1976. doi:10.1016/0038-1098(76)91415-0.

[20] Gatan microscopy suit software. https://www.gatan.com/products/tem-analysis/gatan-microscopy-suite-software.

[21] Carine crystallography. http://carine.crystallography.pagesperso-orange.fr/.

[22] M. Klinger. *CrysTBox - Crystallographic Toolbox*. Institute of Physics of the Czech Academy of Sciences, Prague, 2015. URL: http://www.fzu.cz/~klinger/crystbox.pdf.

[23] Pdf card no.: 00-004-0836 quality:s.

[24] Pdf card no.: 00-089-5895 quality:c.

[25] Pdf card no.: 00-077-0199 quality:c.

[26] Pdf card no.: 00-004-0850 quality:s.

[27] Pdf card no.: 00-047-1049 quality:s.

[28] John F Moulder, William F Stickle, and Peter E Sobol. *Handbook of X-ray photoelectron spectroscopy*. Perkin-Elmer, Physical Electronics Division, September 1992.

[29] Xpspeaks41. `https://xpslibrary.com/wp-content/uploads/2019/09/xpspeak41.zip`.

[30] M.R. Pinnel, H.G. Tompkins, and D.E. Heath. Oxidation of copper in controlled clean air and standard laboratory air at 50°c to 150°c. *Applications of Surface Science*, 2(4):558–577, May 1979. `doi:10.1016/0378-5963(79)90047-3`.

[31] A N Oraevskii, V P Pimenov, A A Stepanov, and V A Shcheglov. Laser polymerization in gases. *Soviet Journal of Quantum Electronics*, 4(5):711–712, May 1974. `doi:10.1070/qe1974v004n05abeh009302`.

[32] I N Kal'vina, V F Moskalenko, E P Ostapchenko, L L Pavlovskii, T V Protsenko, and V I Rychkov. Resonant action of laser radiation on polymerization processes. *Soviet Journal of Quantum Electronics*, 4(10):1285–1286, October 1975. `doi:10.1070/qe1975v004n10abeh011755`.

[33] Pietro Marabotti, Sonia Peggiani, Alessandro Vidale, and Carlo Spartaco Casari. Pulsed laser ablation in liquid of sp-carbon chains: Status and recent advances. *Chinese Physics B*, 31(12):125202, December 2022. `doi:10.1088/1674-1056/ac81b2`.

[34] Bryan R. Coad, Tanja Scholz, Krasimir Vasilev, John D. Hayball, Robert D. Short, and Hans J. Griesser. Functionality of proteins bound to plasma polymer surfaces. *ACS Applied Materials and Interfaces*, 4(5):2455–2463, April 2012. `doi:10.1021/am300128n`.

[35] Hasan D. Hazrati, Jason D. Whittle, and Krasimir Vasilev. A mechanistic study of the plasma polymerization of ethanol. *Plasma Processes and Polymers*, 11(2):149–157, January 2014. doi:10.1002/ppap.201300110.

[36] Craig F Bohren and Donald R Huffman. *Absorption and scattering of light by small particles*. John Wiley & Sons, Nashville, TN, April 1998.

[37] Uwe Kreibig and Michael Vollmer. *Optical properties of metal clusters*. Springer Series in Materials Science. Springer, Berlin, Germany, December 2010.

[38] Ahmed Al-Kattan, Gleb Tselikov, Khaled Metwally, Anton A. Popov, Serge Mensah, and Andrei V. Kabashin. Laser ablation-assisted synthesis of plasmonic si@au core-satellite nanocomposites for biomedical applications. *Nanomaterials*, 11(3):592, February 2021. doi:10.3390/nano11030592.

[39] Vincenzo Amendola and Moreno Meneghetti. Size evaluation of gold nanoparticles by UV-vis spectroscopy. *The Journal of Physical Chemistry C*, 113(11):4277–4285, February 2009. doi:10.1021/jp8082425.

[40] Antonio Rivera Ovidio Peña-Rodríguez Konstantin Ladutenko, Umapada Pal. Mie calculation of electromagnetic near-field for a multilayered sphere. https://physics.itmo.ru/en/mie#/spectrum.

[41] Mie plot. http://www.philiplaven.com/mieplot.htm.

[42] Andrea Baldi. Mie_scattering_and_absorption_sphere. https://github.com/andrea-baldi/Mie_Scattering_and_Absorption_Sphere/releases/tag/v1.0.2.

[43] Refractiveindex.info. https://refractiveindex.info/.

[44] *Handbook of optical constants of solids*. Handbook of Optical Constants of Solids. Academic Press, San Diego, CA, June 1985.

[45] Daniel Gall. Electron mean free path in elemental metals. *Journal of Applied Physics*, 119(8):085101, February 2016. doi:10.1063/1.4942216.

Chapter 3

Electrochemical measurements

This Chapter will describe the techniques used for the preparation of the electrodes and the measurements conducted on them. The electrode characterization is performed by Scanning Electron Microscopy and Rutherford Backscattering Spectrometry. Electrochemical measurements are performed using Cyclic Voltammetry, Linear Sweep Voltammetry, Electrochemical Impedance Spectroscopy and Mott Schottky. The thoretical background of the electrochemical tecniques used is firstly explained and, then, the experimental results are presented and discussed. At the end of this chapter, data interpretation is discussed and, finally, the results found in this work are compared with the literature.

3.1 Electrodes preparation

For the electrochemical tests Graphene Paper (GP) (240μm thick, Sigma Aldrich, St. Louis, MO, USA) and Nichel Foam (NF) (Goodfellow Inc., Huntingdon, England, thickness 1.6mm, porosity $\geq$ 95%) were used as substrates for the WE. Firstly, the bare substrate was tested as WE. Then the NPs loaded on the substrate were characterized. Thus, Copper in methanol (Cu_met), Copper in ethanol (Cu_et), Nickel in methanol (Ni_met) and both Copper in ethanol and Nickel in methanol ($Cu\_et + Ni\_met$). The last mixed NPs come from a different solution that was previously prepared by mixing 50ml of Cu_et and 50ml of Ni_met in another con-

tainer.

Substrates were first cut in a rectangular shape with the shorter side of about $1cm$ and then rinsed with deionized water and dried in N_2 to clean their surface. Electrodes are prepared by drop casting $60\mu l$ of sonicated and handshacked NP solution on substrates. Then electrodes are dried on a hot plate. Methanol boiling temperature is $64.7°C$ and ethanol boiling temperature is $78.4°C$ [1], so the hot plate was kept at $\sim 80°C$ for about one hour to guarantee the complete solvent evaporation and drying.

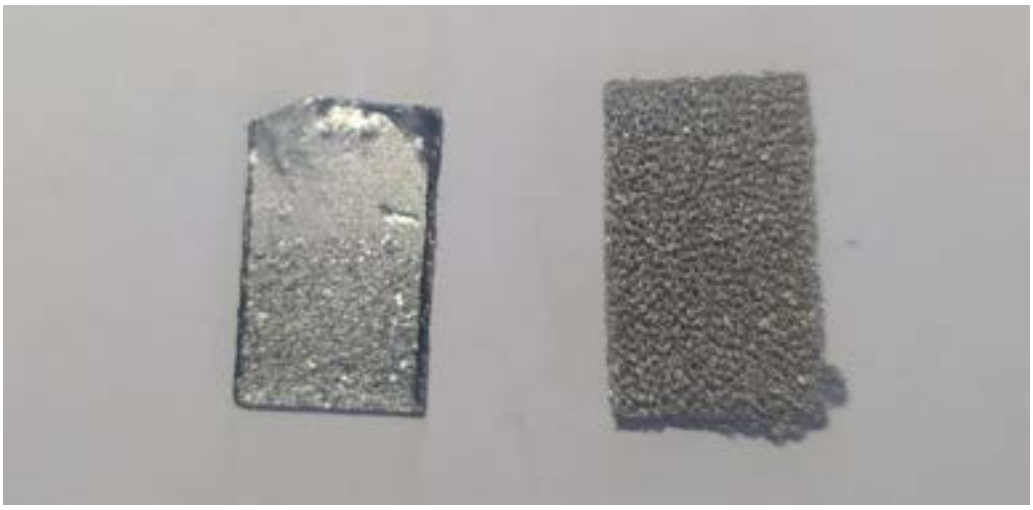

Figure 3.1: Example of GP substrate on the left and NF on the right. The amount of NPs is so low that they are not visible to the eye and with the camera. The different appearance of the lower part of the GP electrode is due to the corrosion occurred during the electrochemical measures.

3.1.1 Rutherford Backscattering Spectrometry

On GP substrates, Rutherford Backscattering Spectrometry (RBS) analysis (see appendix E) was conducted to evaluate the mass of deposited catalyst material. Dose ($atoms/cm^2$) was evaluated by integrating the specific element peak using the software `RUMP` [2]. In Figure 3.2 are shown the RBS spectra of the samples. They presents a well defined peak referred to Nickel ($1.522MeV$) and Copper ($1.554MeV$). As seen in Table 2.1, *Cu_met* presents the lowest amount of ablated mass followed by *Cu_et* and the

highest was the Nickel. This can indicates that the dropped solution was picked up uniformly from the solutions. The significant presence of Carbon comes from GP substrate and also a oxygen is present according to the consideration about polymer (Section 2.4.1) and from the dried solvent.

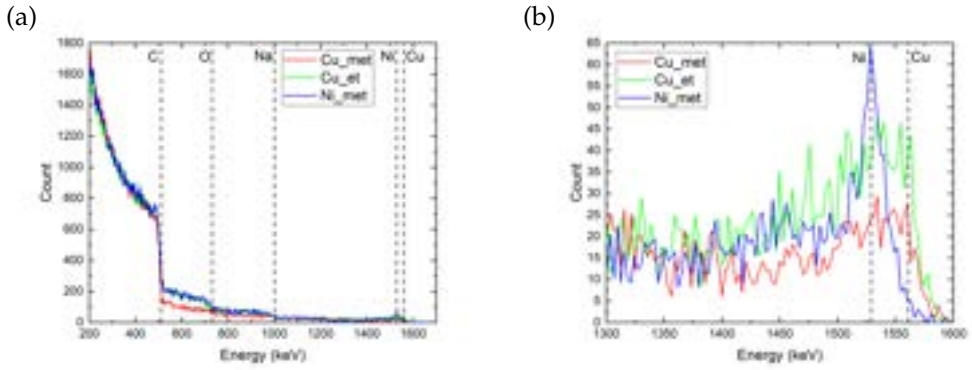

Figure 3.2: (a): RBS spectrum of the GP electrodes. Vertical lines represents the scattering energy of Carbon 511.7keV, Oxygen 731.8keV, Nickel 1.529MeV and Copper 1.561MeV [2]. **(b)**: Zoom on the Copper and Nickel zone.

Drop casting was performed on a surface $A = 1cm^2$, so knowing the dose (at/cm^2) and the atomic mass u, the total deposited mass m can be evaluated:

$$m = u\frac{Dose}{N_A}A \tag{3.1}$$

where N_A is the Avogadro's number. From the consideration in Chapter 2 the NPs are reported to be metallic, so the used atomic masses are the ones of Nickel and Copper. Catalyst doses and masses are reported in Table 3.1.

Sample	Dose $[at/cm^2]$	Mass $[\mu g/cm^2]$
Cu_met	$7.73 \cdot 10^{15}$	0.8
Cu_et	$1.08 \cdot 10^{16}$	1.1
Ni_met	$7.35 \cdot 10^{15}$	0.7

Table 3.1: Catalyst mass evaluated for each electrode.

Since the drop casting conditions were the same, the catalyst mass are the same both on GP and NF. Also the deposited mass on the mixed sample is considered given by the sum of the mass evaluated on the previous samples divide by two: $Cu\_et + Ni\_met$: Mass $= 0.9 \mu g/cm^2$.

3.1.2 Scanning Electron Microscopy

Figures 3.3 shows some SEM images of the various electrodes.

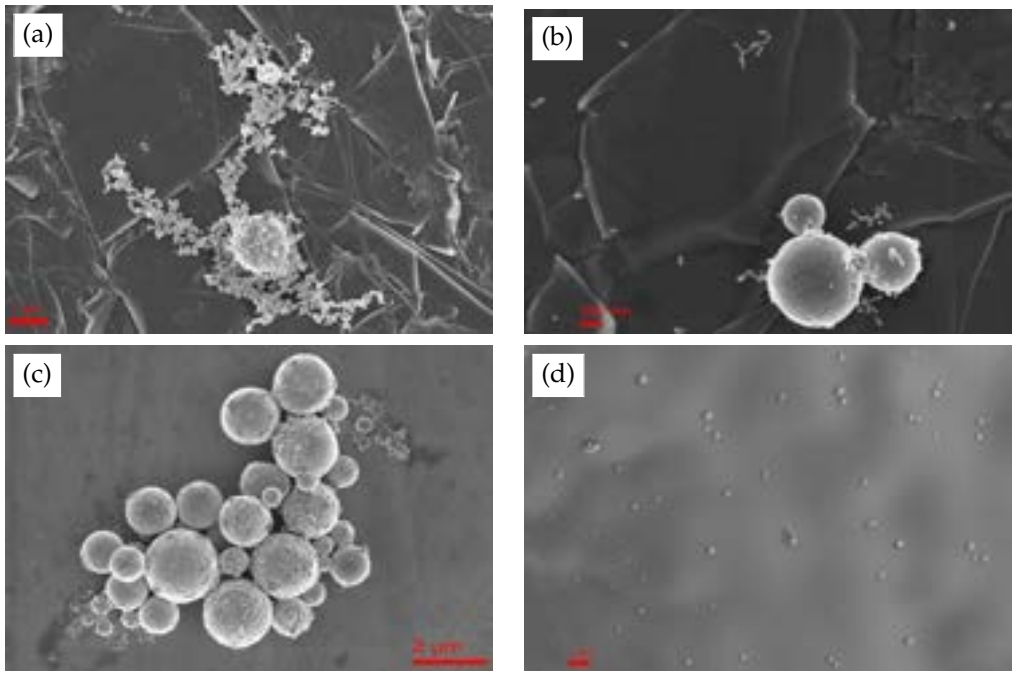

Figure 3.3: SEM images of **(a)**: Cu_et on GP, **(b)**: Ni_met on GP, **(c)**: $Cu\_et + Ni\_met$ on GP and **(d)**: Cu_met on NF.

The GP shows a mostly flat surface made up by stacked sheets with a lot of edge and corner that increases its surface. The NPs appears in clusters but these clusters are uniformly distributed on the surface. The NPs in the $Cu\_et + Ni\_met$ sample are apparently not distinguishable, but from the size distribution of Section 2.3.2 apparently big Nickel clusters with appended at the side Copper cluster like in Figure 3.3(c).

The NF shows a smooth and undulatory surface with some bubbles that are the interested NPs. Also in this case there the cluster are smaller than on GP and also uniformly distributed.

3.2 Experimental setup

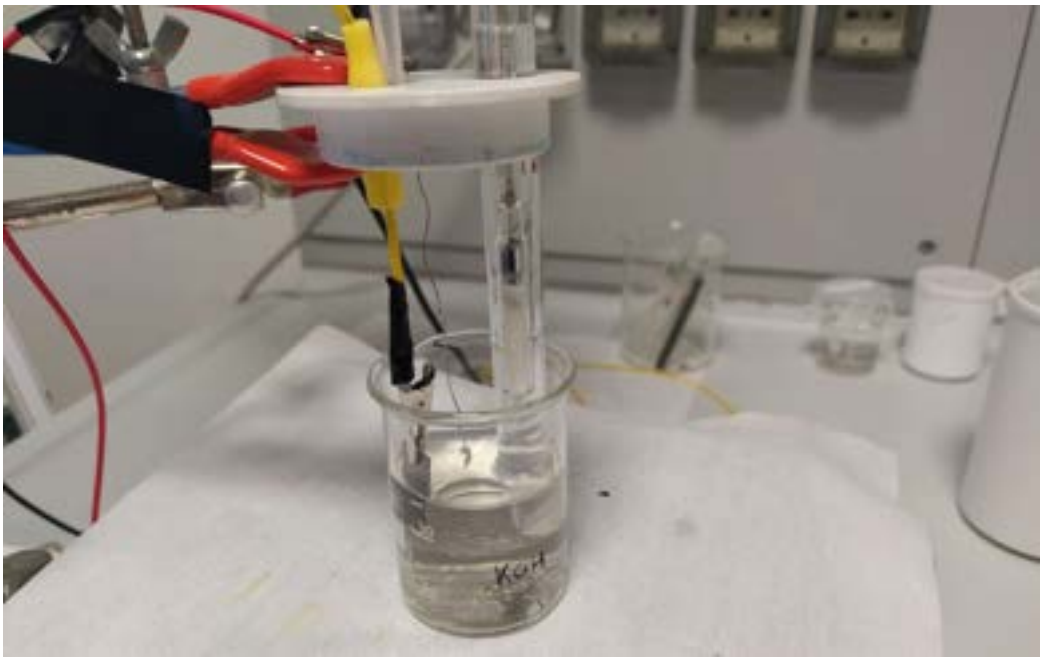

Figure 3.4: Used electrochemical cell filled with $40ml$ of aqueous $1M\ KOH$. The studied WE is attached at the yellow wire and is partially immersed, the CE is a platinum wire on the back and the RE is a SCE on the right.

To perform electrochemical analysis the following apparatus was made up: a quartz beaker was filled with $40ml$ of $1M\ KOH$ aqueous solution ($pH = 14$). The WE are the previously prepared electrodes with an immersed surface of $1cm^2$. The CE is a platinum wire and the RE is a SCE. These electrodes are wired to a `VersaSTAT 4` potentiostat controlled by `VersaStudio` software [3]. This software and hardware are able to perform a variety of electrochemical measures and analysis. Once a WE is equipped, all the electrochemical measures are conducted right away to

avoid contamination due to possible changes in any of the setup parameter.

3.3 Electrochemical characterization

In this Section the the theory and the information that can be extracted from the various measures are explained.

3.3.1 Cyclic Voltammetry

The first measurement in the study of an electrode is the Cyclic Voltammetry (CV). In this analysis the potential on WE is slowly changed linearly from a starting potential to a switching potential and back while the flowing current is measured [4]. Usually the starting point is $0V$ th the RE and the ending potential is chosen high enough to reach and overcome $10mA/cm^2$, once for OER and for HER, depending on the potential regions. Cycles are repeated until stability is reached. NF substrates present some peaks typical of oxidation and reduction of Nickel. These peaks are different in the forward an backward branches: the oxidation reaction occurs at higher potentials than the reduction reaction. In this particular case Nickel goes from Ni^{2+} to $Ni^{3+} + e^-$ in the forward scan (and so the reverse in backward scan) [5]. Once the potential required for this reaction is reached, the current is expected to keep growing, but at some potential the current goes down because the extension of the diffusion layer blocks the mass transport [4]. Nickel peaks should be visible also in the measure on GP, but the amount of material is so low that peaks has a very low amplitude and are eventually covered by the substrate peaks, the same is for Copper oxidation and reduction peaks [6]. Figure 3.5 report some examples of CV with oxidation and reduction peaks.

The scan rate of the experiment controls how fast the applied potential is scanned. Faster scan rates lead to a decrease in the size of the diffusion layer; as a consequence, higher currents are observed [4]. Measures in this work are performed at a scan rate of $10mV/s$ (low scan rate). HER measurements on GP goes from $0V$ to $-1.7V$, on NF goes from $0V$

to $-1.5V$ (both vs. SCE). OER measurements on both GP and NF goes from $0V$ to $+0.7V$ vs. SCE. Also in Figure 3.5 is possible to see that NF slightly gets better at every cycle: the curve shifts to left at high potential and characteristic peaks rise in intensity, GP slightly gets worse, but both stabilize. From this kind of measure is possible to understand how the electrode evolves in time and its necessary to stabilize the electrode. Furthermore gives a gross estimation of the oxidation/reduction reactions and information of the potential at which the OER or the HER starts.

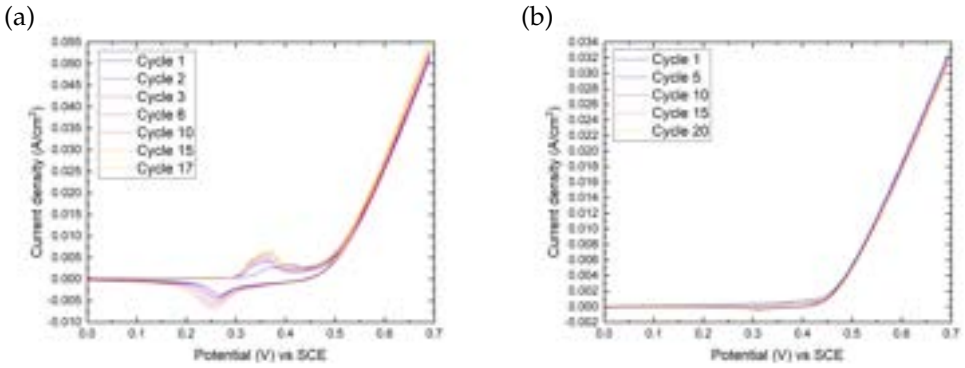

Figure 3.5: Example of CV measurements for OER. **(a)**: *Cu_met* on NF and **(b)**: *Ni_met* on GP. Not all cycle are reported to evince the differences. Nickel oxidation peaks are presents in both graph: in (a) they are more evident and come from the substrate, in (b) they come from the NPs and are much less evident.

3.3.2 Linear Sweep Voltammetry

In Linear Sweep Voltammetry (LSV) the potential on WE is slowly changed linearly from a starting potential to a final potential. This analysis occurs when the WE is stable and from the LSV curve, overpotential and Tafel slope are extracted. A logarithmic plot of the LSV current density against the overpotential gives the Tafel plot. Both LSV and Tafel plots give an overview on the electrode kinetic. LSV are performed at a scan rate of $5mV/s$ in the same ranges of CV.

An example of this measurement is provided in Figure 3.6, where the LSV of bare GP is analyzed for HER. Figure 3.6(a) shows a descendent

behaviour from $0V$ to negative potentials. At around $\sim -1.0V$ there is a small peak due to some oxidation reaction happening on the substrate. At $\sim -1.4V$ the current starts descend rapidly. The Tafel plot helps in understanding what happens on the electrode. Initially the current is due to the ion movement in solutions and grow exponentially with the applied potential (Nernst Equation 1.6). The Tafel plot in Figure 3.6(b) is in logarithmic scale so all the exponential behaviours become linear behaviours and are easy to find: the first linear zone in the plot is due to ionic current at very low potential and current. Up to $1.2V$ there is the region corresponding to oxidation peak and over $1.4V$ there is finally the HER linear behaviour (marked blue line). In next Section LSV and Tafel plots will be presented for each electrode.

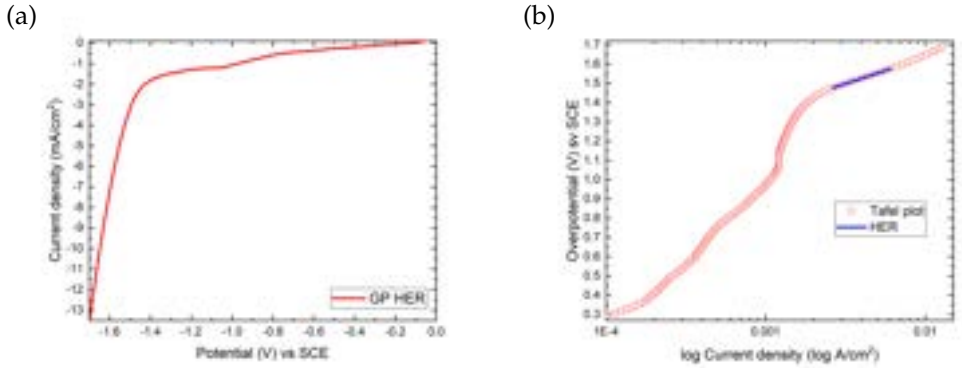

Figure 3.6: (a): Example of LSV measurements on bare GP for HER and **(b)** relative Tafel plot with linear zone marked.

Before proceeding, the potential scale must be converted from SCE (V_{SCE}) to RHE (V_{RHE}) to obtain the overpotential [7]:

$$\begin{aligned} \text{HER: } V_{RHE} &= V_{SHE} + 0.241 + 0.059pH - E_c^0 - iR \\ \text{OER: } V_{RHE} &= V_{SHE} + 0.241 + 0.059pH - E_a^0 - iR \end{aligned} \tag{3.2}$$

The term $+0.241[V]$ is SCE to SHE conversion, the term $+0.059pH[V]$ is the pH correction of the SHE to RHE conversion, E_c^0 and E_a^0 are the half reaction potentials of cathode and anode (Equations 1.4 and 1.5). In this alkaline case $E_a^0 = 1.23V$ and $E_c^0 = 0V$. Then there is a voltage drop

compensation due to the current i flowing trough the electrode and the resistance R that will be evaluated with EIS.

3.3.3 Electrochemical Impedance Spectroscopy

Electrochemical Impedance Spectroscopy (EIS) is a technique that gives information about the electrode liquid interface and the charge transfer. The liquid-solid interface can be like a capacitor as in Figure 1.9. But also a charge transfer occurs so also a resistor should be considered. With this analysis all the resistance and capacitors can be evaluated.

EIS consists in applying an alternate voltage and measuring the current. This alternate behaviour can be represented by a sin wave or better by a complex exponential of frequency ω, so both the current and the voltage have a real part and an imaginary part. From the Ohm law the resistance becomes a complex number called impedance and has a dependence from frequency ω:

$$R = \frac{V}{I} \rightarrow Z(\omega) = \frac{V(\omega)}{I(\omega)} = \frac{V_{Re} + iV_{Im}}{I_{Re} + iI_{Im}} \tag{3.3}$$

For resistors the impedance is equal to resistance $Z = R$ and is real. For capacitors the impedance is given by $Z = 1/i\omega C$ and the current that flows trough the capacitor have a 90° phase shift respect to the applied voltage. By measuring current oscillation with respect to voltage oscillation, the instrument can provide both the real part and the imaginary part of the impedance and plot Z_{Re} against Z_{Im}.

In general the electrode liquid interface can be represented by a Randel's cell [8, 9] presented in Figure 3.7(a). This circuit is made up by a resistance R_u called uncompensated resistance and then in parallel the capacitor like element Q and the charge transfer resistance R_{ct}.

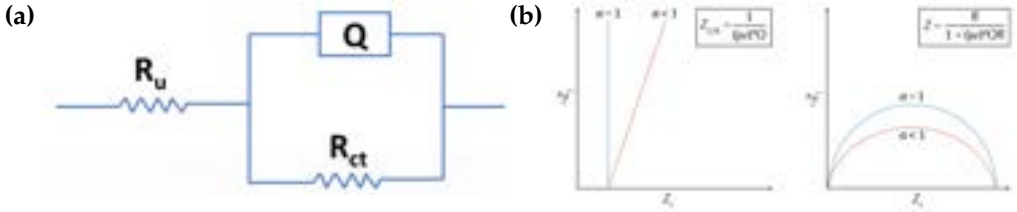

Figure 3.7: (a): Randel's cell circuit. **(b)**: Impedance behaviour of a Constant Phase Element and impedance behaviour of the Randel's cell [8].

The uncompensated resistance represents the solution resistance between the WE and the RE and so depends only on the position between the electrodes and their geometry and in general is different for every electrode. This resistance is the one that appear in the Equations 3.2. The charge transfer resistance R_{ct} is the one that refers on the charge transfer between the electrode and the solution. The element indicated by Q is not proper a capacitor because the electrical double layer is not ideal. For neutral solution this is a Warburg element which have a 45° phase shift between current and voltage that states the intermediate nature of the same between a resistor and a capacitor. In the most general case of electrodes non perfectly flat a Constant Phase Element (CPE) is used. It's impedance is given by:

$$Z_{CPE} = \frac{1}{(i\omega)^{\alpha} Q} \tag{3.4}$$

where there is an exponent α that controls the phase shift.

The meaning of the plot in Figure 3.7(b) is that at high frequencies the capacitor/CPE acts like a short circuit so the only impedance is the R_u and is real. At low frequencies the capacitor/CPE do not contribute to the current acting like an insulator so the total impedance is given by $R_u + R_{ct}$ and is once again real. At intermediate frequency the impedance has an imaginary part that is represented by a semicircle if $\alpha = 1$ (perfect capacitor) or a depressed semicircle if $\alpha < 1$ (Constant Phase Element).

When the surface is partially covered by nanostructured catalysts the Armstrong and Henderson circuit is used [8, 10].

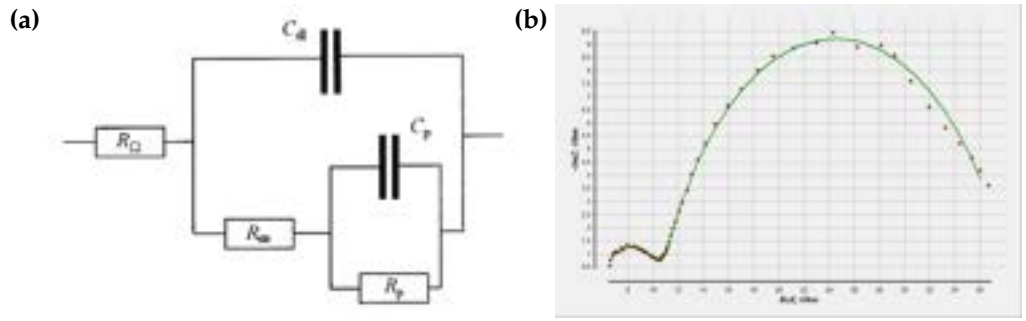

Figure 3.8: (a): Armstrong and Henderson equivalent circuit [10]. **(b)**: An example of EIS spectrum of GP decorated with PLAL obtained $Cu\_et + Ni\_met$ NPs for OER fitted and plotted with [11].

This circuit, in Figure 3.8(a), contains one more capacitor and one more resistor. The meaning of the uncompensated resistance R_u (in Figure R_Ω) is the same. The element C_{ct} and R_{ct} (in Figure C_{dl} and R_∞) are related to the charge transfer between the substrate and the adsorbed species (H^+ for HER and OH^- for OER) and represent respectively the double layer capacitance and the charge transfer resistance. The element C_p and R_p (same as Figure) are related to the mass transfer so the kinetic of adsorption and desorption [10]. These two element are in series with R_{ct} because ions must be adsorbed in order to exchange electrons with the electrodes. In this case the spectrum presents two depressed semicircles, but not always the smaller one is well defined and data must be fitted to find the element values.

EIS measurements in this work are performed in the frequency range $100kHz - 0.1Hz$ at a potential a little above the onset potential[1]. There is a debate on which potential should be used [9], but a potential just above the onset potential gives information about the electrode behaviour within the required reaction and can give a comparison between all the electrodes.

[1]The onset potential is the potential at which the HER or OER reaction starts.

3.3.4 Mott Schottky

Mott Schottky (MS) analysis provides information about the band bending at the interface between electrode and electrolyte. The charge layer inside the electrode surface is coupled with the total double layer charge resulting in a capacitor. From the Poisson Equation and the depletion layer thickness (Equations 1.19 and 1.20) is possible to find a relation between the capacitance and the flat-band potential V_{fb} [12]:

$$\frac{1}{C^2} = \frac{2}{\epsilon\epsilon_0 A^2 e N_D}\left(V - V_{fb} - \frac{k_B T}{e}\right) \tag{3.5}$$

where A is the electrode surface and $k_B T/e$ is the contribution given by thermal fluctuation. All measurements were made at the same temperature of $\sim 25°C$ so the term $k_B T/e \approx 25mV$. The Mott Schottky equation (Eq. 3.5) shows a linear dependence between $1/C^2$ and the applied voltage V. Equation 3.5 represents the ideal case and the liquid-solid interface in electrochemical systems follows the linear behaviour only in a narrow potential region [13]. `VersaSTAT 4` potentiostat used in this work can provide capacitance measurement at different potential using alternate current. Figure 3.9 gives an example of Mott Schottky plot (Potential against $1/C^2$). A linear fit in the linear zone is used to provide the voltage axis intercept, that is given by the sum of V_{fb} and $k_B T/e$.

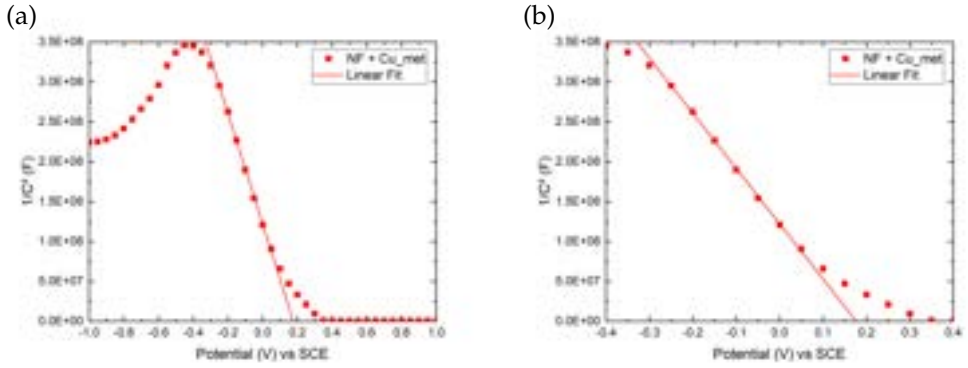

Figure 3.9: (a): Example of MS measurement on NF+*Cu_met* with the fit in the linear region. **(b)**: Zoom on the linear part.

From the linear part of the Mott Schottky plot is so possible to obtain the flat-band potential V_{fb} and from this, the band bending potential V_{bb} is given by subtracting the open-circuit potential V_{oc} [14]:

$$V_{bb} = V_{fb} - V_{oc} \tag{3.6}$$

The open-circuit potential V_{oc} is the potential at which the electrode immersed in the electrolyte reaches the electric equilibrium without applying any voltage.

For each electrode in this work, firstly the Open Circuit (OC) potential is measured and then the Mott Schottky analysis is conducted. Then CV, LSV and EIS analysis where conducted.

3.4 Electrochemical measurements of PLAL-NPs loaded onto Graphene Paper

Electrochemical measurements on GP-based electrodes report in general noisy behaviours. When electrodes are taken out the solution, the GP appear visibly more rough than it was before the usage, so contact with the water itself is enough to corrode the substrate. However some appreciable result are obtained.

3.4.1 Open Circuit and Mott Schottky

The first measurement conducted is the Open Circuit potential after some minutes of electrode immersion when the OC measured is constant for almost 10 seconds.

The second measurement conducted is the Mott Schottky and results are plotted in Figure 3.10. All the measured capacitance are roughly in the same range, expect for the mixed $Cu\_et + Ni\_met$ sample. This sample also present a double linear descendent zone. In the descendent linear zone, a linear fit is performed to obtain the x-intercept V_{fit} and so the flat band potential V_{fb} using Equation 3.5. The OC potential V_{oc} is used with the flat band potential V_{fb} to obtain the band bending using Equation 3.6 and all the values are reported in Table 3.2. Samples with Nickel (blue

and cyan lines) presents approximately the same intercept around $570mV$ while samples with Copper (red and green lines) and the bare GP (black line) presents approximately the same intercept around $1000mV$ indicating no significant changes. The mixed sample (cyan line) apparently has two linear zones, but only the second is considered because with this jump reaches the level of the other curves.

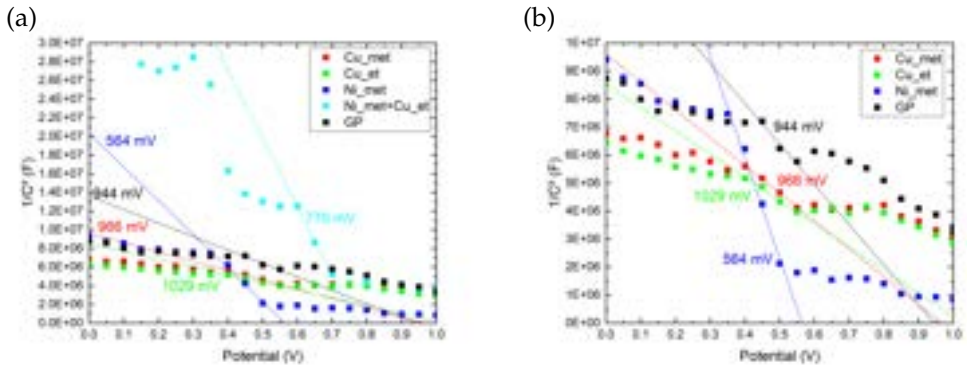

Figure 3.10: (a): Mott Schottky plot of GP samples with marked x-intercept. **(b)**: Plot without $Cu\_et + Ni\_met$ to better distinguish the other samples.

Sample	V_{OC} $[mV]$	V_{fit} $[mV]$	V_{bb} $[mV]$
GP	-213	944	1132
Cu_met	-201	966	1142
Cu_et	-183	1029	1208
Ni_met	-192	564	731
$Cu\_et + Ni\_met$	-213	770	958

Table 3.2: Summary of OC and MS measures on the GP-based electrodes. V_{OC} is the Open Circuit potential, V_{fit} is the x-intercept of the linear fit in the MS plot (Figure 3.10) and V_{bb} is the evaluated band bending potential.

No conversion between SCE and RHE was made. In fact this correction should be applied both on V_{oc} and V_{fb} and the subtraction (Equation 3.6) will cancel it.

3.4.2 Hydrogen Evolution Reaction measurements

3.4.2.1 Cyclic Voltammetry

For each sample at least 10 cycles between $0V$ and $-1.7V$ vs. SCE were performed. Each sample showed a slightly worsening in the first cycles and then tends to stabilize. The switching potential is chosen high enough to reach at least $10mA/cm^2$. The worsening trend is presented also with the bare substrate so it can be ascribed to GP affected by corrosion when the high negative potential is applied.

3.4.2.2 Linear Sweep Voltammetry

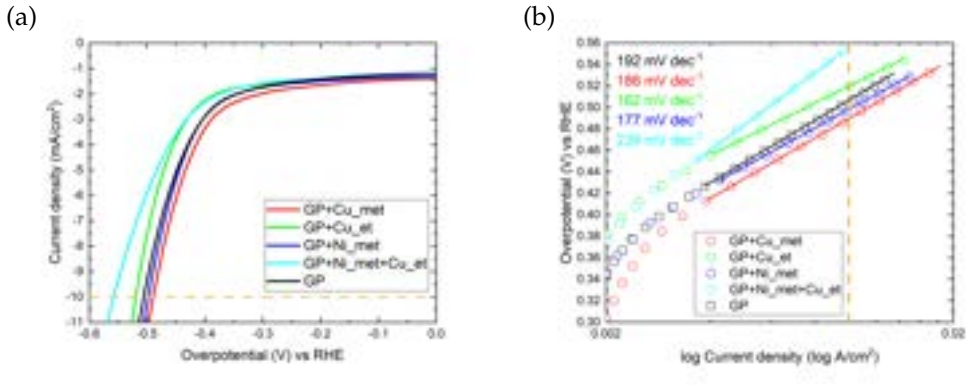

Figure 3.11: (a): LSV and **(b)**: Tafel plot of GP-based electrodes for HER in $1M$ KOH with marked Tafel slopes. Horizontal orange dashed line in (a) and vertical in (b) marks the current density of $10mA/cm^2$.

With LSV all electrodes are compared on the same applied voltage range and plotted in Figure 3.11. The conversion from SCE to RHE was conducted using Equation 3.2 with the uncompensated resistance R_u obtained from EIS. In Table 3.3 the results of overpotential (marked as η) vs RHE, Tafel slope and R_u from EIS are shown for each electrode. Only the sample with Cu_met and Ni_met NPs results in overpotential slightly lower than the bare substrate and the Tafel plot shows similar behaviour for these samples. Cu_et sample apparently starts its reaction at higher potential with respect to the other samples but then the current grows

rapidly as indicated from the lower Tafel slope. $Cu\_et + Ni\_met$ follows Cu_et at low potential an then behave worse than the other as indicated from the higher Tafel slope.

Sample	R_u $[\Omega]$	η vs RHE $[mV]$	Tafel slope $[mV/dec]$
GP	7.5	506	192
Cu_met	6.3	490	186
Cu_et	5.9	520	162
Ni_met	6.8	498	177
Cu_et+Ni_met	5.6	558	239

Table 3.3: Summary of LSV measures on GP-based electrodes for HER in $1M$ KOH.

3.4.2.3 Electrochemical Impedance Spectroscopy

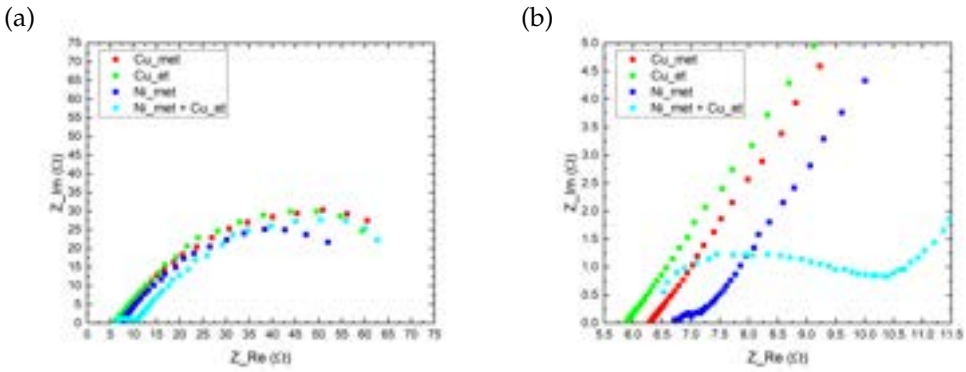

Figure 3.12: (a): EIS measurements on GP-based for HER in $1M$ KOH. **(b)**: Zoom on high frequency behaviour.

EIS measurements are plotted in Figure 3.12 and shows for all the samples the expected behaviour that recall a depressed semicircle. Only $Cu\_et + Ni\_met$ sample clearly shows the expect two semicircles. In the high frequency region (low real and imaginary impedance) a very small semicircle is also observed in the other samples. The values of resistance

and capacitance obtained by fitting the curves with the Armstrong and Henderson model using [11] are summarized in Table 3.4. The uncompensated resistance R_u shows slightly the same values for all the samples because the experimental setup is the same. Charge transfer resistance R_{ct} shows low values (less than 10Ω) for all the samples. This resistance is higher for Copper samples, in particular for *Cu_et* as expected from the presence of the thick layer of polymer. R_p shows very high values (up to $\sim 90\Omega$).

Sample	Potential vs SCE $[V]$	R_u $[\Omega]$	R_{ct} $[\Omega]$	R_p $[\Omega]$	C_{dl} $[F]$	α_{dl}	Q_p $[F]$	α_p
Cu_met	-1.44	6.3	3	92	0.006	0.7	0.006	0.7
Cu_et	-1.44	5.9	10	79	0.008	0.7	0.005	0.8
Ni_met	-1.45	6.8	1	84	0.002	0.7	0.001	0.7
Cu_et+Ni_met	-1.45	5.6	5	90	0.0004	0.6	0.01	0.7

Table 3.4: Summary of EIS measurements on GP-based electrodes for HER in $1M$ *KOH* fitted with [11].

3.4.3 Oxygen Evolution Reaction measurements

3.4.3.1 Cyclic Voltammetry

For each sample at least 10 cycles between $0V$ and $+0.7V$ vs. SCE were performed. Also in this case, each sample showed a slightly worsening (less than HER in the previous Section) in the first cycles and then tends to stabilize.

3.4.3.2 Linear Sweep Voltammetry

LSV curves are plotted in Figure 3.13 and summarized in Table 3.5, R_u is obtained from EIS (Table 3.6). All the samples, except for $Cu\_et + Ni\_met$, results in better performance with respect to the bare GP. Samples with Copper NPs show no significant improvement with respect to the bare substrate. *Ni_met* results to be the best sample with an overpotential $40mV$ lower than the substrate one and also the Tafel slope is slightly lower. The Tafel plot in Figure 3.13(b) shows the linear zone for all the

samples before the current of $10 mA/cm^2$. At higher current all the curves bend upward indicating that something starts to limit the processes.

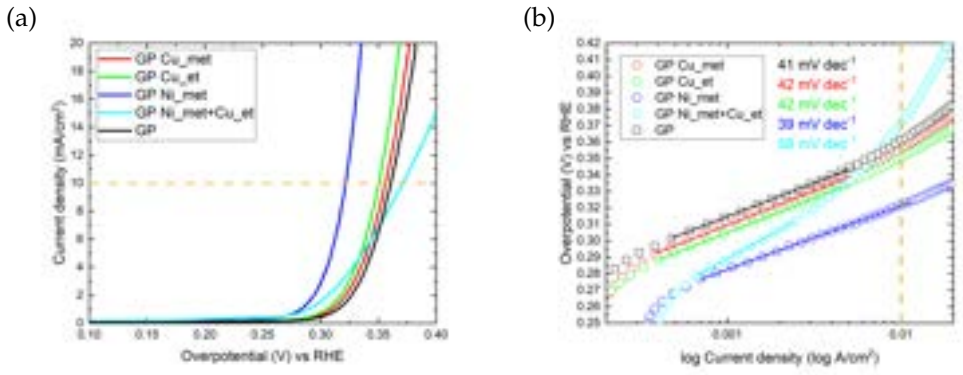

Figure 3.13: (a): LSV and **(b)**: Tafel plot of GP-based electrodes for OER in $1M$ *KOH* with marked Tafel slopes. Horizontal orange dashed line in (a) and vertical in (b) marks the current density of $10 mA/cm^2$.

Sample	R_u $[\Omega]$	η vs RHE $[mV]$	Tafel slope $[mV/dec]$
GP	4.5	361	41
Cu_met	6.6	356	42
Cu_et	6.1	350	42
Ni_met	5.9	321	39
Cu_et+Ni_met	5.8	371	58

Table 3.5: Summary of LSV measures on GP-based electrodes for OER in $1M$ *KOH*.

3.4.3.3 Electrochemical Impedance Spectroscopy

EIS measurements are plotted in Figure 3.14 and the results of fitting are summarized in Table 3.6. Also in this case only $Cu\_et + Ni\_met$ presents the two semicircles, but in the high frequency region (low impedance) a hinted semicircle is also observed in the other samples. As expected, R_u is slightly the same for all the samples. R_{ct} presents very low values (lower than HER) indicating a favored process except for $Cu\_et + Ni\_met$.

R_p presents higher values but still much lower than HER (Table 3.4). The highest R_p is referred to *Cu_et* while the lower one is referred to *Ni_met* which also has the best performance in LSV.

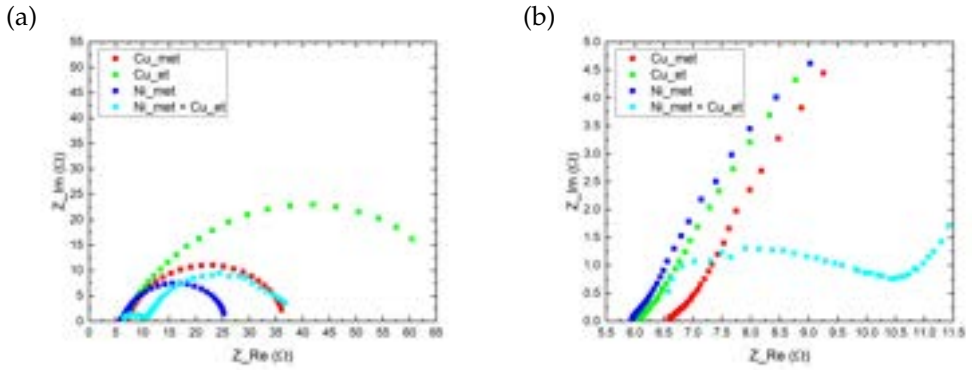

Figure 3.14: (a): EIS measures on GP-based electrodes for OER in 1*M KOH*. **(b)**: Zoom on high frequency behaviour.

Sample	Potential vs SCE $[V]$	R_u $[\Omega]$	R_{ct} $[\Omega]$	R_p $[\Omega]$	C_{dl} $[F]$	α_{dl}	Q_p $[F]$	α_p
Cu_met	0.47	6.6	0.7	30	0.001	0.8	0.004	0.8
Cu_et	0.45	6.1	0.7	71	0.002	0.8	0.007	0.7
Ni_met	0.45	5.9	0.7	20	0.002	1	0.007	0.8
Cu_et+Ni_met	0.45	5.8	5.0	28	0.0002	0.6	0.009	0.8

Table 3.6: Summary of EIS measures on GP-based electrodes for OER in 1*M KOH* fitted with [11].

3.5 Electrochemical measurements of PLAL-NPs loaded onto Nichel Foam

Electrochemical measurements on NF are in general more clean and smooth than on GP. After the various measurements the samples do not show clearly sign of corrosion. The high porosity of the substrate suggest in general higher performance than GP due mainly to the high exposed surface.

3.5.1 Open Circuit and Mott Schottky

The first measures conducted are OC and MS. Mott Schottky measurements are plotted in Figure 3.15 with all the curves that presents the same smooth trend and the linear fit have the intercept in approximately the same zone with no valuable differences for the Copper presence. In Table 3.2 data from OC and MS are presented together with the band bending obtained with Equation 3.6.

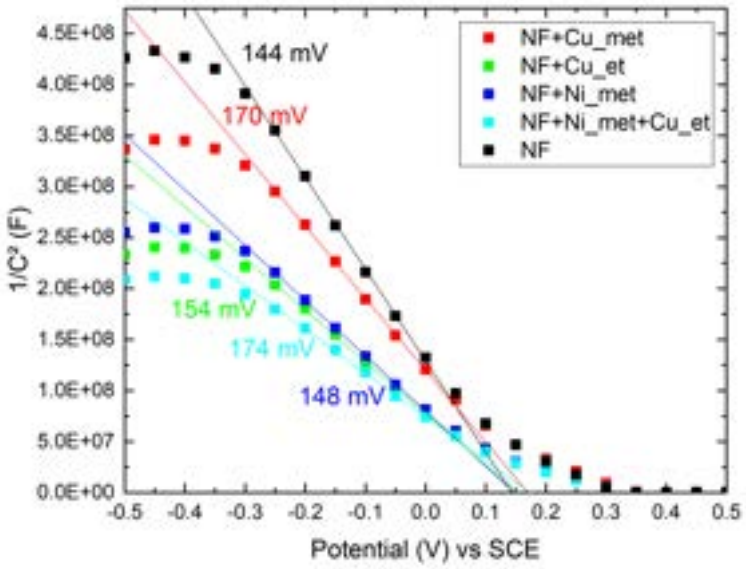

Figure 3.15: Mott Schottky plot of NF-based electrodes with marked x-intercept.

Sample	$V_{OC}\ [mV]$	$V_{fit}\ [mV]$	$V_{bb}\ [mV]$
NF	-429	144	548
Cu_met	-352	170	497
Cu_et	-320	154	481
Ni_met	-340	148	463
$Cu\_et + Ni\_met$	-361	174	510

Table 3.7: Summary of OC and MS measures on the NF-based electrodes. V_{OC} is the Open Circuit potential, V_{fit} is the x-intercept of the linear fit in the MS plot (Figure 3.15) and V_{bb} is the evaluated band bending potential.

3.5.2 Hydrogen Evolution Reaction measurements

3.5.2.1 Cyclic Voltammetry

For each sample at least 10 cycles between $0V$ and $-1.5V$ vs. SCE were performed. Each electrode showed a slightly improvement in the first cycles and then tends to stabilize.

3.5.2.2 Linear Sweep Voltammetry

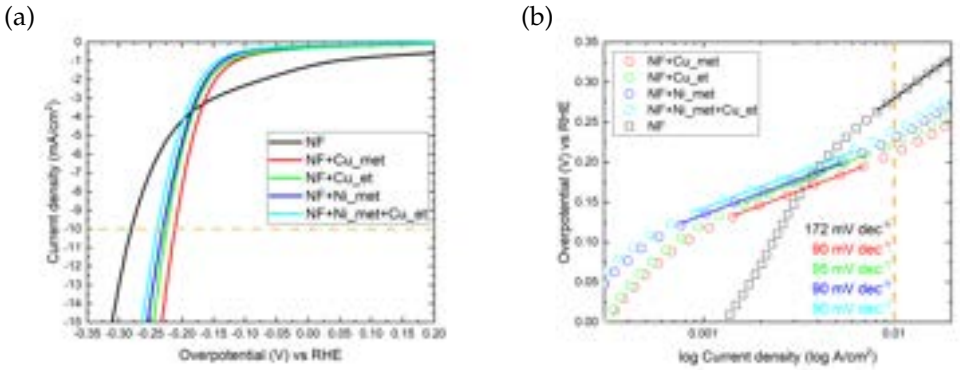

Figure 3.16: (a): Linear Sweep Voltammetry and **(b)**: Tafel plot of NF-based electrodes for HER in $1M\ KOH$ with marked Tafel slopes. Horizontal orange dashed line in (a) and vertical in (b) marks the current density of $10mA/cm^2$.

LSV measures are plotted in Figure 3.16 and summarized in Table 3.8, R_u is obtained from EIS (Table 3.9). All the samples results in better performance with respect to bare NF lowering the overpotential by $51mV$ ($Cu\_et + Ni\_met$) in the worst case and $68mV$ (Cu_met) in the best case. All the samples maintain slightly the same behaviour and have slightly the same Tafel slope and similar overpotential both much lower than the bare NF. The Tafel plot in Figure 3.16(b) shows the linear zone for all the samples at lower potential and current than the bare substrate, after the current of $10mA/cm^2$ the curves start bend upward. This significant difference between the substrate and the NP-loaded electrodes indicates that there is a strong catalytic activity due to the presence of NPs.

Sample	R_u $[\Omega]$	η vs RHE $[mV]$	Tafel slope $[mV/dec]$
NF	2.2	279	172
Cu_met	2.2	211	90
Cu_et	2.3	224	95
Ni_met	2.3	230	90
Cu_et+Ni_met	2.3	238	90

Table 3.8: Summary of LSV measurements on NF-based electrodes for HER in $1M\ KOH$.

3.5.2.3 Electrochemical Impedance Spectroscopy

EIS measurements are plotted in Figure 3.17 and the results of fitting are summarized in Table 3.9. The size of the semicircles recall the LSV behaviour of Figure 3.16: R_{ct} decreasing agrees with the overpotential decreasing. R_{ct} presents low values for the Copper samples and higher values for the Nickel and the mixed samples, while R_p is lower for the Nickel sample, a bit higher for the Copper samples and very high for the mixed sample. The plots apparently does not presents the double semicircle behaviour, also in the low impedance region, but with a deeper analysis all the points have a deviation from the main semicircle indicating the presence of the second smaller semicircle.

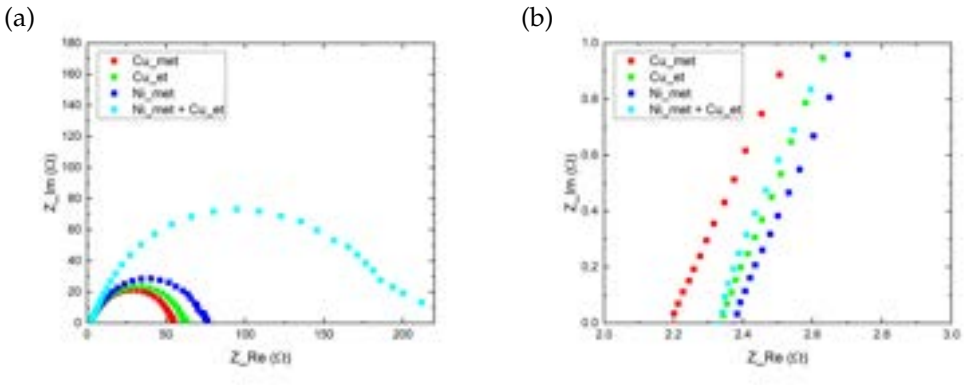

Figure 3.17: (a): EIS measurements on NF-based electrodes for HER in $1M\ KOH$. **(b)**: Zoom on high frequency behaviour.

Sample	Potential vs SCE $[V]$	$R_u\ [\Omega]$	$R_{ct}\ [\Omega]$	$R_p\ [\Omega]$	$C_{dl}\ [F]$	α_{dl}	$Q_p\ [F]$	α_p
Cu_met	-1.20	2.2	0.4	53	0.0008	0.8	1E-8	0.8
Cu_et	-1.20	2.3	0.3	60	0.0007	0.8	5E-6	0.8
Ni_met	-1.20	2.4	32	39	0.0006	0.8	0.0002	1
Cu_et+Ni_met	-1.15	2.3	46	146	0.0006	0.8	0.0001	1

Table 3.9: Summary of EIS measurements on NF-based electrodes for HER in $1M\ KOH$ fitted with [11].

3.5.3 Oxygen Evolution Reaction measures

3.5.3.1 Cyclic Voltammetry

For each sample at least 10 cycles between $0V$ and $+0.7V$ vs. SCE were performed. Each sample showed a slightly worsening in the first cycles and then tends to stabilize.

3.5.3.2 Linear Sweep Voltammetry

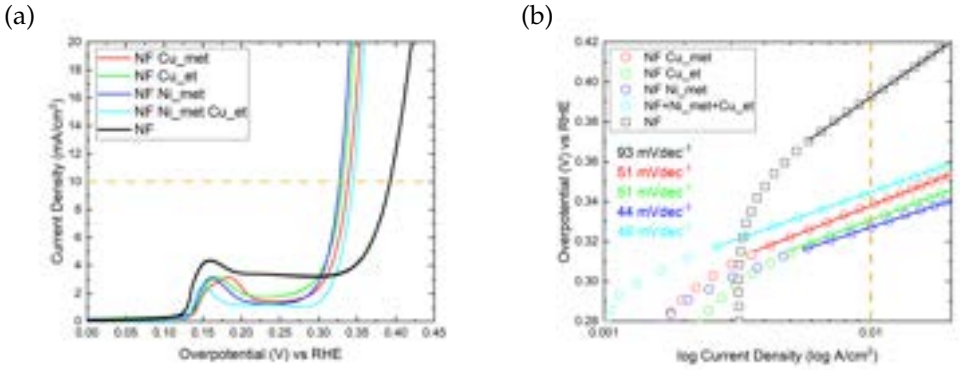

Figure 3.18: (a): LSV and **(b)**: Tafel plot of NF-based for OER in $1M\ KOH$with marked Tafel slopes. Horizontal orange dashed line in (a) and vertical in (b) marks the current density of $10mA/cm^2$.

LSV measurements are plotted in Figure 3.18 and the resuts of overpotential and Tafel slope are summarized in Table 3.10, R_u is obtained from EIS (Table 3.11). All the samples results in better performance with respect to bare NF substrate lowering the overpotential by $48mV$ $(Cu\_et + Ni\_met)$ in the worst case and $62mV$ (Ni_met) in the best case. All the samples maintain slightly the same behaviour and have slightly the same Tafel slope and similar overpotential both much lower than the bare NF. Figure 3.18(a) shows the Nickel oxidation peak due to the substrate for all the samples. The Tafel plot in Figure 3.18(b) shows the linear zone in the same current range for all the samples, but the bare substrates presents a bigger slope. These heavy differences between the substrate and the prepared samples indicate that there is a strong catalytic activity due to the presence of NPs.

Sample	R_u $[\Omega]$	η vs RHE $[mV]$	Tafel slope $[mV/dec]$
NF	2.4	393	93
Cu_met	2.8	338	51
Cu_et	2.3	331	51
Ni_met	2.3	327	44
Cu_et+Ni_met	2.2	345	48

Table 3.10: Summary of LSV measurements on NF-based electrodes for OER in 1*M KOH*.

3.5.3.3 Electrochemical Impedance Spectroscopy

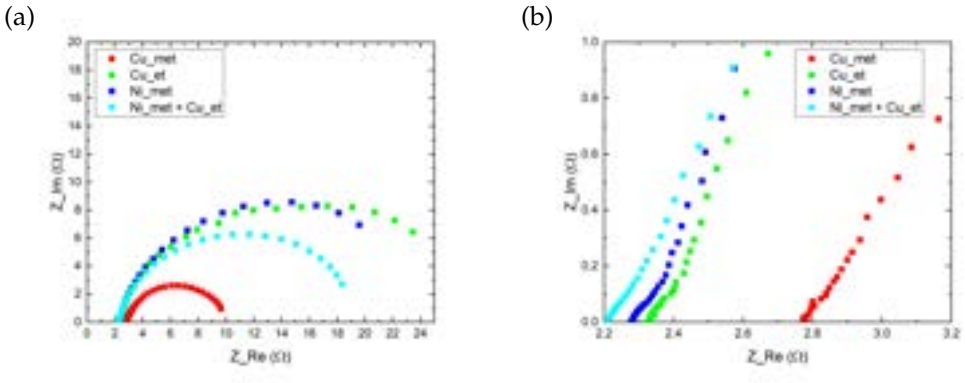

Figure 3.19: (a): EIS measurements on NF-based electrodes for OER in 1*M KOH*. **(b)**: Zoom on high frequency behaviour.

EIS measurements are plotted in Figure 3.19 and the results of fitting are summarized in Table 3.11. R_u and R_{ct} are slightly the same for all the samples while R_p presents big variations and higher values. The plots apparently does not presents the double semicircle behaviour, but in the low impedance region there is the clear evidence of a very small semicircle.

Sample	Potential vs SCE $[V]$	R_u $[\Omega]$	R_{ct} $[\Omega]$	R_p $[\Omega]$	C_{dl} $[F]$	α_{dl}	Q_p $[F]$	α_p
Cu_met	0.48	2.8	0.7	7	0.03	0.7	0.004	1
Cu_et	0.45	2.3	0.3	24	0.03	0.8	0.004	1
Ni_met	0.45	2.3	0.4	23	0.03	0.8	0.006	1
Cu_et+Ni_met	0.47	2.2	0.2	17	0.002	1	0.02	0.8

Table 3.11: Summary of EIS measurements on NF-based electrodes for OER in 1*M KOH* fitted with [11].

3.6 Understanding the electrochemical data

In this Section, a qualitatively data interpretation and modeling is proposed. From now on, the samples $Cu\_et + Ni\_met$ will be indicated as "mix".

3.6.1 Relation between electrochemical parameters

As seen in Sections 3.4.1 and 3.5.1, both GP-based and NF-based electrodes have a positive band banding resulting in accumulation of positive charges on the surface. All the NPs are metallic (Section 2.5) and so are positively charged as the substrate surface. This charge accumulation should interfere with the absorption of H^+ ions. So the reaction will start at higher applied potential and consequently the overpotential (for now on marked as η) will increase. So an ***Hypothesis*** is proposed: **Lower band bending** implies **lower overpotential** in HER.

Instead the relation between Tafel slope and the total resistance $R_{ct} + R_p$ is given by: $\frac{1}{R_{ct}+R_p} = \frac{\partial i}{\partial V} = nF\frac{\partial k}{\partial V}$ using the notation of Section 1.2.1 where k is the reaction rate, F is the Faraday constant and n is the number of electron involved.The quantity $\partial i/\partial V$ reported in log scale is Tafel slope [10], so follows that **lower total resistance** implies **lower Tafel slope**.

Table 3.12 collects the data from the previous Sections of this Chapter and tries to show some correlations between the data. *Ni_met* on GP presents the lowest band bending and a low overpotential as expected and both low Tafel slope and total resistance. *Cu_met* on NF presents

both the lowest Tafel slope and total resistance and also the lowest overpotential, but a high band bending (*Ni_met* has the lowest).

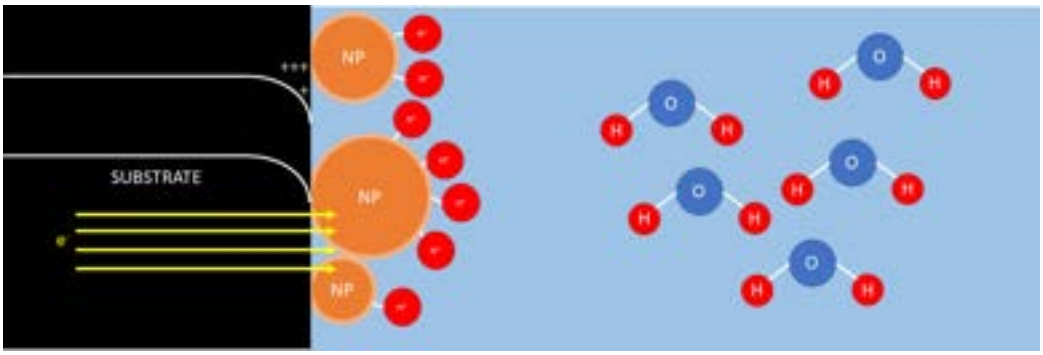

Figure 3.20: Scheme of band bending and H^+ adsorption on NPs during the Hydrogen Evolution Reaction.

Sample	V_{bb} $[mV]$	η $[mV]$	Tafel slope $[mV/dec]$	R_{ct} $[\Omega]$	$R_{ct}+R_p$ $[\Omega]$
Section	3.4.1	3.4.2.2		3.4.2.3	
GP	1132	506	192		
Cu_met	1142	490	186	3	95
Cu_et	1208	520	162	10	89
Ni_met	731	498	177	0.8	85
mix	761;958	558	239	5	95
Section	3.5.1	3.5.2.2		3.5.2.3	
NF	548	279	172		
Cu_met	497	211	90	0.4	53
Cu_et	481	224	95	0.3	60
Ni_met	463	230	90	32	71
mix	510	238	90	46	192

Table 3.12: Summary of HER measurements in $1M$ *KOH* on GP-based and NF-based electrodes. Marked blue values represents the lowest values in the column, marked red values represents the highest values in the column.

Unfortunately, no specific correlation appears between the band bending and the overpotential from the data concerning the same substrate.

Focusing on the bare substrate instead, GP presents higher band bending and so the higher accumulated positive charge and so higher overpotential with respect to NF and the Hypothesis is confirmed.

The correlation between the resistance and the Tafel slope is evident within the variations due to the choice of potential. In fact the potential chosen to perform EIS measurements (as discussed in Section 3.3.3) is the onset potential, while in this case the measurement should be made at the same potential. The NF-mixed electrode is a clear example: LSV in Figure 3.11 at low overpotential recall the *Cu_et* curve and so the resistance values obtained from EIS in Table 3.12 are similar, but at high overpotential the mixed sample grows slowly (higher Tafel slope).

OER measurements are summarized in Table 3.13 and the previous consideration on total resistance and Tafel slope are valid.

Following the reasoning previously discussed, a higher positive charge accumulation should encourage the OH^- absorption and so the reaction, but the data of the NPs electrodes shows the opposite trends. But focusing on the bare substrate instead, GP presents higher band bending and so the higher accumulated positive charge and so lower overpotential with respect to NF (Figure 3.22) and also in this case the reasoning runs.

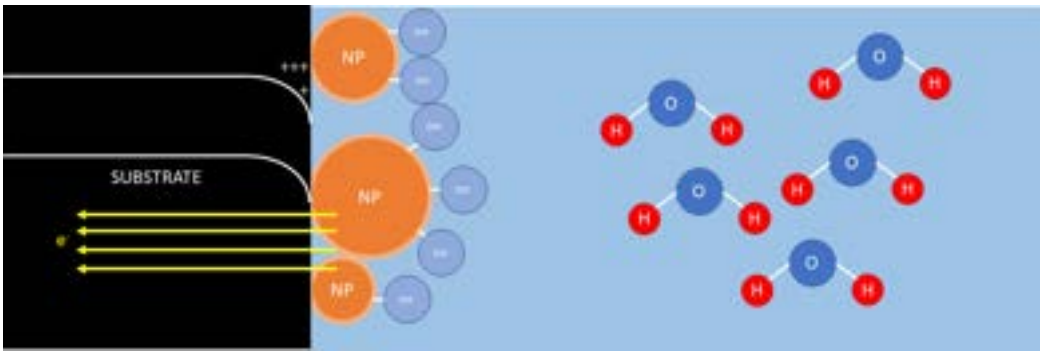

Figure 3.21: Scheme of band bending and OH^- adsorption on NPs during the Oxygen Evolution Reaction.

Sample	V_{bb} $[mV]$	η $[mV]$	Tafel slope $[mV/dec]$	R_{ct} $[\Omega]$	$R_{ct}+R_p$ $[\Omega]$
Section	3.4.1	3.4.3.2		3.4.3.3	
GP	1132	361	41		
Cu_met	1142	356	42	0.7	31
Cu_et	1208	350	42	0.7	72
Ni_met	731	321	39	0.7	21
mix	761;958	371	58	5	33
Section	3.5.1	3.5.3.2		3.5.3.3	
NF	548	393	93		
Cu_met	497	338	51	0.7	8
Cu_et	481	331	51	0.3	24
Ni_met	463	327	44	0.4	23
mix	510	345	48	0.2	17

Table 3.13: Summary of OER measurements in $1M\ KOH$ on GP-based and NF-based electrodes. Marked blue values represents the lowest values in the column (highest band bending), marked red values represents the highest values in the column (lowest band bending).

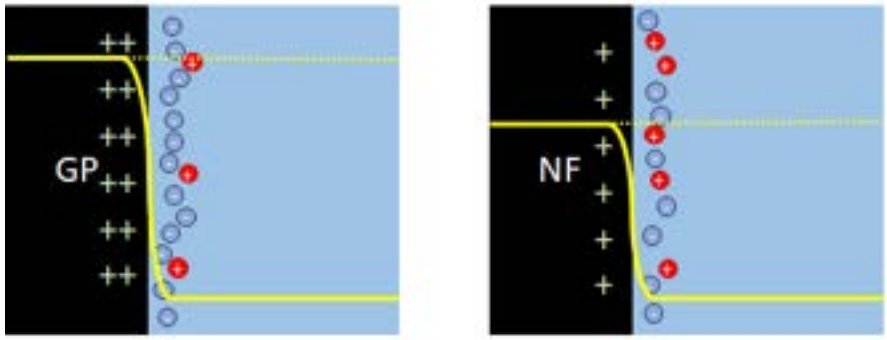

Figure 3.22: Schematic representation of the charge accumulation at the equilibrium between two different substrate (black) and the liquid (light blue) depending on the indicated band bending.

3.6.2 Band bending and overpotential

To clarify the relation between the band bending and overpotential with the presence of the catalytic NPs, what happen to the bands inside the substrate, the NP and the liquid should be investigated. SEM images shows that the substrate is mostly exposed to the liquid (as seen in Figure 3.3) so the ***Hypothesis*** is that band bending (and the consequently voltage steps) between the liquid and the substrate remains unaltered with or without the NPs. Giving this value as fixed, the presence of the NPs produce a different measured band bending due to the energetic levels inside the particle, so the voltage step between the NPs clusters and the substrate can be evaluated by a simple subtraction. The schematic representation of the various electrodes with evaluated voltage steps and band bending is given in Figures 3.23 for GP and 3.24 for NF.

The bare substrate with the liquid acts like discussed in Section 1.2.1 starting from the Nernst Equation and so on, but for the other samples there is the presence of an intermediate step given by the interaction between the substrate and metallic NPs. The next ***Hypothesis*** is that the junction between the substrate and the NP is supposed to acts like a Schottky diode [15].

The following interpretations does not work for the $Cu\_et + Ni\_met$ maybe because there are two type of separate particles and the system maybe act like a double Schottky diode. This is only a further ***Hypothesis*** that only a specific study can prove or deny.

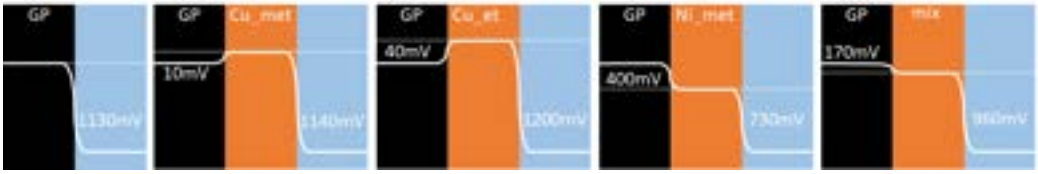

Figure 3.23: Band scheme of the GP-based electrodes with marked approximated voltage steps (not in scale).

For the NF electrodes (Figure 3.24) the junction presents the substrate as p-type with respect to the particle so in OER the junction is forward biased while in HER the junction is reverse biased (Figure 3.25). In fact the highest voltage step (between substrate and catalyst) correspond with

the lowest overpotential in OER (*Ni_met*) and the lowest voltage step (between substrate and catalyst) correspond with the lowest overpotential in HER (*Cu_met*).

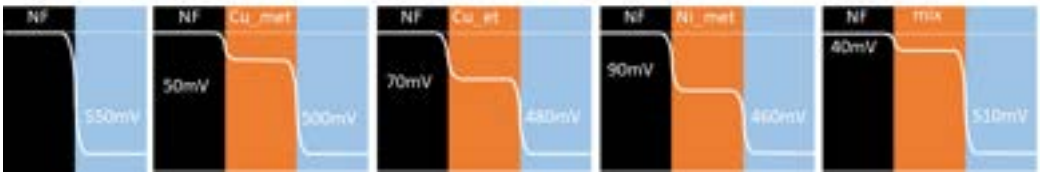

Figure 3.24: Band scheme of the NF-based electrodes with marked approximated voltage steps (not in scale).

For the GP electrode (Figure 3.23) the situation is the same (p-n junction) for *Ni_met*, but opposite (n-p junction) for *Cu_met* and *Cu_et* because of the inverted voltage step. In *Ni_met* the junction is forward biased in OER in fact it has the lowest overpotential. In HER the junction is forward biased for *Cu_met* and *Cu_et*, so the highest voltage step is supposed to bring the lowest overpotential, but the complete system (substrate-NP-liquid) in this case act like a trap for electrons, so the lesser voltage step (*Cu_met*) brings to the lowest overpotential.

This oversimplified model gives a qualitatively result that is in according with the experimental data. In order to make previsions is necessary a theoretical study to evaluate in advantage the voltage steps between the substrate and the NP. A starting point can be the work function: $\phi_{Copper} = 4.7eV < \phi_{Carbon} = 4.81eV < \phi_{Nickel} = 5.01eV$ [16] that recall the inverse of the energetic levels in the schemes. Copper and Carbon have similar values so explain the low voltage step, Nickel presents a higher value and so the steps are increased. But the NPs has not the same work function of the bulk material due to their small size, the presence of the polymer and the interaction with the electrolyte, this could explain the high difference between the Nickel substrate and the Nickel NPs dropped on the Nickel substrate.

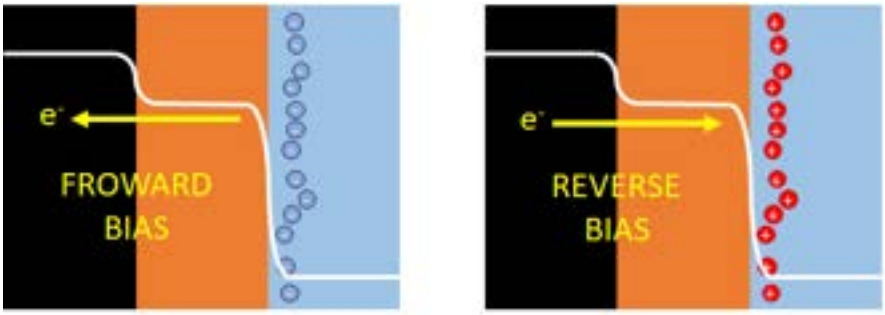

Figure 3.25: Schematic representation of the junction between the substrate (black) and the NP (orange), with marked forward or reverse bias depending on the current direction.

3.7 Summary and comparison

Substrate	NPs	Catalyst loading $[\mu g/cm^2]$	HER $\eta[mV]$	Tafel slope $[mV/dec]$	OER $\eta[mV]$	Tafel slope $[mV/dec]$
GP	*Cu_met*	0.8	490	186	356	42
GP	*Cu_et*	1.1	520	162	350	42
GP	*Ni_met*	0.7	498	177	321	39
GP	mix	0.9	558	239	371	59
NF	*Cu_met*	0.8	211	90	338	51
NF	*Cu_et*	1.1	224	95	331	51
NF	*Ni_met*	0.7	230	90	327	44
NF	mix	0.9	238	90	345	48

Table 3.14: Summary of the obtained results including **Catalyst loading**, **Overpotential** vs RHE and **Tafel slope** for HER and OER in $1M\ KOH$ aqueous ambient.

All the results obtained in this Chapter involving water splitting are summarized in Table 3.14. The first important result is the low amount of catalyst ($\sim 1\mu g$) that makes these values comparable with those of the state of the art (Tables 1.2, 1.3, 1.4 and 1.5) [17]. The produced electrodes obtained

good results in HER only for NF as substrate, but a bit far away from the state of the art while in OER the overpotential is comparable with the state of the art for both the substrates. Figure 3.26(a) clearly shows two group of data for NF and GP in HER, but Figure 3.26(b) shows only a group of data. In both Figures the data found in this work lie in the high part of the graph indicating a very low amount of used catalyst.

Another important result obtained in this Chapter is the model that relates the overpotential with the band bending considering first the substrate-liquid (Figure 3.22) and then substrate-NP-liquid interaction (Figure 3.25), but still more studies should be conducted to find a theoretical model and to experimental understand if this was a fortunate case or this model can be applied to all materials.

Some comparison with electrodes produced by classical way (sputtering and dewetting) was also conducted and reported in appendix H.

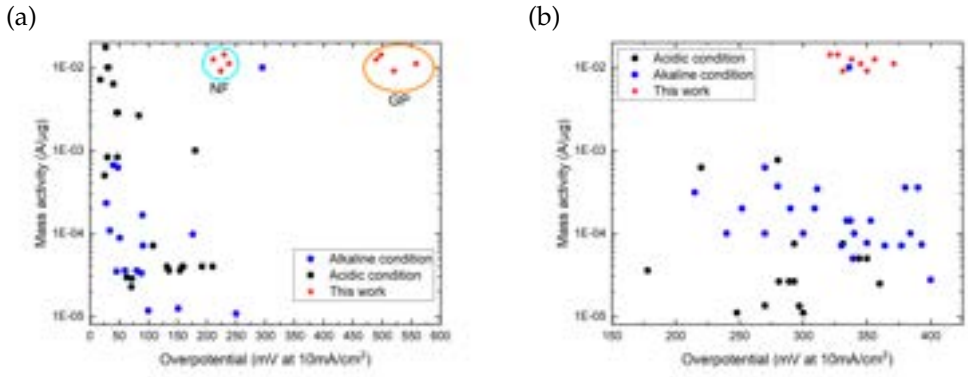

Figure 3.26: (a): Literature data for HER from Table 1.2 [17] with added data from this work. Two groups of data are presents indicating the NF-based and the GP-based electrodes. **(b)**: Literature data for OER from Table 1.3 [17] with added data from this work. Mass activity is evaluated from Catalyst Loading with Equation 1.22.

Bibliography

[1] Boiling point of gases, liquids and solids. https://www.americanelements.com/boiling-point.html.

[2] Rump - genplot. http://www.genplot.com/.

[3] Versastudio software. https://www.ameteksi.com/products/software/versastudio-software.

[4] Noémie Elgrishi, Kelley J. Rountree, Brian D. McCarthy, Eric S. Rountree, Thomas T. Eisenhart, and Jillian L. Dempsey. A practical beginner's guide to cyclic voltammetry. *Journal of Chemical Education*, 95(2):197–206, November 2017. doi:10.1021/acs.jchemed.7b00361.

[5] Lucas-Alexandre Stern and Xile Hu. Enhanced oxygen evolution activity by niox and ni(oh)2nanoparticles. *Faraday Discuss.*, 176:363–379, 2014. doi:10.1039/c4fd00120f.

[6] J. Ambrose, R.G. Barradas, and D.W. Shoesmith. Investigations of copper in aqueous alkaline solutions by cyclic voltammetry. *Journal of Electroanalytical Chemistry and Interfacial Electrochemistry*, 47(1):47–64, September 1973. doi:10.1016/s0022-0728(73)80344-4.

[7] S. Anantharaj, S. R. Ede, K. Karthick, S. Sam Sankar, K. Sangeetha, P. E. Karthik, and Subrata Kundu. Precision and correctness in the evaluation of electrocatalytic water splitting: revisiting activity parameters with a critical assessment. *Energy & Environmental Science*, 11(4):744–771, 2018. doi:10.1039/c7ee03457a.

[8] Shangshang Wang, Jianbo Zhang, Oumaïma Gharbi, Vincent Vivier, Ming Gao, and Mark E. Orazem. Electrochemical impedance spectroscopy. *Nature Reviews Methods Primers*, 1(1), June 2021. doi:10.1038/s43586-021-00039-w.

[9] Sengeni Anantharaj and Suguru Noda. Appropriate use of electrochemical impedance spectroscopy in water splitting electrocatalysis. *ChemElectroChem*, 7(10):2297–2308, May 2020. doi:10.1002/celc.202000515.

[10] N Krstajić, M Popović, B Grgur, M Vojnović, and D Šepa. On the kinetics of the hydrogen evolution reaction on nickel in alkaline solution. *Journal of Electroanalytical Chemistry*, 512(1-2):16–26, October 2001. doi:10.1016/s0022-0728(01)00590-3.

[11] Eis spectrum analyzer. http://www.abc.chemistry.bsu.by/vi/analyser/.

[12] K. Gelderman, L. Lee, and S. W. Donne. Flat-band potential of a semiconductor: Using the mott–schottky equation. *Journal of Chemical Education*, 84(4):685, April 2007. doi:10.1021/ed084p685.

[13] Kevin Sivula. Mott–schottky analysis of photoelectrodes: Sanity checks are needed. *ACS Energy Letters*, 6(7):2549–2551, July 2021. doi:10.1021/acsenergylett.1c01245.

[14] Luca Bruno, Sergio Battiato, Mario Scuderi, Francesco Priolo, Antonio Terrasi, and Salvo Mirabella. Physical insights into alkaline overall water splitting with NiO microflowers electrodes with ultralow amount of pt catalyst. *International Journal of Hydrogen Energy*, 47(80):33988–33998, September 2022. doi:10.1016/j.ijhydene.2022.08.005.

[15] Bernard Sapoval and Claudine Hermann. *Physics of semiconductors*. Springer, New York, NY, 1995 edition, December 1994.

[16] Work functions for photoelectric effect. http://hyperphysics.phy-astr.gsu.edu/hbase/Tables/photoelec.html.

[17] Jakob Kibsgaard and Ib Chorkendorff. Considerations for the scaling-up of water splitting catalysts. *Nature Energy*, 4(6):430–433, May 2019. doi:10.1038/s41560-019-0407-1.

Conclusions

Brief summary

The aim of this work was to find and study a low cost and non pollutant electrocatalysts with valuable performances for both HER and OER using nanostructures and fabricated in a simple and cheap way.

PLAL technique was used to synthetize Copper and Nickel NPs in Methanol and Ethanol. UV-Vis-NIR optical measurements (Section 2.3.1) shows the typical plasmonic peaks of Copper and Nickel. Optical simulation (Section 2.4.2) indicate a very large amount of small particles and a very few amount of bigger ones. SEM images (Section 2.3.2) showed particles of circular shape, while TEM images (Section 2.3.3) showed smaller crystalline particles with radius in the order of few nanometers. Interplanar distances and diffraction pattern indicated metallic nature of Copper NPs. XRD (Section 2.3.4) reveled a metallic crystalline nature of Cu and Ni and XPS (Section 2.3.5) showed Cu and Ni peaks with a chemical shift indicating the presence some surface compounds. EDX-TEM indicated Carbon and Oxygen all around the NPs. All the analysis conducted indicated the presence of a polymer all around the particle that preserve and protect the NPs and their crystalline metallic structure (Section 2.4.1). The polymer also explained the difference between the size distribution observed between SEM and TEM: big particles with radius in the order of $100nm$ are agglomeration of small particles that optically respond almost as metal particles (Section 2.4.2).

The electrodes were prepared by drop casting $60\mu l$ of NPs solution

on the substrate (GP and NF). SEM images (Section 3.1.2) show NPs uniformly distributed on the substrate and RBS (Section 3.1.1) indicates the presence of about $\sim 1\mu g$ of deposited material. Electrochemical measurements are conducted in $1M\ KOH$ solution. Measurements on GP-based electrodes (Section 3.4) indicates good performance in OER with an evident catalytic activity, but a not good performance in HER with little variability between the measures. Measurements on NF-based electrodes (Section 3.5) indicates good performance and evident catalytic activity both in OER and HER. Comparison with literature (Section 3.7) shows that some result are not distant from the state of the art. Furthermore a simplistic model (Section 3.6.2) is proposed to understand the obtained results and find some correlation between band bending and overpotential.

Most relevant results

The first relevant results are the values of overpotential and catalyst loading found for the produced electrodes that respond to the aim of this work. The results reported in Section 3.7 are comparable with the state of the art as shown in Figure 3.26. In fact, the found values lies in the top part of the graph (indicating high mass activity). In HER only the NF-based electrodes report good results because the substrate itself presents high porosity and enhance the catalyst effect. In OER all the electrodes report good results.

The second relevant result is the presence of polymer around the particles discussed in Section 2.4.1. This was an unexpected results that came from the high energies involved during the PLAL process. The big particles and clusters in SEM images (in Section 2.3.2 and 3.1.2) are nothing but sphere of polymer with embedded metal particles which make the polymer conductive. This conductive polymer may be seen as a problem because of their poor conductive properties, but in this case can see as an advantage because the polymer protect the metal particles from oxidation and corrosion during the electrochemical processes and preserve so the metallic nature and cristallinity of the NPs.

The third relevant result is the model discussed in Section 3.6.2. This model is still to simplistic, but explain the differences in the obtained overpotential and start to make prediction based on the measured band bending.

Perspectives

Based on the obtained results, there are many possible perspectives for future studies:

1. The use of the NPs on a variety of substrate and at different coverage to study and investigate how this affect the electrochemical parameters. Also maintaining the same catalyst amount, a large comparison between particles of different material or produced in different ways (an example is reported in Appendix H).

2. The study of the conductive polymer properties (electron transport, optical properties, work function, . . .) and also the relation between the target, the laser beam energy and the solvent. From the actual data Ethanol lead to a thicker polymer than Methanol, so solvent with longer Carbon chains should lead to the formation of much more polymer.

3. The further evaluation of the model proposed in Section 3.6.2 that focus on the similitude between the band bending at the liquid-electrode interface and the Schottky junction. Maybe this study can lay the foundation of a theoretical model that connect the electronic properties of the electrode (first of the substrate, then with the adding of NPs) to the Evolution Reactions behaviours. Another study can bu executed on the interaction between the substrate and the NPs without the presence of the liquid to study the involved phenomena.

4. The effects of NPs of different materials on the same substrate. In this work the mixed sample produced the worst performance. A study should be conducted to find out how this particles mix together and how this affect the various properties.

5. The study on the possibility of use the produced NPs as photoelectrocatalyst for the water splitting reaction.

6. The further study on optical simulation using a numerical model for non spherical shapes and that involves clusters.

Thanks for the reading.

Acknowledgements

Thanks to the Supervisor and the Co-Supervisor.
Thanks to the managers of the used laboratories and instruments in this work (in order of usage):

- Dr. G. Franzò - Access to all CNR-IMM labs at DFA
- Prof. F. Ruffino - Laser `Quanta-Ray PRO-Series Nd:YAG` - DFA
- Prof. A. Terrasi - `Varian Cary 500` Spectrophotometer - DFA
- Dr. V. Strano - SEM `Zeiss Supra25 FE-SEM` - DFA/CNR-IMM
- Dr. S. Scalese - SEM `Zeiss Supra35 FE-SEM` - CNR-IMM
- Dr. S. Boninelli - TEM `JEOL ARM200F` - CNR-IMM
- Prof. G. Malandrino - XRD `Rigaku, Smartlab` - BRIT
- Prof. G. Condorelli - XPS `PHI 5000 VersaProbe II` - BRIT
- Prof. S. Mirabella and S. Tatì - RBS - DFA/CNR-IMM
- Prof. S. Mirabella - `VersaSTAT 4` potentiostat and NanoSPES lab - DFA
- Prof. F. Ruffino and Prof. A. Terrasi - Sputter `Emitech K550X` - DFA

Appendices

Appendix A

Laser

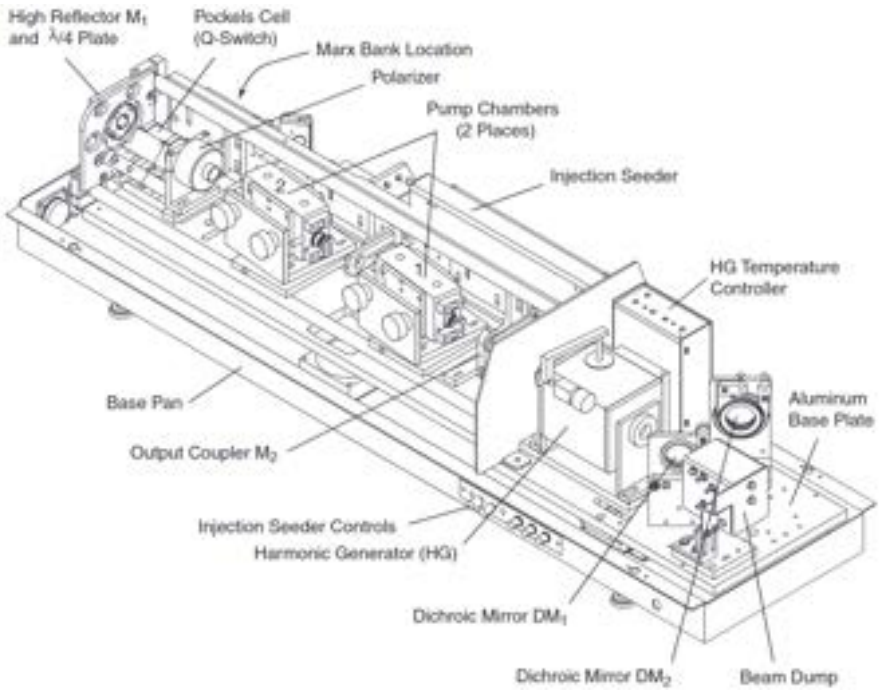

Figure A.1: Quanta-Ray PRO-Series Nd:YAG internal scheme [1].

The laser used in this work is a `Quanta-Ray PRO-Series Nd:YAG` [1]. The laser scheme is presented in Figure A.1.

A.1 Laser structure and parameters

Lasers are made up by a resonant cavity in which lies an active media that amplifies light whenever pass trough it. The cavity is delimited by two mirrors, one is high reflective and the other one is partially reflective (in Figure A.1 respectively M_1 and M_2). The partially reflective mirrors usually have about $\sim 10\%$ transmission [2]. Due to interference only some photonic modes are allowed inside the cavity and are equally spaced in frequency ν:

$$\Delta\nu = \frac{c}{2L} \tag{A.1}$$

whit c speed of light and L cavity length. The active media is a three or four levels system in which population inversion is guaranteed. Between the two electronic levels among which we want lasing, electrons should stay in the upper level so, whenever a photon arrives another photon is created by stimulated emission. Now electrons are in the lower levels and must be carried away. The upper level is usually a metastable state whit decay time of about $\sim ns$, the others level are short-lived whit decay time of about $\sim fs$ so electron goes away rapidly. An external pumping provides electrons to be promoted in upper levels that rapidly decay in the metastable one waiting for lasing. Amplification gain γ is defined as the ratio between output photon flux ϕ_{out} and input photon flux ϕ_{in} and depends on the frequency ν

$$\gamma(\nu) = \frac{\phi_{out}}{\phi_{in}} = \frac{\gamma_0(\nu)}{1 + \phi_{in}/\phi_s(\nu)} = \frac{N_0\sigma(\nu)}{1 + \phi_{in}/\phi_s(\nu)} \tag{A.2}$$

where γ_0 is the initial gain and depends on the initial population inversion N_0 and the cross section $\sigma(\nu)$ that as a lorentian shape and ϕ_s is a saturation flux. When $\phi_{in} = \phi_s$ population inversion is half of the initial one [2].

In the specific case of our laser, cavity modes have a $200MHz$ spacing and the active media gain has a $30GHz$ linewidth (Figure A.2).

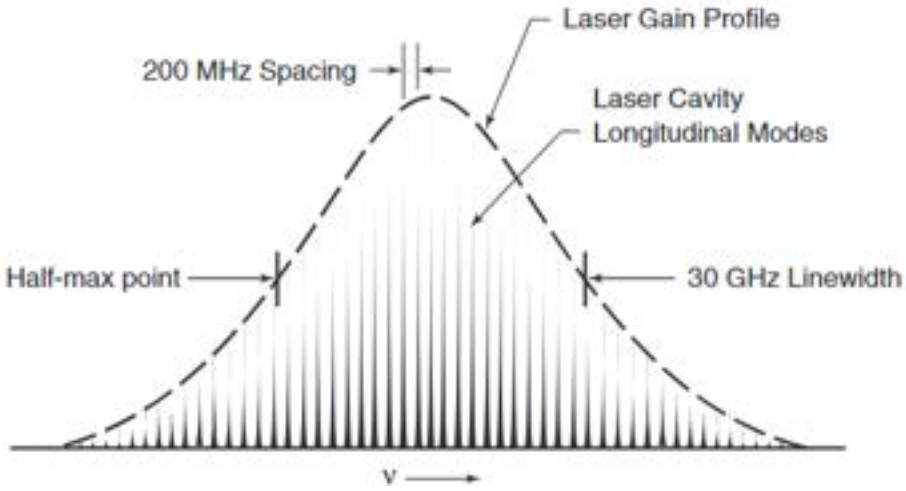

Figure A.2: Gain linewidth and cavity frequency spacing [1].

Our laser has two Nd:YAG active media. Nd:YAG is Yttrium Garnet ($Y_3Al_5O_{12}$) doped with Nd^{3+} ions. Neodymium ions provide a lot of energy levels to make lasing as shown in Figure A.3. In particular electrons are pumped in higher levels (marked as pumping bands) and then decay rapidly in level ${}^4F_{3/2}$. Then the laser transition occurs at $1064nm$.

Inside the cavity there is also an electric controlled Q-switch that provide $10ns$ pulses. Max frequency (pulses per second) allowed is $10Hz$, but lesser ones can be produced.

Outside the cavity there is an harmonic generator that provide second harmonic generation at $532nm$ (green light). Then the two beam lines are splitted and go out the laser separately.

A digital calorimeter is used to measure beam energy and provides values of about $\sim 500mJ$ per pulse. This correspond to a peak power of

$$P = 500 \cdot 10^{-3} J / 10 \cdot 10^{-9} s = 50MW \tag{A.3}$$

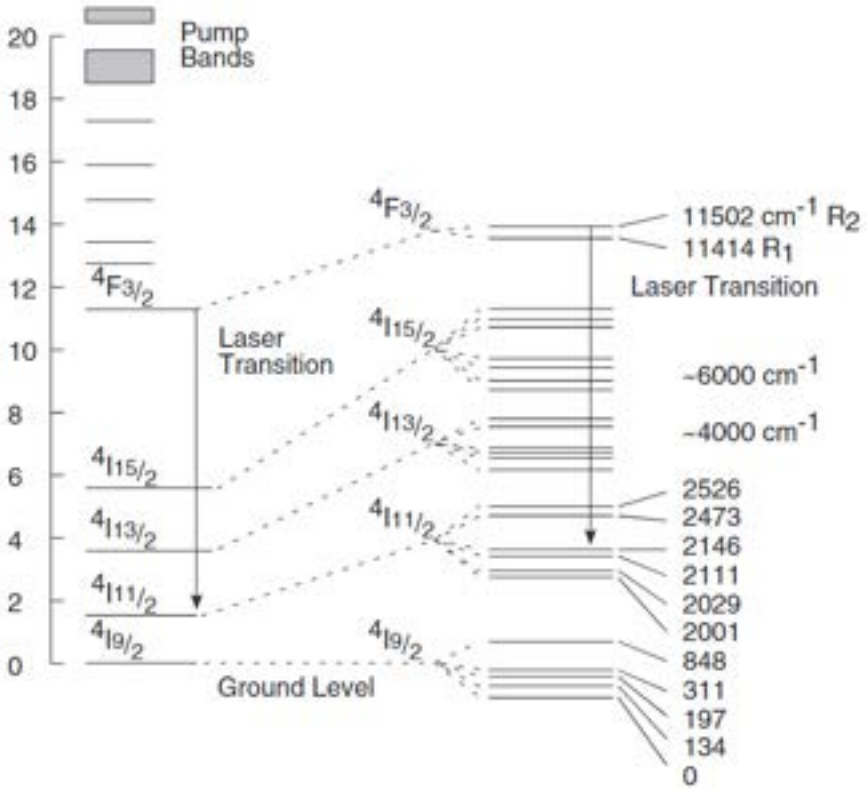

Figure A.3: Neodymium levels in Nd:YAG, 1064*nm* laser transition marked with an arrow [1].

Appendix B

UV-Vis-NIR Spectrophotometry

UV-Vis-NIR Spectrophotometry is based on the interaction between a sample and a monocromatic electromagnetic wave in the range between UV and near Infra Red. With this technique is possible to measure the fraction on light scatterd, absorbed and transmitted by the sample at different wavelengths. Wavelength λ is related to photon energy E trough this relation:

$$E = \frac{hc}{\lambda} \approx \frac{1239[eV \cdot nm]}{\lambda[nm]} \tag{B.1}$$

where h is the Plank constant and c is the speed of light.

B.1 Spectrophotometer

The spectrophotometer is an instrument that can perform UV-Vis-NIR Spectrophotometry. In this work `Varian Cary 500 Spectrophotometer` is used.
Spectrophotometers are made up by different parts:

- Lamps: provide an high intensity spectrum at different wavelengths. Usually an halogen lamp covers the Visible and near Infrared spectrum and a Deuterium lamp covers the ultraviolet spectrum. A rotating mirror can select the required lamp.

- Monocromator: receives in input lamp light and provides in output a monocromatic beam light. Is made up by some filters, an input slit, an output slit and a rotating grating. All these parts are electronically controlled to provide the required wavelength.
- Beam splitter: the beam light is divided in two identical beams. Is made by a mirror partially covered with reflective material.
- Sample holder: One of the beam passes trough the sample that can be a solid object, but also a solution. Different configuration involving mirrors can provide transmission measures or reflection measures.
- Detectors: one of the beams reaches directly the detector and acts like a reference I_0. The beam that passed trough the sample reaches another detector I_s.

If the light passes trough the sample, transmission measure is obtained by the ratio: [3]

$$T = \frac{I_0}{I_s} \tag{B.2}$$

and is usually expressed in percentage. If the light is reflected by the sample, reflection measure is obtained by the ratio:

$$R = \frac{I_0}{I_s} \tag{B.3}$$

and is usually expressed in percentage. A different kind of detector called integrating sphere can provide a measure of total reflection and scattering using Equation B.3. If scattering and emission rates are low, an absorbance measure can be obtained from the transmission one. In fact $R + A + T = 1$ where T is the transmission, R the reflection, A the absorbance. Other phenomena like emission are negligible. In general absorbance is expressed as the logarithm of the inverse of transmission:

$$A = log\left(\frac{1}{T}\right) \tag{B.4}$$

For colloidal solution the absorbance is related to concentration of the absorbing species via the Beer-Lambert law:

$$A = dN\sigma \tag{B.5}$$

where d is the optical path inside the solution, N is the absorber concentration (numeric density) and σ is the absorption cross section.

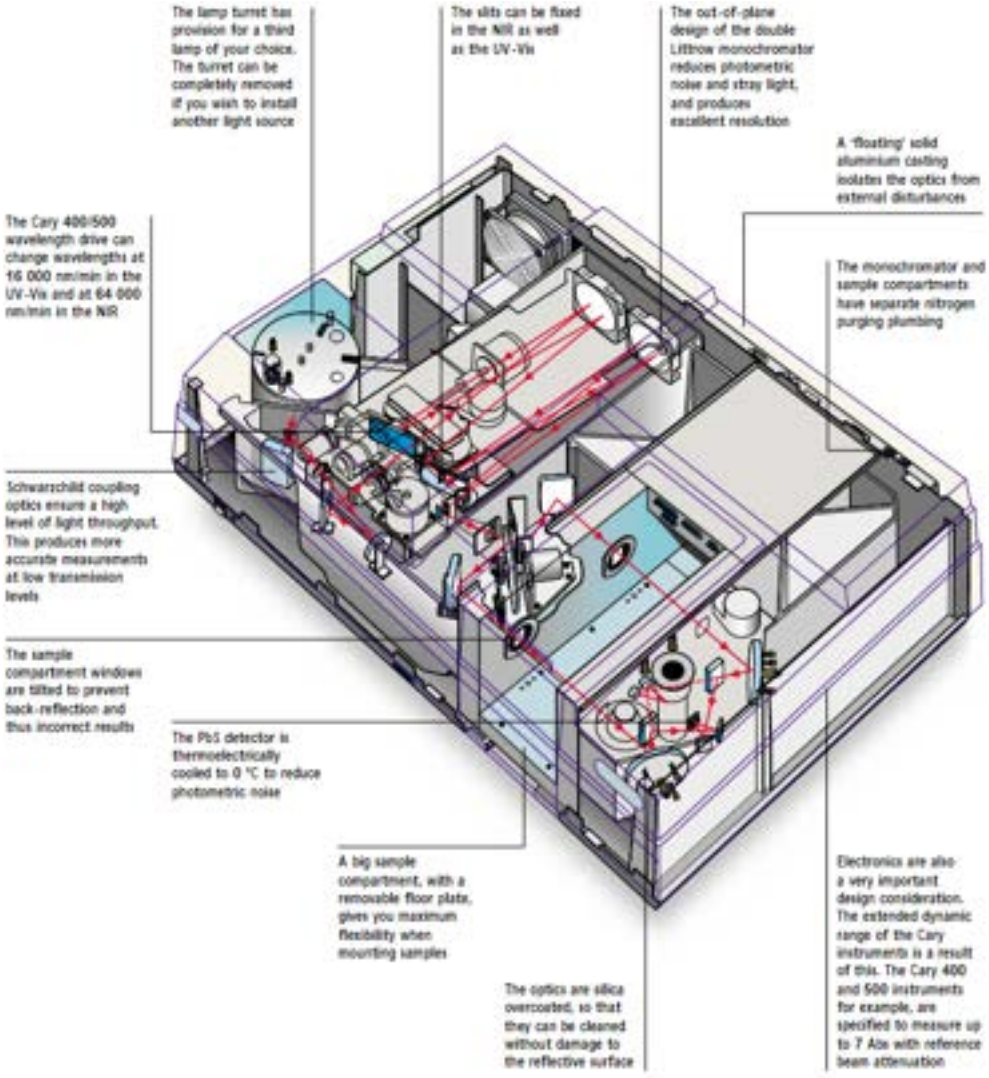

Figure B.1: Varian Cary 500 Spectrophotometers scheme [4].

Appendix C

Scanning Electron Microscopy

Figure C.1: Used SEM with EDX module.

Scanning Electron Microscopy (SEM) is a technique involving a microscope that uses the interaction of an electronic beam with a sample to

reconstruct an image of this with nanometric resolution.

In this work a `Zeiss Supra25 FE-SEM` and a `Zeiss Supra35 FE-SEM` were used.

C.1 SEM working principle

The use of electrons instead of light is an advantage because wavelength is much smaller. This bring higher magnification and depth of field.

By definition, the resolution (or resolving power) is the minimum distance between two object in order to be distinguishable. So two objects are distinguishable if their distance Δx is:

$$\Delta x \geq 0.61 \frac{\lambda}{N.A.} \tag{C.1}$$

This is the Rayleigh criterion, λ is electron wavelength, $N.A.$ is the numeric aperture (a parameter that is related to the maximum angle at which signal can be detected), 0.61 is a parameter that depends on the diffraction pattern of a single slit. For visible light, maximum resolution is about $\sim 200nm$, some SEM could reach $\sim 3nm$.

For electrons all depend on the wavelength. Electron wavelength comes from De Broglie relation $\lambda = h/p$ where h is the Plank constant and p is the momentum that depends on the electron velocity, the velocity depends on the acceleration voltage V [5]:

$$\lambda = \frac{h}{p} = \frac{h}{\sqrt{2mqV}} \tag{C.2}$$

where m is the electron mass and q is the electron charge. With a potential of about some kV, λ is the order of magnitude of the nm, that's good because also interatomic distances are in the order of nm. In theory this works, but the interaction volume of the electrons inside the sample is larger than the beam spot (especially for materials made up by light atoms), so scattering events are affected by a broadening of the original focused electron beam within the sample.

C.2 SEM structure

The SEM is made up by different parts:

- Electron gun: An hot filament or a tip emit electrons for thermionic effect or field effect. Then some rings provides positive voltage (in range $10 - 12kV$) to extract electron and create an electron beam of a precise energy. This system require ultra high vacuum.
- Magnetic lens: a first magnetic system decrease the beam diameter also with a single slit to increase resolution, a second magnetic system with another slit focus the beam on the sample.
- Scanning system: two couples of magnetic coils move the beam along `X` and `Y` direction to scan different points of the sample. Not all the sample is scanned, but only a portion. The magnification M is defined as the rate between image dimension and sample dimension.

Once electrons interact with the sample, some detectors gives information about the sample:

- Back Scattered electrons: A solid state detector is placed near the electron beam. It works using a p-n junction and provides information about the electrons scattered at angle near the beam.
- Secondary electrons: a Faraday cage (called collector) can collect both scattered electrons and secondary electrons if it works at negative potential, only scattered if it works at positive potential. Collected electrons reach a scintillator where a light signal is produced and reachs a photomultiplier that converts this in an electric signal. Different position can be chosen for this detector: out-lens collects secondary electrons from all the target, in-lens collects secondary electrons only from a region near the beam spot.

These detectors gives morphological information about the sample structure and produces grey-scales images where the brighter zones correspond to heavy atoms (high probability of scattering), but the brightness is also affected by morphology. Top part of a structure will result

brighter than the bottom part and then the substrate below. The detector position can cause a shadowing effect: the sample surface exposed to detector will result brighter than the one on the other side, is like watching the sample from a side. This happen with nanostrucutred samples and rough substrate and can be avoided using in-lens collector, like watching the sample from the top.

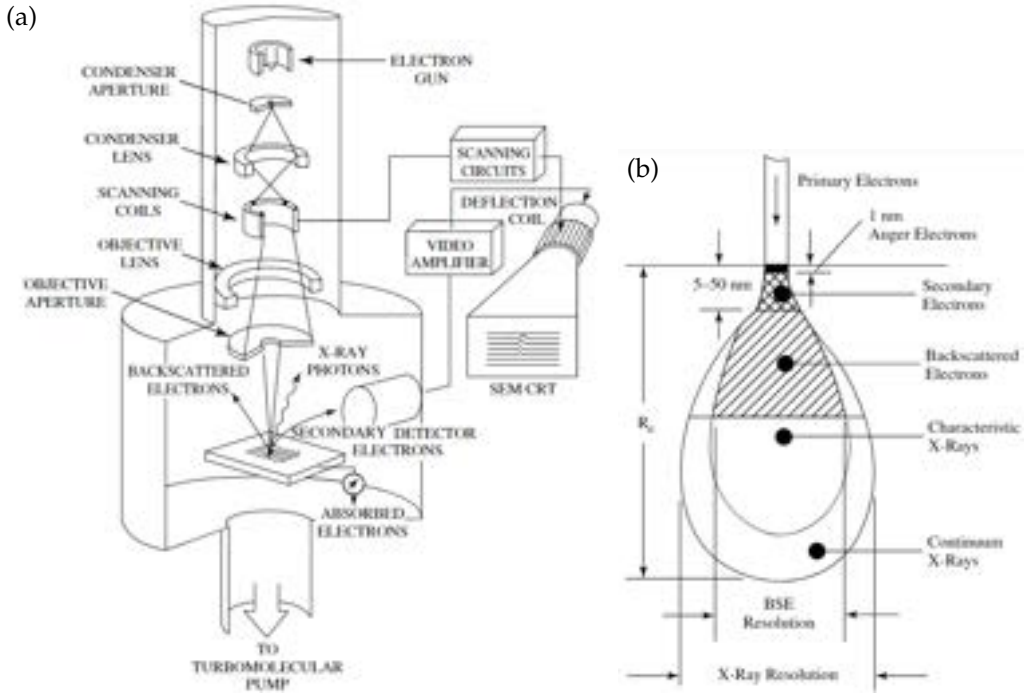

Figure C.2: (a): SEM structure [5]. **(b)**: Summary of the range and spatial resolution of backscattered electrons, secondary electrons, X-rays, and Auger electrons for electrons incident on a solid. [5].

C.3 Energy Dispersive X-Ray

Another detector can analyze X-rays produced by the electron beam interaction with the sample. This is called Energy Dispersive X-Ray (EDX) or Energy Dispersive X-Ray Spectrometer (EDS) [6, 7].

When a high energy electron interacts with an atom of the sample, a possible result is the ejection of an electron from a inner shell. The atom is

left in excited state and relax through a limited set of allowed transitions of outer shell electron filling the inner-shell vacancy. This relaxation process could lead to the emission of a X-Ray photon or an Auger electron. Every element as a characteristic X-Ray emission, so focusing the electron beam on a small sample region is possible to obtain compositional information and eventually create an element map.

The detector is a Silicon doped with Lithium p-i-n junction. A Berilium windows prevents low energy photon (compared to X-Rays) to enter the detector. When an X-Ray interacts with a Silicon atom, an electron is emitted with an energy $h\nu - E_c$ (the X-Ray energy minus the binding energy) and this photoelectron travels inside the detector producing electron-holes pair (every pair requires $3.96eV$ to be formed). So the total current depends on the incident energy. Also Auger electrons can create electron-holes pairs and Silicon atoms can emit other X-Rays that can be reabsorbed. To prevent electronic noise, the detector must be cooled with liquid nitrogen.

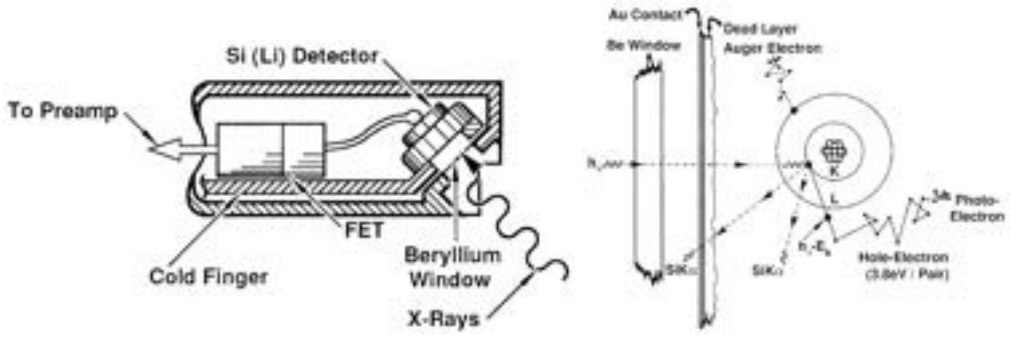

Figure C.3: EDX detector structure and detection process scheme [7].

Appendix D

Transmission Electron Microscopy

Transmission Electron Microscopy (TEM) is a microscopic technique that can obtain the maximum possible resolution for imaging a sample [8]. Like a SEM, it use the interaction between electrons and the sample, but in transmission, so electrons travel inside the sample interacting with it, Equations C.1 and C.2 are valid. Best machines has $N.A. \approx 0.01$ and $\lambda \approx 0.004nm$ with an accelerating voltage of $V \approx 100kV$, this bring to a resolution of $\sim 0.25nm$, compatible with atomic dimension.

Electrons are created with an electron gun and accelerated with a voltage in range $100 - 400kV$. Some condenser lens focus the beam on the sample in a few μm spot. The sample is placed on a small Copper or Carbon grid with large holes and must be thin (at least few hundreds of nm). Elsewhere electrons will be heavily scattered or absorbed by the sample or by the grid. After the interaction with the sample, electrons are focused with other lens on a fluorescent screen. Forward scattered electrons forms a diffraction pattern that give structural information. Bright-field images are formed only with transmitted electrons, dark-field images are formed with a specific diffracted beam. This operating mode is called parallel beam. High resolution TEM is able to give information on the atomic structure of the sample by showing single atomic lines.

Scanning Transmission Electron Microscopy (STEM) uses a fine electron beam $\approx 0.1nm$ (atomic size) to raster the sample and the software reconstructs the image point by point. This operating mode is called convergent beam and some scanning coil similar to the SEM ones are used. In

this case the electrons interact with the sample producing X-Rays and lost some energy, but still cross the sample. Spectroscopy can be performed both on X-Rays using EDX and on electrons using Electron Energy Loss Spectroscopy (EELS). Both of this technique are used to perform chemical analysis and combined with the scanning system can provides chemical map of the sample.

Selected Area Diffraction (SAD) is obtained focusing the beam in a specific zone. The interaction between the electrons and the crystal creates a diffraction pattern that can be detected and used to identify crystallinity and crystal planes.

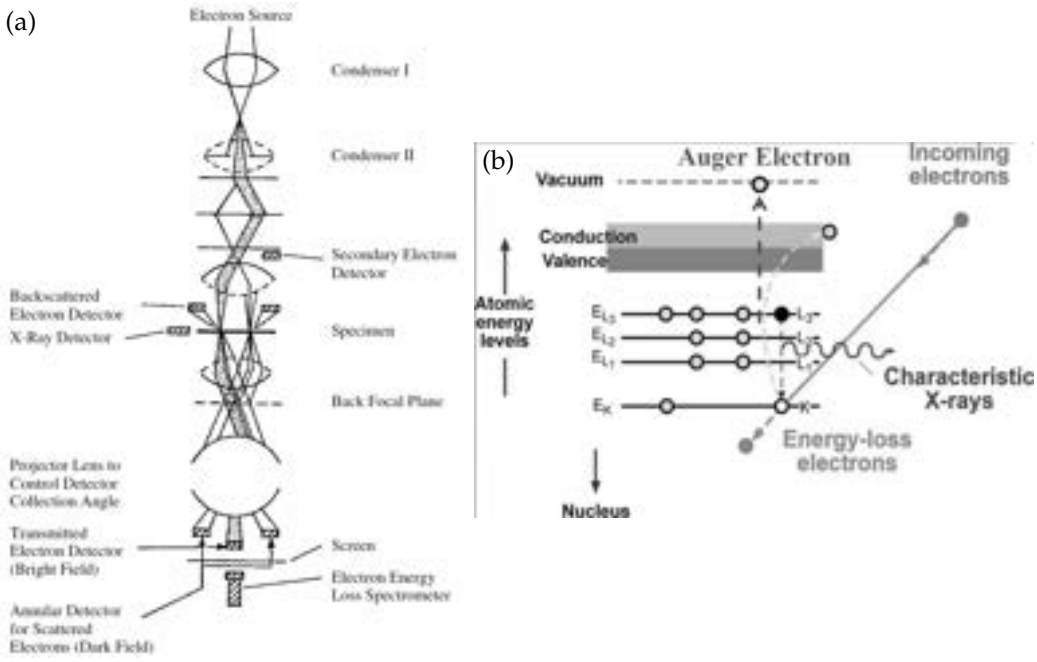

Figure D.1: (a): TEM structure [5]. **(b)**: Scheme of the process involving the electrons and the sample [9].

In this work the machine `JEOL ARM200F` [10] was used. It is equipped with a spherical aberration corrector on the electrons probe so as to ensure a spatial resolution below the Angstrom in scanning transmission electron microscopy (S/TEM), even at very low energy, and in the energy range between $200KeV$ and $40KeV$. This microscope is able to analyse

2D materials. The instrument is equipped with three digital cameras, 2k x 2k, for wide angle diffraction, high resolution TEM and 5 STEM detectors for atomic resolution STEM analyses. It is also able of performing tomographic analysis of nano-structured materials in both TEM that STEM mode. The instrument is also equipped with a last generation of monocromated electron energy loss spectrometer (EELS) and a large angle SDD-EDS X-ray detector ($0.98 str$), able to work simultaneously and acquire up to $1500 spectra/sec$ in joint fast EELS / EDX mode.

Figure D.2: JEOL ARM200F [10].

Appendix E

Rutherford Back Scattering Spectrometry

Rutherford Backscattering Spectrometry (RBS) is a non destructive surface analysis useful to evaluate thickness and composition of thin films.

Usually He^+ ions are sent to the sample with few MeV energy. Analyzing the energy of the backscatterd ions is possible to understand the mass of the surface element and also the depth distribution in few μm [5, 8].

Incident ions lose their energy while interacting with the sample electrons, but few of them succeed to make an elastic scattering with an atom nucleus and come back to the detector. The scattering event may happen on the surface or in depth, in this case the ion lose energy, scatter and then lose again energy until it reaches the surfaces and travel free toward the detector. An important parameter is the kinematic factor K defined as the ratio between the backscattering energy E_1 and the initial energy E_0:

$$K = \frac{E_1}{E_0} = \left(\frac{\sqrt{1 - (Rsin\theta)^2} + Rcos\theta}{1 + R} \right)^2 \qquad R = \frac{M_1}{M_2} \tag{E.1}$$

where R is the mass ratio between projectile M_1 and target M_2 and θ is the scattering angle. For heavy element in the target ($M_2 > M_1 \rightarrow R \ll 1$)

and high angles ($\theta \sim 180^{\circ}$), relation E.1 simplifies in:

$$K \approx 1 - \frac{2R(1 - cos\theta)}{(1+R)^2} \tag{E.2}$$

But also interaction with the sample produces energy loss, so the total energy E_t for a ion that backscatter at depth t is:

$$E_t = (E_0 - \Delta E_{in})K - \Delta E_{out} \tag{E.3}$$

where ΔE_{in} and ΔE_{out} are the loss inside the target before and after the scattering and depends on the depth t:

$$\Delta E_{in} K - \Delta E_{out} = [S]t \tag{E.4}$$

where $[S]$ is the backscattering energy loss factor and it is tabulated for pure elements target.

The backscattering yield (the counts of backscatterd ions) is given by

$$Y = \sigma \Omega Q N \tag{E.5}$$

where Ω is the solid angle of the detector, σ is the Rutherford cross section of the elastic scattering, Q is the total number of incident ions and N is the numerical surface density of target atoms. The total number of incident ions Q can be evaluated by the total charge of the scattering chamber. The Rutherford cross section is:

$$\frac{d\sigma(\theta)}{d\theta} = \left(\frac{Z_1 Z_2 e^2}{4E_{in}}\right)^2 \frac{1}{sin^4\theta/2} \tag{E.6}$$

Typical RBS spectrum does not shows peaks but bands well defined in energy. The higher energy of the band is given by ions scattered by the surface atoms and give information about the element mass of the target. The lower energy is given by the ions backscattered deep in the target and gives information about the thickness of the layer. The counts integrated between this two energies gives information about the atoms density. With this technique also composite layers can be analyzed.

For the analysis in this work a particles accelerator provided $2MeV$ Helium ions He^+. The scattering chamber was provided with high vacuum. Inside the chamber there is a carousel with different samples, an

electric controlled goniometer and the detector (solid state p-n junction silicon detector) placed at 15° with respect to the incident beam. The analysis to extract atoms density and composition are conducted with the software RUMP [11].

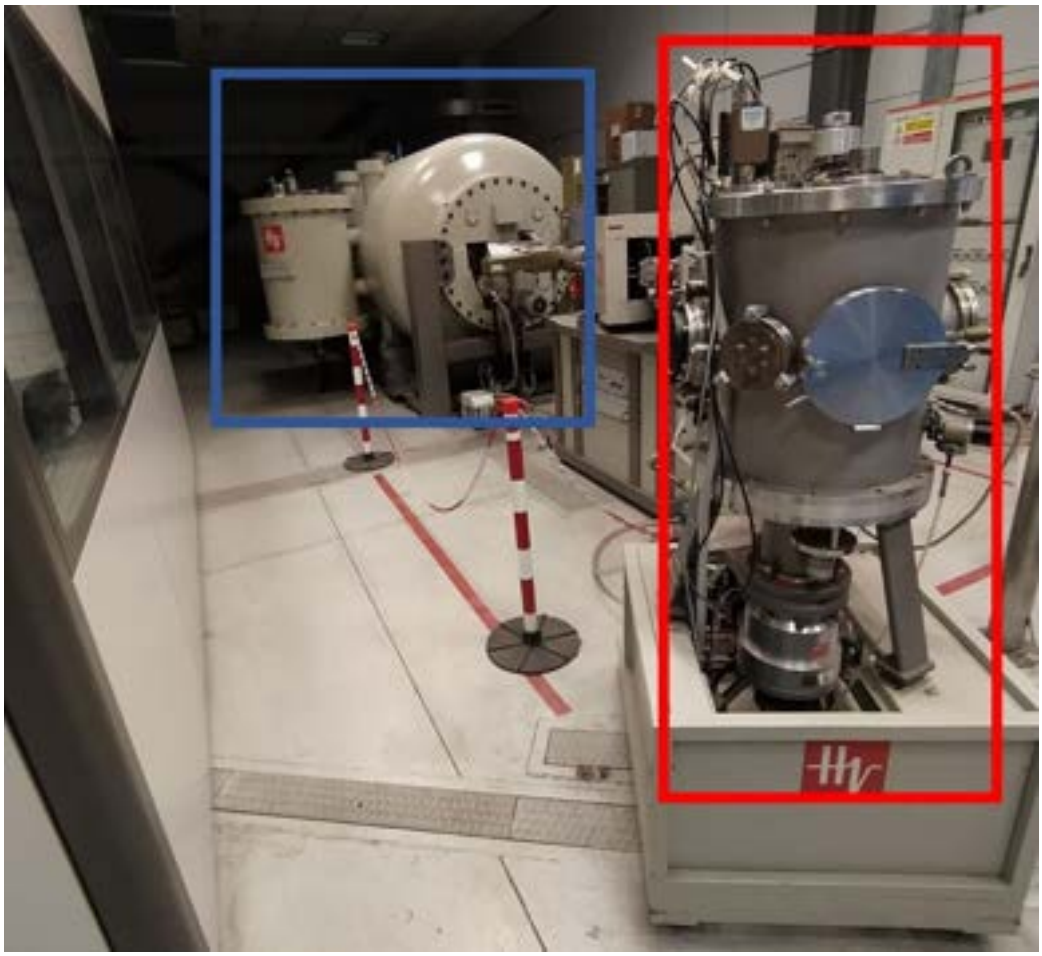

Figure E.1: Used RBS apparatus. Blue box: the ion accelerator. Red box: the detection chamber

Appendix F

X-Ray Diffraction

X-Ray Diffraction (XRD) is a technique that uses the diffraction of high energy photons to study the crystal nature of a sample [8, 12].

Everything works because X-rays are mirror reflected by crystal planes of the sample so the angle of the incoming wave will be equal to the one of the outgoing wave. Both initial and scattered waves will be on the same plane. Photons can interact with different crystal planes and after the reflection they have traveled different paths. So interference phenomena occurs (Bragg law):

$$n\lambda = 2d_{hkl}sin\theta \tag{F.1}$$

where λ is the photons wavelength, d_{hkl} is the distance between two parallel plans of Miller index (h,k,l) and θ is the angle for constructive interference. So depending on the order n an interference peak should be found at the angle θ.

d_{hkl} is related to the lattice parameter a for every crystal structure, for example for cubic crystal:

$$d_{hkl} = \frac{a}{\sqrt{h^2+k^2+l^2}} \tag{F.2}$$

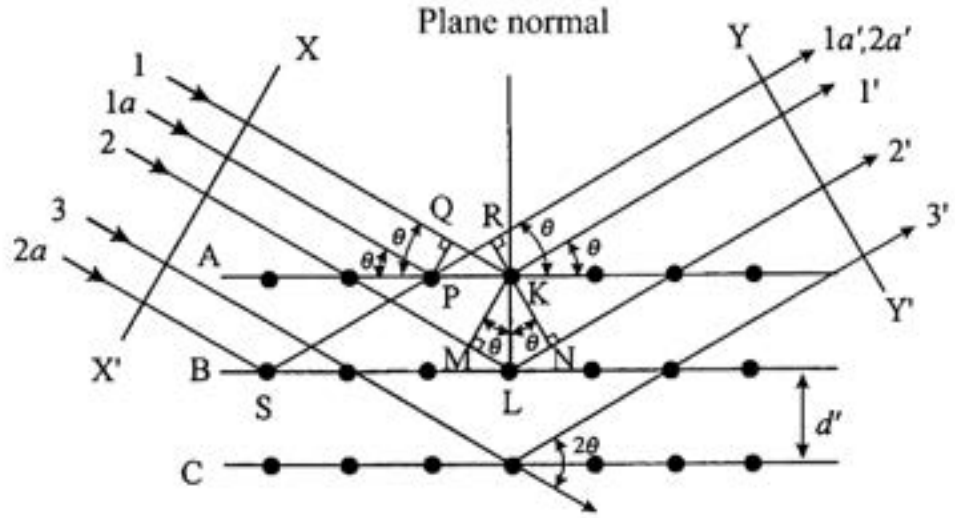

Figure F.1: Schematic diagram of diffraction of X-rays by a crystal (Bragg condition) [12].

XRD machines are made up by two rotating arms that revolve vertically around the sample holder. One harm holds the X-rays, on the other there's the X-rays detector. Usually the source is fixed at grazing angle with the sample while the detector spin around. The software will produce a graph called diffractogram where the double of the angle 2θ and the count are presented. Both solid samples and powders can be analyzed and no vacuum is required because X-Rays travels free in air.

Using XRD is possible to find first of all if the sample is crystalline. If it is amorphous, a broad hump will span all over the diffractogram, although a crystal sample produces sharp peaks. By comparing these peaks with those tabulated in the databases is possible to find the composition of the sample. Also if the sample is polycrystaline, the Scherrer formula relate the medium dimension τ to the peak FWHM β:

$$\tau = \frac{K\lambda}{\beta cos\theta} \tag{F.3}$$

where λ is the X-rays wavelength, θ is the maximum peak angle and K is a constant.

A peak shift can be related to a lattice parameter strain via relation F.1 and can help study crystal deformation.

The `Rigaku, Smartlab` [13] was used for this work, whit Copper as X-ray source. The Smartlab combines in a unique apparatus, the facilities of conventional $\theta - \theta$ diffractometer (for phase analysis and thin films characterization) and those of an Eulerian cradle diffractometer (for pole figure and strain/stress analyses). Accurate measurements of thin film thickness, roughness and density are achievable through X-ray reflectivity (XRR) techniques. Small Angle X-ray Scattering (SAXS) will allow particle size distributions of nanoparticles suspended in solution.

Figure F.2: Rigaku, Smartlab [13].

Appendix G

X-Ray Photoelectron Spectroscopy

X-Ray Photoelectron Spectroscopy (XPS) is a technique that use the photoelectric effect to evaluate the surface composition of a sample [5, 8]. All the elements except for Hydrogen and Helium can be detected. Target electrons can be emitted from any orbital with photoemission occurring for X-ray energies exceeding the binding energy.

X-rays are generated using light elements like Al ($E_{K\alpha} = 1.4866keV$) or Mg ($E_{K\alpha} = 1.2566keV$) because they have very sharp linewidth. Produced X-rays are filtered by a crystal to remove unwanted peaks and travel in high vacuum to the sample.

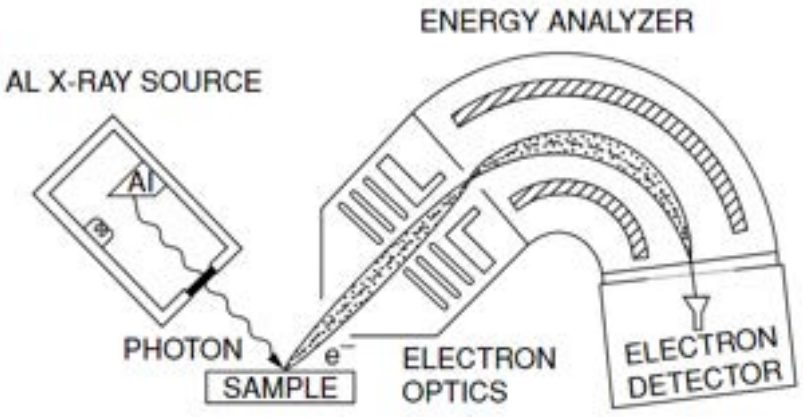

Figure G.1: XPS apparatus scheme [8].

When a photon of high energy energy $h\nu$ interacts with an electron in the sample this escapes and is then detected. This electron must obtain from X-Ray enough energy to exceed binding energy E_b and also the detector work function ϕ_{sp} (some eV). So the binding energy E_b is related to the detection energy E_{sp}:

$$E_b = h\nu - E_{sp} - q\phi_{sp} \tag{G.1}$$

where q is the electron charge.

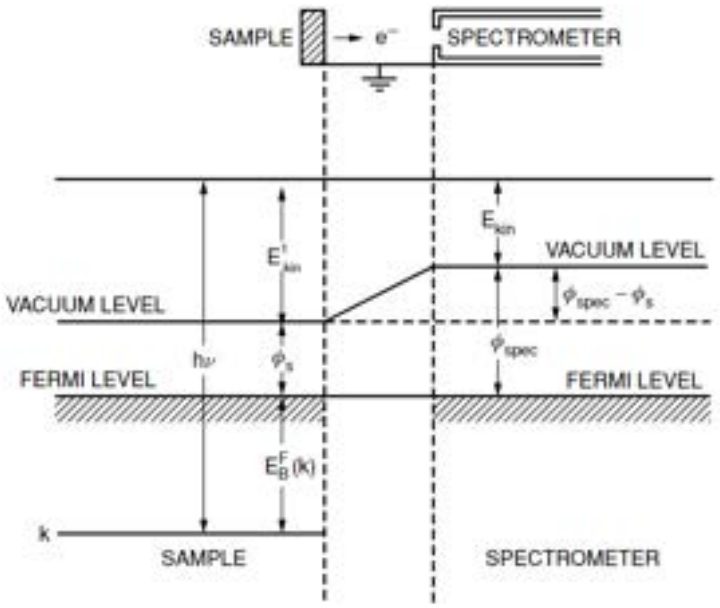

Figure G.2: Energy level scheme of the sample and the detector [8].

Also Auger electrons are produced and detected. Binding energy is characteristic for every element, so an XPS spectrum provides the composition of the sample surface. Deep analysis cannot be made because produced photoelectrons are absorbed before they escape, so this technique can sample about $100nm$ depth. Binding energy of external electrons can be slightly modified by chemical bonding, so a peak shift can indicate the presence of chemical composite like oxides.

Usually detectors are hemispherical electrons energy analyzer. They consist of two concentric conductive hemispheres that serve as electrodes

and bend the trajectories of the electrons when a potential is applied. Electrons enter via a narrow slit and their trajectory depends on their kinetic energy and the applied voltage. So only electrons with selected energy can reach the counter at the end of the path.

The `PHI 5000 VersaProbe II` [14] was used for this work with Aluminum source. The instrument is equipped with a monochromatic, microfocused, scanning X-ray source which provides excellent large area and superior micro-area spectroscopy performance. Spectroscopy, depth profiling and imaging can all be performed over the full range of X-ray beam sizes including the minimum X-ray beam size of less than $10\mu m$. The multi-technique includes a UV lamp for Ultraviolet Photoelectron Spectroscopyă(UPS)ămeasurements.

Figure G.3: PHI 5000 VersaProbe II [14].

Appendix H

Electrochemical measurements on electrodes produced by sputtering deposition and laser dewetting

After the main work described in Chapter 3, a brief comparison was made with some electrodes produced using sputtering and dewetting process using GP as substrate.

H.1 Electrode preparation

The samples were prepared by sputter deposition of a thin film with the sputter `Emitech K550X`. The thin film was then irradiated using the laser described in Appendix A in order to dewett the thin film. This laser process is well known in literature [15] and is easy to perform, cheap and rapid with respect to a flux oven.

H.1.1 Thin film deposition

Sputtering is a thin film deposition technique that uses a ionized gas to extract atoms from a target and deposit them on a substrate. The schematic apparatus in Figure H.1(b) shows the deposition chamber in which a vacuum of $\sim 10^{-}2mbar$ is reached. Inside the chamber, the inert

gas is pumped (typically Argon). Target and substrate are wired with two electrodes that provides high voltage. This high voltage ionizes the gas, forming a plasma in which the ions are accelerated toward the target with an energy up to some keV. With this energy the incident ions collide with the target ions and extract them. With non conductive target an RF alternate current should be applied. The extracted atoms have an energy up to $10eV$ but the amount of sputtered atoms depends on the material sputtering yield defined as $S = \frac{\text{extracted atoms}}{\text{incident ions}}$. The ions travel toward the chamber and reach the substrate were can nucleate and form thin film. The thickness of the film so depends on the sputtering time and the number of atoms. The machine used in this work allows to set the time (up to 4 minute) and the plasma current (up to $50mA$). The film thickness is reported to grow linearly both with current and time [16, 17].

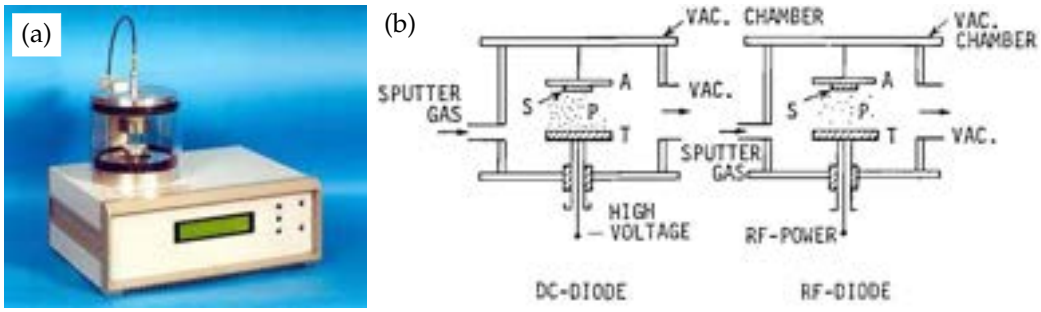

Figure H.1: (a): Sputter coater used in this work [16]. **(b)**: Sputter apparatus scheme (A: anode, T: target, S: substrate, P: plasma) [17].

Three samples were prepared with the parameters of Table H.1: one with Cu, one with Ni and another one sputtering first Ni and then Cu. The mass of the deposited material was evaluated with RBS (as in Chapter 3) and the results a reported in Table H.1. The mass of the mixed sample is given by the sum of the two Nickel and Copper because was made by subsequent deposition. Sputtering parameters were chosen in order to obtain a mass similar to one of the samples produced by PLAL-drop casting. The different used current between the two target within the same time is due because the Nickel has a lower sputtering yield than the Copper.

Target	Current	Time	Dose	Mass
Cu	$10mA$	4 min	$7.29 \cdot 10^{15} at/cm^2$	$0.8\mu g$
Ni	$25mA$	4 min	$7.02 \cdot 10^{15} at/cm^2$	$0.7\mu g$

Table H.1: Sputtering parameters and RBS analysis results.

H.1.2 Laser dewetting

The dewetting process was conducted with the $532nm$ laser beam instead of the $1064nm$ one used for PLAL in Chapter 2 because this shorter wavelength carries double the energy per photon and is near to the plasmonic peak of the Copper seen in Section 2.4.2. The laser beam was deflected with a mirror and pass trough a adjustable beam splitter attenuator, then is reflected with mirrors in an optical path of length $\sim 17m$ and reaches the sample placed in front of the digital power meter. A single shot on the sample produced a laser spot of radius $\sim 0.1cm$. The laser energy fluence was estimated to be $0.5J/cm^2$ using Equation 2.1. The reason behind the long optical path is that guarantee an uniform and homogeneous spacial distribution of the beam intensity.

The repetition rate was set to $1Hz$ and sample was irradiated in $1cm^2$. Figure H.2 shows an electrode with visible laser shot marks that cover the area used for the electrochemical measurements.

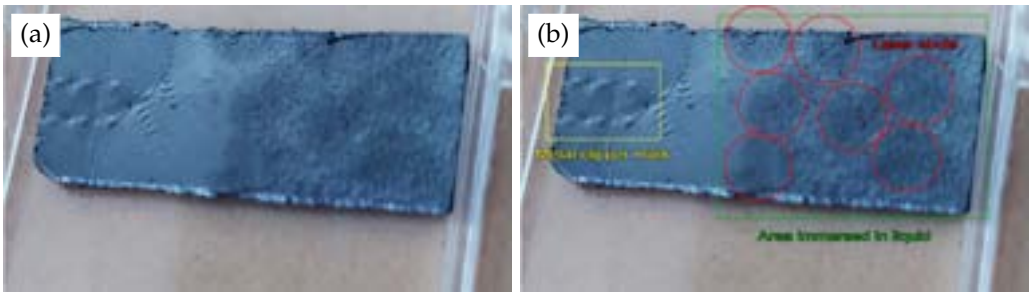

Figure H.2: (a): Example of an used electrode. **(b)**: The same electrode with marked some visible sign of the usage.

H.2 Electrochemical measurements and comparison

The electrochemical measurements were conducted as the ones in Chapter 3: first the OC and MS analysis to evaluate the band bending and then in order CV, LSV and EIS both for HER and OER.

The results obtained from OC and MS are reported in Table H.2 and Figure H.3 compared with the data from Chapter 3. The new Copper electrode reports a band bending value similar to *Cu_met* and so the mixed sample that presents also the double linear zone. The strong difference is in the Nickel that presents very high value of band bending and also a double linear zone. This strong difference may come from some issues in the dewetting process: the laser wavelength ($532nm$) matches the Copper plasmonic peak promoting the process, but is far away the Nickel plasmonic peak $\sim 300nm$.

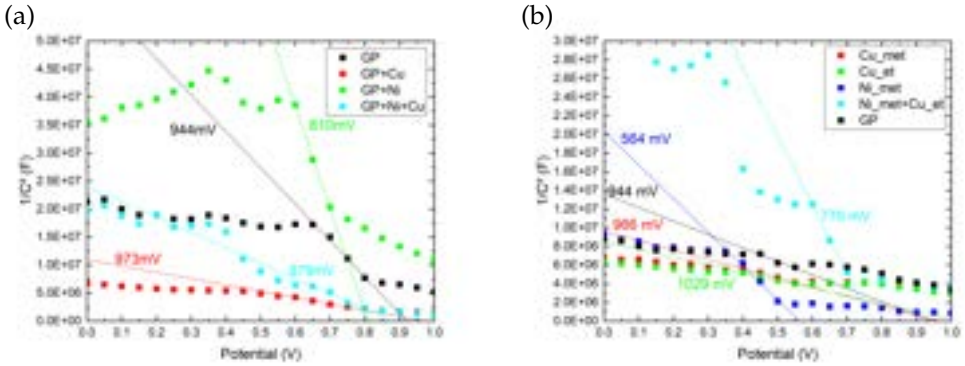

Figure H.3: Mott Schottky plot of GP samples with marked x-intercept. Comparison between electrode produced by **(a)**: sputtering-dewetting, **(b)**: PLAL-drop casting.

This Appendix			Chapter 3		
Sample	V_{OC} $[mV]$	V_{bb} $[mV]$	Sample	V_{OC} $[mV]$	V_{bb} $[mV]$
GP	-213	1132	GP	-213	1132
Cu	-198	1146	Cu_met	-201	1142
			Cu_et	-183	1208
Ni	-259	1368	Ni_met	-192	731
$Ni + Cu$	-182	1036	mix	-213	958

Table H.2: Obtained values for open circuit potential V_{OC} and band bending potential V_{bb} both for samples produced by sputtering-dewetting and PLAL-drop casting.

All the CV measurements were performed with at least 10 cycle and all shows a slightly worsening on all the samples for both HER and OER.

LSV in HER shows that all the samples prepared in this way are worse than the bare GP (Figure H.4 and Table H.3). Probably this behaviour is due to the annealing process that leads to the formation of oxides and/or some surface modification of the substrate. Only the mixed sample presents a similar behaviour in both fabrication techniques.

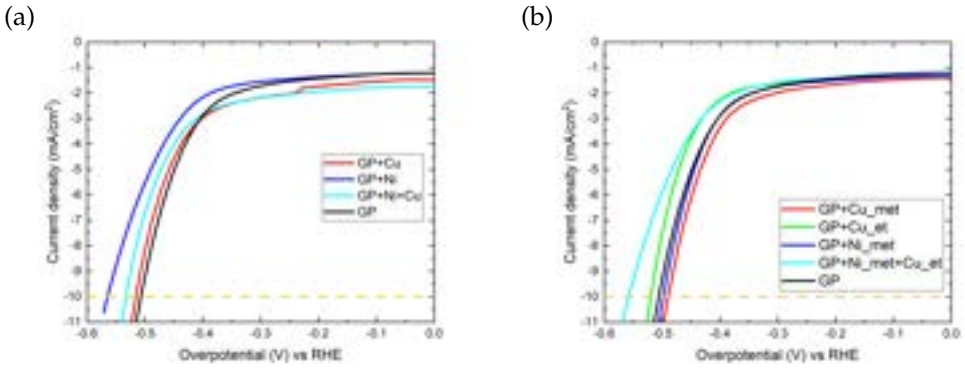

Figure H.4: Linear Sweep Voltammetry of GP samples for HER in $1M\ KOH$ on electrodes produced by **(a)**: sputtering-dewetting and **(b)** PLAL-drop casting. Horizontal dashed line in both plots marks the current density of $10mA/cm^2$. The plots are deliberately in the same axis ranges.

This Appendix			Chapter 3		
Sample	$\eta\ [mV]$	Tafel slope $[mV/dec]$	Sample	$\eta\ [mV]$	Tafel slope $[mV/dec]$
GP	506	192	GP	506	192
Cu	516	180	Cu_met	490	186
			Cu_et	520	162
Ni	565	247	Ni_met	498	177
$Ni + Cu$	532	196	mix	558	239

Table H.3: Summary of LSV measures on GP electrodes for HER in $1M\ KOH$ both for samples produced by sputtering-dewetting and PLAL-drop casting.

LSV in OER shows some good results for the samples prepared in this way (Figure H.5 and Table H.4). Copper and mixed samples curves are very similar and so is their overpotential and Tafel slope, but the mixed sample is slightly better. The Nickel sample, instead, grows very slowly.

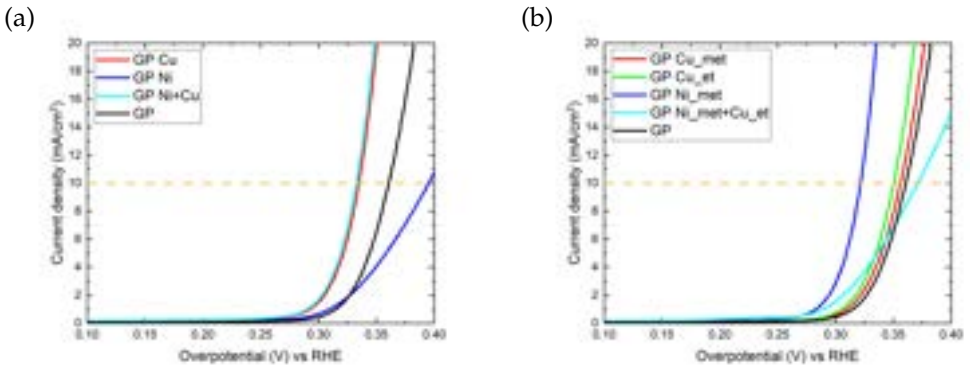

Figure H.5: Linear Sweep Voltammetry of GP samples for OER in $1M\ KOH$ on electrodes produced by **(a)**: sputtering-dewetting and **(b)** PLAL-dropcasting. Horizontal dashed line in both plots marks the current density of $10mA/cm^2$. The plots are deliberately in the same axis ranges.

This Appendix			Chapter 3		
Sample	$\eta\ [mV]$	Tafel slope $[mV/dec]$	Sample	$\eta\ [mV]$	Tafel slope $[mV/dec]$
GP	361	41	GP	361	41
Cu	335	52	Cu_met	356	42
			Cu_et	350	42
Ni	395	166	Ni_met	321	39
$Ni + Cu$	333	52	mix	371	59

Table H.4: Summary of LSV measures on GP electrodes for OER both for samples produced by sputtering-dewetting and PLAL-dropcasting.

EIS (Figure H.6 and Tables H.5 and H.6) shows the explicit double semicircle behaviour only for the Nickel sample indicating an high charge transfer resistance. This is compatible with the previous measures of high overpotential and Tafel slope. The mixed sample presents the lowest R_{ct} and the Copper sample presents the lowest R_p (smallest semicircles) indicating the low Tafel slopes. These considerations are valid for both HER and OER.

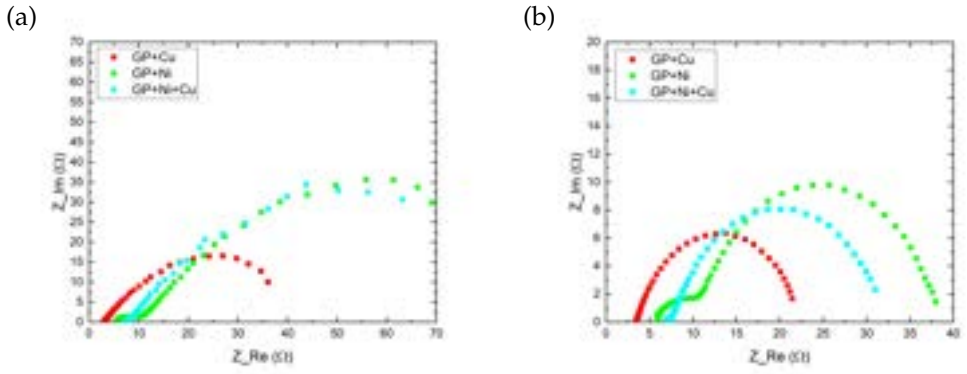

Figure H.6: Electrochemical Impedance Spectroscopy of GP-based electrode in $1M\ KOH$ for **(a)**: HER and **(b)**: OER on electrodes produced by sputtering-dewetting.

Sample	Potential vs SCE $[V]$	R_u $[\Omega]$	R_{ct} $[\Omega]$	R_p $[\Omega]$	C_{dl} $[F]$	α_{dl}	Q_p $[F]$	α_p
Cu	-1.48	3.0	2	60	0.01	0.7	0.007	0.6
Ni	-1.46	5.6	7	132	0.001	0.5	0.01	0.7
$Ni + Cu$	-1.47	7.2	1	155	0.0001	0.6	0.01	0.7

Table H.5: Summary of EIS measures on GP electrodes produced with sputtering-dewetting for HER fitted with [18].

Sample	Potential vs SCE $[V]$	R_u $[\Omega]$	R_{ct} $[\Omega]$	R_p $[\Omega]$	C_{dl} $[F]$	α_{dl}	Q_p $[F]$	α_p
Cu	0.46	3.4	1	18	0.005	0.8	0.005	0.7
Ni	0.47	5.9	5	27	0.0003	0.7	0.004	0.8
$Ni + Cu$	0.46	7.2	1	24	0.002	0.8	0.006	0.7

Table H.6: Summary of EIS measures on GP electrodes produced with sputtering-dewetting for OER fitted with [18].

H.3 Results and considerations

The model proposed in Chapter 3 can be applied also to this samples: the band bending are represented in Figure H.7. In OER the downward voltage steps (in the direction from the substrate to the liquid) represents a forward bias, so the lowest overpotential correspond to the $Ni + Cu$ sample as reported by the data. In HER the lowest overpotential correspond to the Cu sample in which the junction between the substrate and the NPs is in forward bias and the overall potential well is less deep.

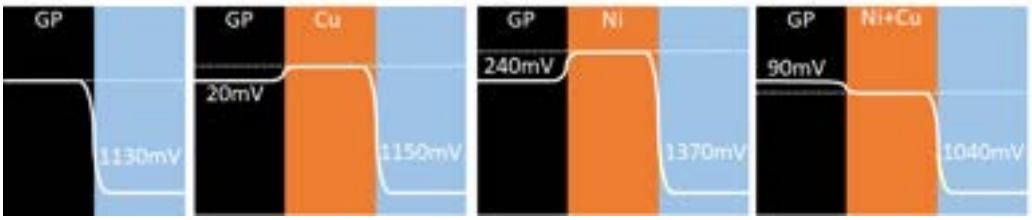

Figure H.7: Band scheme of the GP electrodes produced by sputtering-dewetting with marked approximated voltage steps (not in scale).

All the results obtained in this Appendix involving water splitting are summarized in Table H.7 compared with the ones found in Chapter 3 in Table 3.14. The catalyst loading in all the sample is about $\sim 1\mu g$. The performance in HER of the samples produced by sputtering-dewetting are worse than the one produced by PLAL-drop casting maybe due to some oxidation process occurred during the laser dewetting. The overpotential in OER are comparable in the samples produced by both techniques.

Figure H.8 shows the same group of data of Figure 3.26 with new data distributed between the others obtained in Chapter 3.

Substrate	NPs	Catalyst loading $[\mu g/cm^2]$	HER $\eta[mV]$	Tafel slope $[mV/dec]$	OER $\eta[mV]$	Tafel slope $[mV/dec]$
GP	*Cu_met*	0.8	490	186	356	42
GP	*Cu_et*	1.1	520	162	350	42
GP	*Ni_met*	0.7	498	177	321	39
GP	mix	0.9	558	239	371	59
NF	*Cu_met*	0.8	211	90	338	51
NF	*Cu_et*	1.1	224	95	331	51
NF	*Ni_met*	0.7	230	90	327	44
NF	mix	0.9	238	90	345	48
GP	*Cu*	0.8	516	180	335	52
GP	*Ni*	0.7	565	247	395	166
GP	$Ni + Cu$	1.5	532	196	333	52

Table H.7: Summary of the obtained results including **Catalyst loading**, **Overpotential** vs RHE and **Tafel slope** for HER and OER in $1M$ *KOH* aqueous ambient including data from Table 3.14.

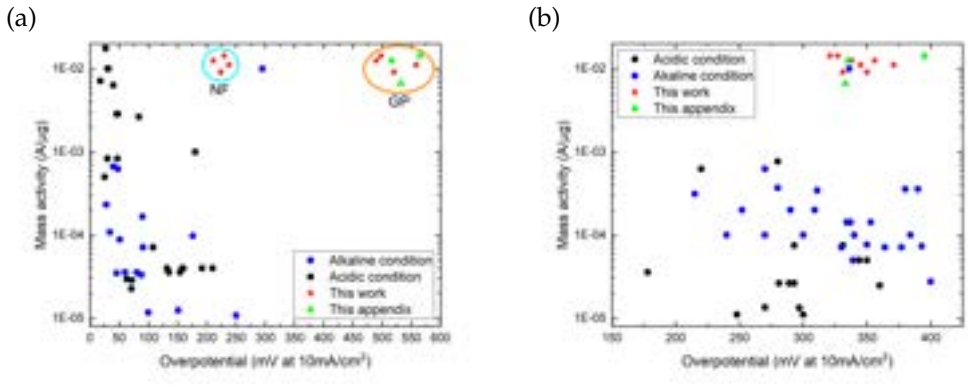

Figure H.8: (a): Literature data for HER from Table 1.2 [19] with added data from this work. Two groups of data are presents indicating the NF-based and the GP-based electrodes. **(b)**: Literature data for OER from Table 1.3 [19] with added data from this work. Obtained data are presented in Table H.7, red stars are data from Chapter 3, green triangles are data from this Appendix. Mass activity is evaluated from Catalyst Loading with Equation 1.22.

Appendix Bibliography

[1] *Quanta-Ray Lab-Series - Users Manual*, 2003.

[2] Bahaa E A Saleh and Malvin Carl Teich. *Fundamentals of Photonics*. Wiley Series in Pure and Applied Optics. Wiley-Blackwell, Chichester, England, 2 edition, February 2007.

[3] *Spectrophotometry: Volume 46*. Experimental Methods in the Physical Sciences. Academic Press, San Diego, CA, July 2014.

[4] *Varian Cary 500 Spectrophotometers - User's manual*.

[5] Dieter K Schroder. *Semiconductor material and device characterization*. Wiley - IEEE. Wiley-Blackwell, Chichester, England, 3 edition, January 2006.

[6] Joseph I Goldstein, Dale E Newbury, Joseph R Michael, Nicholas W M Ritchie, John Henry J Scott, and David C Joy. Ion beam microscopy. In *Scanning Electron Microscopy and X-Ray Microanalysis*. Springer New York.

[7] Joseph Goldstein, Dale E Newbury, David C Joy, Charles E Lyman, Patrick Echlin, Eric Lifshin, Linda C Sawyer, and J R Michael. *Scanning electron microscopy and X-ray microanalysis*. Springer, New York, NY, 3 edition, May 2013.

[8] Terry L Alford, L C Feldman, and James W Mayer. *Fundamentals of Nanoscale Film Analysis*. Springer, New York, NY, 2007 edition, February 2007.

[9] Dott. s. boninelli notes.

[10] Cnr-imm - characterization at catania headquarters. `https://www.imm.cnr.it/articles/characterization-catania-headquarters`.

[11] Rump - genplot. `http://www.genplot.com/`.

[12] Yoshio Waseda, Eiichiro Matsubara, and Kozo Shinoda. *X-ray diffraction crystallography*. Springer, Berlin, Germany, 2011 edition, March 2011.

[13] Brit unict - x-ray diffractometer. http://www.brit.unict.it/it/section/services/x-ray-diffractometer.

[14] Brit unict - x-ray photoelectron spectroscopy (xps). http://www.brit.unict.it/it/section/services/x-ray-photoelectron-spectroscopy-xps.

[15] Francesco Ruffino and Maria Grazia Grimaldi. Nanostructuration of thin metal films by pulsed laser irradiations: A review. *Nanomaterials*, 9(8):1133, August 2019. doi:10.3390/nano9081133.

[16] *K550X Sputter Coater - Instruction Manual*.

[17] Kiyotaka Wasa and Shigeru Haber. *Handbook of sputter deposition technology*. William Andrew Publishing, Norwich, CT, December 1992.

[18] Eis spectrum analyzer. http://www.abc.chemistry.bsu.by/vi/analyser/.

[19] Jakob Kibsgaard and Ib Chorkendorff. Considerations for the scaling-up of water splitting catalysts. *Nature Energy*, 4(6):430–433, May 2019. doi:10.1038/s41560-019-0407-1.